Shear-banding in Entangled Polymer Solutions under Large Amplitude Oscillatory Shear: A Confocal Rheometry Study

A THESIS

SUBMITTED TO THE FACULTY OF THE GRADUATE SCHOOL

OF THE UNIVERSITY OF MINNESOTA

BY

Seunghwan Shin

IN PARTIAL FULFILLMENT OF THE REQUIREMENTS

FOR THE DEGREE OF

DOCTOR OF PHILOSOPHY

Kevin D. Dorfman, Advisor

Xiang Cheng, Advisor

April, 2020

Acknowledgements

First and foremost, I would like to express my utmost appreciation my advisors, Professor Xiang Cheng and Professor Kevin D. Dorfman for their guidance, patience, and encouragement throughout my studies. They were always enthusiastic and caring mentors during the entire years, and none of this work would have been possible if it were not for their support. Their deep understanding of polymers, fluids, and physics and passion for research gave me an inspiration and have driven me to keep dreaming a better researcher.

I would like to extend my sincere gratitude to my committee members, Professor Cari Dutcher and Professor Sungyon Lee for serving on my doctoral final oral examination committee and for reviewing my dissertation. They all provided me with invaluable comments for improving my research and dissertation.

I also hope to have opportunities to thank the members in Cheng and Dorfman research groups: Truong Pham, Bo Zhang, Lian Bai, Leonardo Gordillo, Yu Abe, Devranjan Samanta, Xiaolei Ma, Yi Peng, Dipanjan Ghosh, Shashank Kamdar, Yangming Kou, Zhengyang Liu, Gregorius Pradipta, Yiming Qiao, Ting-Pi Sun (Cheng group), Aashish Jain, Zhicheng Long, Michael McGovern, Julian Sheats, Shi Yu, Vaidya Sethuraman, Pranav Agrawal, Akash Arora, Hui-Min Chuang, Sarit Dutta, Damini Gupta, Scott King, Xiaolan Li, Abhiram Muralidhar, Joel Thomas, Doug Tree, Scott White,

Demetra Adrahtas, Paridhi Agrawal, Aditya Bhandari, Logan Case, Anshul Chawla, Pengyu Chen, Guo Kang Cheong, Zixue Ma, Sarah Seeger, and Mathew Thomas (Dorfman group). Adapting to new environments as an international student is not always easy, but these people made my life here enjoyable at all times, both in research and a daily life. I can never forget precious memories I've had here with them during my gradate years.

I want to acknowledge funding by National Science Foundation on shear-banding of polymer solutions (NSF-1700771). Also, I would like to acknowledge financial support from the Kwanjeong Educational Foundation during earlier years of my graduate study.

Lastly, I am forever grateful to my family, Chungsang Shin, Soongeum Lee, Soojeong Shin, and to my fiance, Jinah Jeun, to whom my dissertation is dedicated, for their endless love and support.

To my family

Abstract

We use a large aspect-ratio, planar-Couette shear cell to explore the flow properties of entangled polymer solutions, with a special focus on a long-standing problem of shear-banding in polymer solutions/melts. We first analyze the velocity profiles of entangled DNA solutions under large amplitude oscillatory shear (LAOS) inside the shear cell. We vary a gap between the shearing plates and Weissenberg number (Wi) to construct phase diagrams quantifying the degree of wall-slip and shear-banding at different conditions. We observe transitions from normal linear shear profiles to wall-slip dominant and finally to shear-banding profiles with increasing Wi. We further explore the dynamics of micron-sized tracer particles embedded in the solutions to study the microscopic origin of the shear-banding. Tracer particles in the shear frame exhibit transient super-diffusivity and strong dynamic heterogeneity localized in the high-shear-rate band. The probability distribution functions of particle displacements follow a power-law scaling at large displacements, indicating a Lévy-walk-type motion, reminiscent of tracer dynamics in entangled wormlike micelle solutions and sheared colloidal glasses. We further characterize the length and time scales of the abnormal dynamics of tracer particles. Based on them, we hypothesize that the unusual particle dynamics arise from localized shear-induced chain disentanglement.

Next, we experimentally investigate a penetration of edge-induced disturbances and

its influence on shear-banding flows. Edge instabilities have been pointed out as one of the possible experimental artifacts leading to apparently heterogeneous shear profiles. Simulations suggested even a mild edge disturbance can penetrate deeply along a vorticity direction to cause apparent gradient-banding of a velocity profile, potentially misleading experimentalists. We measure velocity profiles at different locations to reveal penetrating behavior of edge disturbances and test authenticity of the observed shear-banding flows. Under a weak oscillatory shear ($\mathrm{Wi} < 1$) where DNA solutions display a linear shear profile with wall slip, the penetration depth of the edge disturbance was on the order of the gap thickness , similar to a behavior in Newtonian fluids. Under a strong shear ($\mathrm{Wi} > 1$) where shear-banding flows are developed, the penetration depth was estimated as 20 H along the flow direction while it was still on the order of the gap thickness along the vorticity direction. Furthermore, we find that the shear-banding profiles persist deep inside the sheared fluid, where the influence of edge disturbances diminishes. Our findings suggest a long penetration of the edge disturbance and also demonstrates the authentic nature of the observed shear-banding polymers.

Shear-induced microscopic conformational change of individual polymer chains that trigger shear banding still remains an open question. To attain information about chain-end distributions and its dynamics, we synthesize dumbbells consisting of two spherical colloidal tracer particles connected by λ-DNA linkers and track their 2D-projected configurations and motions in the two shear-bands. We observe preferable alignment along the flow direction, enhanced translation/rotation in the high-shear-rate band. Coupling between translational/rotational dynamics and stronger correlation between chain extension and translation are also found in the high-shear-rate band. We hypothesize a formation of the localized low viscosity zones which allow the enhanced dynamics and chain extension in the high-shear-rate band.

Contents

List of Figures

Chapter 1

Introduction

1.1 Motivation

A polymer is a macromolecule composed of many repeating units. Owing to their tunable versatile properties, polymer products are ubiquitous and inseparable from our daily lives. Since numerous manufacturing and engineering processes of such polymer products involve fast flows of concentrated polymer solutions and melts, where polymeric fluids experience large and rapid non-linear deformations, a concrete knowledge about properties of polymer fluids in the non-linear flow regime will be of great practical importance. However, whereas the polymer dynamics is well understood in the linear viscoelastic regime and its characterization is remarkably successful at low or intermediate flow rate regimes, deviation from the theoretical predictions becomes more evident as higher shear rate flow is imposed [1].

Shear-banding, the co-existence of separated flow regimes with different shear rates, has been one long-standing non-linear flow problem especially in entangled polymer solutions and melts. Even though it was theoretically predicted many decades ago [2], its existence (or lack thereof) was under heated controversy until very recently and its

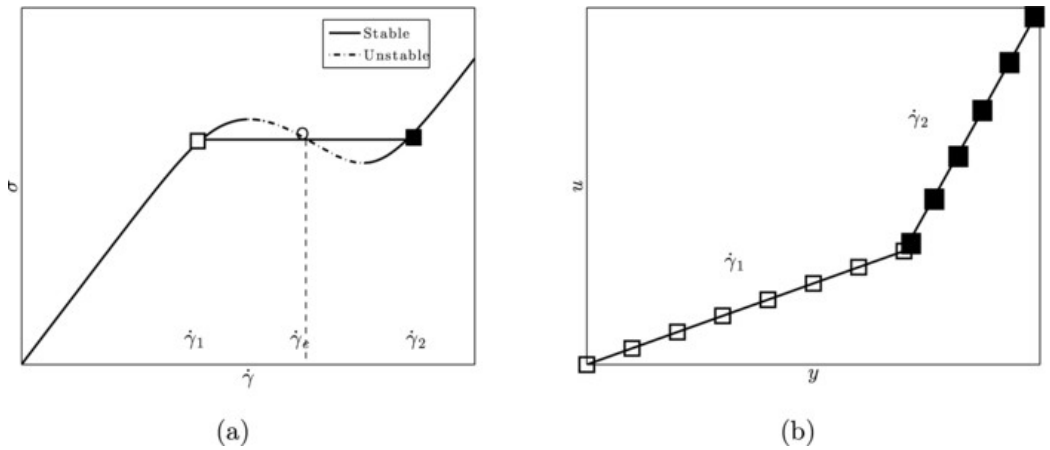

Figure 1.1: (a) A schematic of non-monotonic flow relation between shear stress and shear rate. The region with a negative slope is mechanically unstable. If $\dot{\gamma}$ in the range of the negative slope is applied, the sheared fluid automatically separates into multiple bands. (b) A schematic of a resulting shear-banding velocity profile. While the shear stress is constant, its local shear rates $(\dot{\gamma_1}, \dot{\gamma_2})$ may differ from the applied shear rate (γ_c). Reproduced from Ref. [3].

full understanding is still far from complete. If shear-banding indeed occurs, the *a priori* assumption of homogeneous flow on which conventional rheological characterization is based will be disobeyed and all the rheological measurements that have been made in this regime will be called into question. Therefore, a comprehensive picture of the shear-banding in entangled polymer systems is urgently needed.

Since shear-banding is a long-standing problem, it will be helpful to understand it from a historic perspective. A dynamic theory of entangled polymer dynamics under flow was formalized based upon a relaxation mechanism of entangled polymer chains at equilibrium [4], so it will be a good starting point for a historic review. In the depiction of the dynamics of entangled polymeric fluids, the tube concept has been proven successful and it is widely accepted as a standard theoretical framework [5]. The tube concept was first suggested by Edwards [6] more than 50 years ago. He claimed that

collective topological constraints imposed on a single chain by its surrounding chains can be coarse-grained as a confining tube-like potential along its contour. Adopting this idea, de Gennes proposed the concept of reptation in his discussion about a possible dynamics of a macromolecular chain in a cross-linked polymer gel, and he successfully reasoned out molecular weight dependence of relevant time scales and diffusivity [7]. The concept of diffusion by reptation was later incorporated by Doi and Edwards into their theory of polymer dynamics [8–10]. The basic premise of the Doi-Edwards theory is that, in highly entangled polymer solutions and melts, the diffusion of a chain perpendicular to its backbone is more strictly hindered than the diffusion along its contour due to temporary topological constraints, so the chain will undergo a snake-like diffusion along the contorted tube formed by the surrounding chains. A relevant characteristic relaxation time scale, the reptation time or disengagement time (τ_d), is defined as the time required for a confined chain to escape from its original tube constraint. In the original tube theory, the retraction of a stretched chain was assumed instantaneous, but modified later by Marrucci and Grizzuti by introducing the Rouse-stretch time (τ_R) [11].

In the original tube approach, non-linear deformation at high shear rates ($\dot{\gamma} > \tau_d^{-1}$) aligns the tube segments along the flow direction and the sheared fluid exhibits a very strong shear-thinning behavior due to over-orientation, which eventually leads to a non-monotonic relationship between shear-stress and shear-rate (Fig. 1.1) [3]. Such a non-monotonic constitutive curve is mechanically unstable, so the fluid spontaneously separates into macroscopic regimes with fast and slow shear rates [12]. This phenomenon is called "shear-banding." Marrucci [2] highlighted that the Doi-Edwards theory predicts the non-monotonic constitutive curve which leads to the shear-banding and formalized the idea that a spurt effect observed in polymer melts [13], the sudden increase of the flow rate above a critical pressure drop, could be its consequence. Motivated by the theoretical formalization, experimentalists attempted to observe the shear-banding

phenomenon in entangled polymer solutions and melts. However, the shear-banding was not reported in those systems for a long time [14].

As experimental results did not support the prediction by the original Doi-Edwards theory, both experimental and theoretical efforts were made to reconcile them. From experimental side, wormlike-micelle (WLM) solutions were studied as a wide range of shear stress plateau, hinting to the existence of shear-banding, was confirmed in this system [16, 17]. WLM chains can be entangled in an analogous way to entangled linear polymer chains while they can also combine and break. In a fast shear flow, they indeed displayed shear-banding velocity profiles and a strong flow-structure coupling. For example, in experiments coupling a flow cell and small angle neutron scattering (SANS) [15], a flow induces a low viscosity phase (high-shear-rate band) where chains are more aligned along the flow direction (Fig. 1.2).

Theoreticians worked on updating and refining the existing tube theory by introducing additional relaxation mechanisms to "heal" the mechanical instabilities of the non-monotonic constitutive curve [18]. The most important addition to the model in regard to the shear-banding problem is convective constraint release (CCR) [19]. The CCR allows some stress felt by a test chain can be relaxed when entanglement points are partially convected away as chains slide past each other. In its simplest form [20],

$$\frac{1}{\tau_i} = \frac{1}{\tau_{i,eq}} + \beta \left(\mathbf{k} : \bar{\mathbf{S}} - \frac{1}{\lambda} \frac{d\lambda}{dt} \right), \tag{1.1}$$

where τ_i is the CCR-affected relaxation time, $\tau_{i,eq}$ is the equilibrium relaxation time without CCR, β is the CCR parameter ($0 < \beta < 1$), $\mathbf{k}$ is the velocity gradient tensor or strain-rate tensor, $\bar{\mathbf{S}}$ is the average tube orientation tensor, and λ is the ratio between the stretched/unstretched tube length. As inferred from Eq.(1.1), the CCR accelerates the relaxation rate. The relaxing contribution from CCR becomes more and more significant

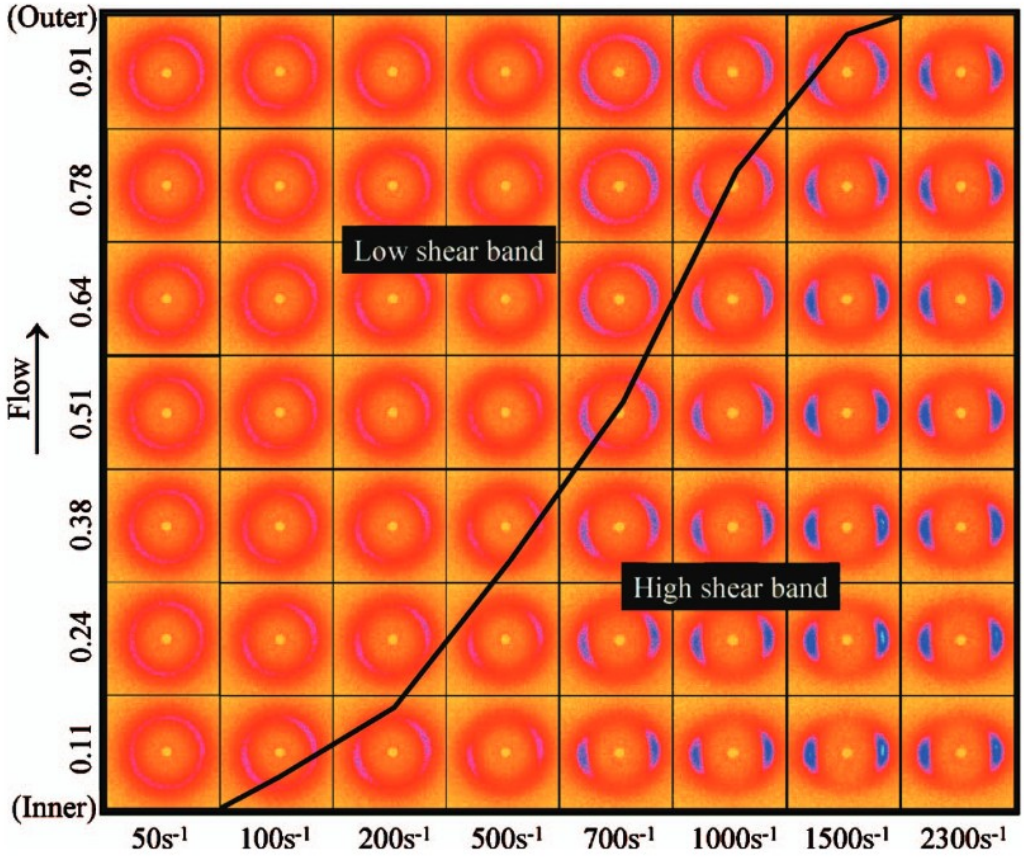

Figure 1.2: Two dimensional 1-2 flow-SANS patterns of 490 mM cetyltrimethylammonium bromide (CTAB) in D_2O solution at different applied shear rates and normalized gap positions. A black inset line denotes the interface between the shear bands, determined by Particle Image Velocimetry. Unique peaks (blue) in SANS patterns of the high band indicate alignment along the flow direction. Reproduced from Ref. [15].

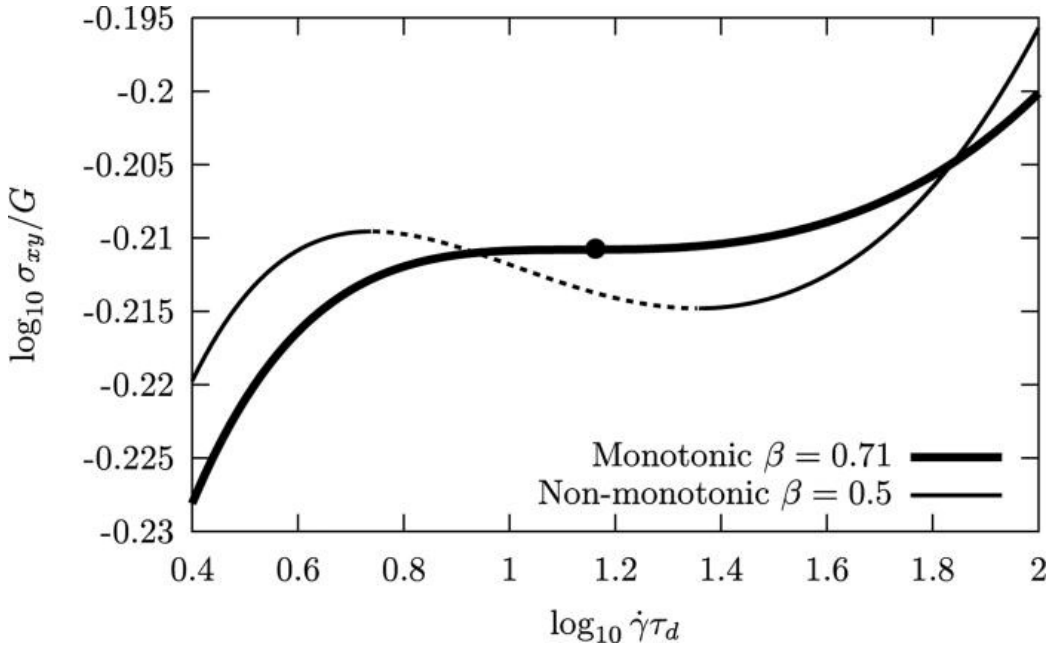

Figure 1.3: Constitutive curves arising from Rolie-Poly model simulations with different CCR parameters, β. The shear stress and the shear rate are normalized by the plateau modulus (G) and reptation relaxation rate (τ_d), respectively. Increasing β from 0.5 to 0.71 eliminated the non-monotonicity of the constitutive equation. Reproduced from Ref. [21].

as the shear rate is higher and the chain is more stretched, thereby reducing the shear stress peak and eliminating the troublesome non-monotonic instability of the flow curve as described in Fig. 1.3 [21]. The most refined version of such a theoretical effort is the so-called GLaMM model (**G**raham, **L**ikhtman **a**nd **M**ilner-**M**cLeish) [22] or its simplified differential version, the Rolie–Poly model (**RO**use **LI**near **E**ntangled **POLY**mers) [23]. Its predictions showed quantitative agreement with experiments covering a wide range of shear rates.

While theorists developed a refined model and became convinced that shear-banding

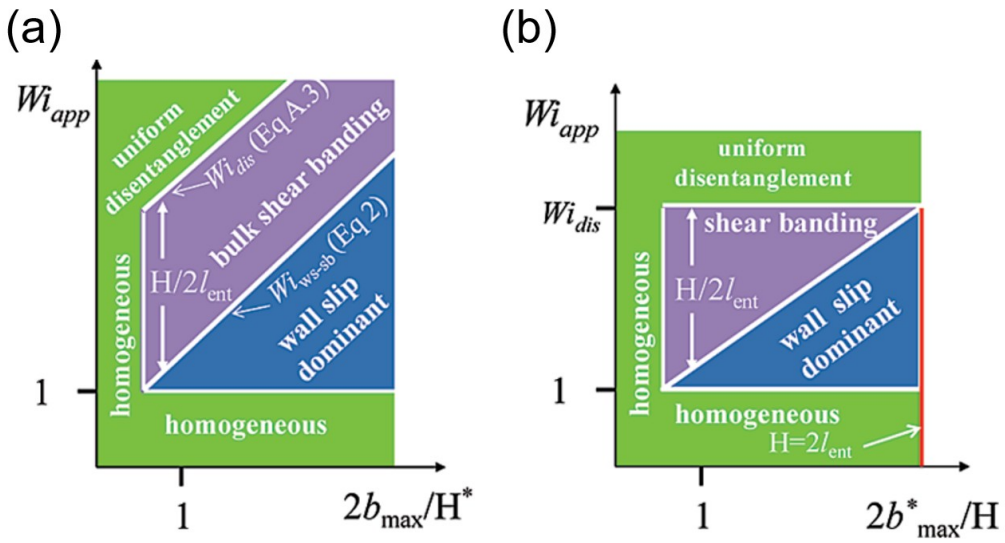

Figure 1.4: Phase diagrams in the parameter space of Wi and $2b_{max}/H$ in a log-log scale. In the three diagrams, the variable denoted with * is fixed in an experimental setup. (a) When a gap thickness (H^*) is fixed, a vertical line is experimentally accessible by varying $\mathrm{Wi_{app}}$. (b) For a given sample with a constant maximum slip length (b^*_{max}), the gap thickness (H) and the applied shear rate ($\mathrm{Wi_{app}}$) can be adjusted to explore the phase diagram. Reproduced from Ref. [24].

would not occur in the entangled polymer solutions and melts due to the healed monotonic constitutive curve, experimental observations of the phenomenon in polymer system were finally reported. Britton [25] and Callaghan [26] found heterogeneous velocity gradient developing inside a sheared polyacrylamide (PAAm) solution by combining nuclear magnetic resonance (NMR) velocimetry with a cone-plate rheometer. Later, owing to advancement of the *in-situ* particle tracking velocimetry (PTV) technique, Wang and coworkers conducted extensive experimental observations of shear-banding in polybutadiene (PBD) and deoxyribonucleic acid (DNA) solutions under different shear protocols, including time independent steady shear [27–31], time-dependent start-up shear [28–32], and time-dependent large amplitude oscillatory shear (LAOS) [32–34]. Phase diagrams (Fig. 1.4) were also presented to depict where linear, wall-slips, and shear-banding velocity profiles are expected as a function of the applied Weissenberg number ($\mathrm{Wi}_{\mathrm{app}}$) and a normalized maximum slip length [24]. In their phase diagram, as $\mathrm{Wi}_{\mathrm{app}}$ is increased for a sufficiently entangled polymer solution, wall-slip always precedes shear-banding. Since polymer chains can be partially or entirely adsorbed to shearing plates, the remaining free portion of the chains near the plates have a shorter effective length, and thereby a lower effective entanglement density, than in the bulk region. It leads to the formation of lower viscosity zones of a molecular size thickness near the shearing boundaries under flow, and the wall-slip dominates here. The slip reduces the effective shear strain and shear rate experienced by the bulk solution such that it remains in the linear flow regime until the viscosity of the thin layer almost reaches its lower bound, the solvent viscosity. When even higher shear rate ($\mathrm{Wi}_{\mathrm{app}} > \mathrm{Wi}_{\mathrm{ws-sb}}$) is applied, the bulk solution is finally forced to experience non-linear shear flow ($\mathrm{Wi} > 1$) even after reduction due to the wall-slip, and transition from wall-slip to shear-banding happens. A critical Weissenberg number ($\mathrm{Wi}_{\mathrm{ws-sb}}$) in Fig. 1.4 corresponds to $\mathrm{Wi}_{\mathrm{app}}$ where the

transition from wall-slip to shear-banding occurs, and it is estimated as:

$$\mathrm{Wi_{ws-sb}} = 1 + 2\mathrm{b_{max}}/\mathrm{H}, \tag{1.2}$$

where the maximum slip length, b_{max}, can be determined from a rheology test.

However, their experimental findings [27,33,35] were debated because of the rheometer apparatus exploited to prevent the exposed fluid/air interface from fracturing. For instance, they wrapped a plastic film around a fluid meniscus and used a cone-partitioned-plate (CPP) rheometer. They were criticized by other researchers [36] since the protective film and the trench in the CPP rheometer could have affected the measured velocity profiles. A collaborative group of rheologists from four different institutes [36] reported that they could not find a convincing evidence of shear-banding in the regime where Wang and coworkers had claimed to discover it based on their phase diagrams (Fig. 1.5). They argued that the shear-banding in Wang and coworkers' experiments may be due to mis-alignment of shearing plates, edge fractures, or optical aberrations. Wang and coworkers pointed out that the molecular weight of PBD the critics used was actually lower than the value they reported and the debate was not quickly resolved [37–39]. To make it even more complicated, some experimental works [40, 41] suggested the shear-banding in polymer systems may not be a true steady-state as the steady states they reached under the same final shearing condition exhibited dependence on the previous ramping history. Aside from the controversies, the shear-banding phenomenon was experimentally reported also by other researchers in entanled polymer systems such as PAAm solutions [42, 43], actin filament solutions [44], single-stranded and double-stranded DNA solutions [45], and xanthan solutions [46].

Updates have been made from the modeling side in order to capture the newly discovered experimental shear-banding polymer flows. Phenomenological models are often

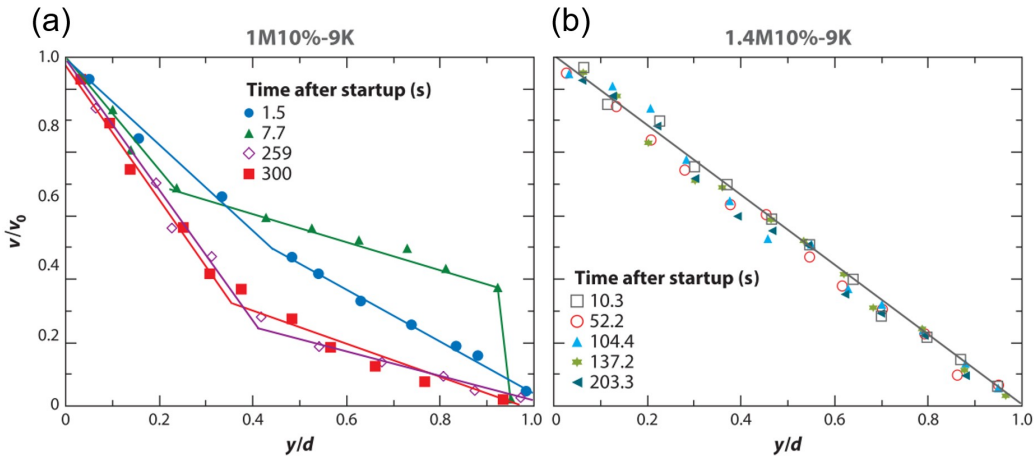

Figure 1.5: Velocity profiles at different times under start-up shear in the rotating parallel plate rheometer. Reproduced from Ref. [47] (a) Ref. [33] reported transient and steady shear-banding profiles with a PBD solution, with an average number of entanglement per chain $(Z) = 42$. (b) Velocity profiles obtained from a similar protocol. The sample has a slightly higher concentration than (a) and $Z = 55$. Ref. [36] did not observe an evidence of shear-banding in the experiment even though it falls in the shear-banding regime of the phase diagram (Fig. 1.4.)

used as microscopic models are not easily tractable in the non-linear flow regimes where shear-banding flows are developed. The phenomenological models usually decompose a total stress ($\mathbf{T}$) into contributions from a solvent part and a polymer part:

$$\mathbf{T} = -p\mathbf{I} + 2\eta\mathbf{D} + \mathbf{\Sigma}, \tag{1.3}$$

where $\mathbf{I}$ is the identity tensor, $\mathbf{D}$ is the symmetric velocity gradient tensor defined as $\mathbf{D} = \frac{1}{2}[\nabla\mathbf{v} + (\nabla\mathbf{v})^T]$, p is the pressure, η is the solvent viscosity, $\mathbf{v}$ is the velocity field, and $\mathbf{\Sigma}$ is an extra stress. The first two terms denote a Newtonian stress arising from a solvent and the last term corresponds to a polymeric contribution. Additionally, incompressible flow and creeping (inertia-less) flow are commonly assumed.

$$\nabla \cdot \mathbf{v} = 0 \tag{1.4}$$

$$\nabla \cdot \mathbf{T} = 0 \tag{1.5}$$

In experiments, the stress plateau reached at steady state is usually independent of initial conditions and flow history [47]. This unique stress selection rule requires inclusion of the stress diffusion term in the governing equation of the polymeric stress [48]:

$$\frac{\partial \mathbf{\Sigma}}{\partial t} = f(\dot{\gamma}, \mathbf{\Sigma}) + \mathcal{D}\frac{\partial^2 \mathbf{\Sigma}}{\partial y^2} \tag{1.6}$$

Here, the second term stands for the stress diffusion along the gradient direction and it describes the response to the inhomogeneous viscoelastic stress. f is a non-linear function, the exact form of which depends on the constitutive model of choice. $\mathcal{D}$ allows for estimation of typical width of interface between the bands, $l = \sqrt{\mathcal{D}\tau}$, where τ is the relaxation time of the fluid.

In relatively simpler phenomenological models such as the diffusive Giesekus model [49] or the diffusive Johnson-Segalman model [50], microscopic details are coarse-grained into quantities defined at macroscopic scales. As a result, those models cannot fully capture microscopic dynamics of polymer chains even though they can reproduce many aspects of shear-banding flows in polymeric solutions. A compromise between coarse-grained phenomenological models and microscopic details is made by using the diffusive Rolie-Poly model, which is a simplified version of the refined Doi-Edwards theory introduced above [23]. Here, the viscoelastic contribution of the stress ($\mathbf{\Sigma}$) is replaced by a product of the elastic modulus (G) and the polymeric strain ($\mathbf{W}$), $\mathbf{\Sigma} = G\mathbf{W}$. Description of $\mathbf{W}$ contains microscopic details about the polymer chain dynamics and it is defined here along with the diffusive term as follows [21]:

$$\begin{aligned}(\partial_t + \mathbf{v}\cdot\nabla)\mathbf{W} - (\nabla\mathbf{v})^T\cdot\mathbf{W} - \mathbf{W}\cdot(\nabla\mathbf{v}) + \frac{1}{\tau_d}\mathbf{W} \\ = 2\mathbf{D} - \frac{2}{\tau_R}(1-A)[\mathbf{I} + \mathbf{W}(1+\beta A^{-2\delta})] + \mathcal{D}\nabla^2\mathbf{W},\end{aligned} \tag{1.7}$$

where $A = (1 + \mathrm{tr}\mathbf{W}/3)^{-1/2}$. Again, τ_d is the characteristic time required for a polymer chain to escape from the initial confining tube by means of 1D curvelinear diffusion along the tube contour (reptation time), τ_R is the Rouse time governing chain stretch, and β is the CCR parameter that controls the efficacy of strain release by convective flows. $\delta = -1/2$ was chosen in the original Rolie-Poly model by comparison with transient and steady state measurements under the assumption of homogeneous flows [23]. The average number of entanglement per chain (Z) is determined by the ratio between the two relaxation times:

$$Z = \frac{1}{3}\frac{\tau_d}{\tau_R} \tag{1.8}$$

The diffusive Rolie-Poly model has been widely used to study the emergence of shear-banding flow in a variety of flow conditions. Adams and Olmsted [21, 51] tuned

the CCR parameter to control the monotonicity of the constitutive curve. Even in absence of constitutive instability, they found that transient shear-banding could appear in start-up, LAOS, and step strain protocols if a geometry with large stress gradient is exploited. This finding was extended by Moorcroft and Fielding [52, 53] who conducted systematic linear stability analysis studies to reveal the criteria for occurrence of shear-banding flows. The linear stability analysis determines whether an initially homogeneous flow becomes unstable in response to the growth of locally introduced perturbations of heterogeneous flows, which is considered as a precursor to the shear-banding. In the steady shear flow, they found the following criterion for linear instability:

$$\frac{\partial T_{xy}}{\partial \dot{\gamma}} < 0 \tag{1.9}$$

This criterion is same as the constitutive instability arising from the region of negative slope in the flow curve. Therefore, it indeed predicts that the non-monotonic constitutive curve is required to develop a steady shear-banding profile. More importantly, transient shear-banding flows can be realized even if the underlying constitutive curve is monotonic when the following condition is satisfied:

$$-\,\mathrm{tr}M\frac{\partial T_{xy}}{\partial \gamma} + \dot{\gamma}\frac{\partial^2 T_{xy}}{\partial \gamma^2} < 0, \tag{1.10}$$

where M characterizes conformational structures with $\mathrm{tr}M < 0$ in a fast, elastically dominated startup shear protocol. This criterion suggests that a strong stress overshoot of an initially homogeneous flow can play a role as a trigger to the onset of the transient shear-banding irrespective of constitutive instabilities.

Carter and coworkers [54] further applied the linear stability analysis to large amplitude oscillatory strain (LAOStrain) and large amplitude oscillatory stress (LAOStress) shear flows and reproduced similar results (Fig. 1.6). As each cycle of LAOS flow at low

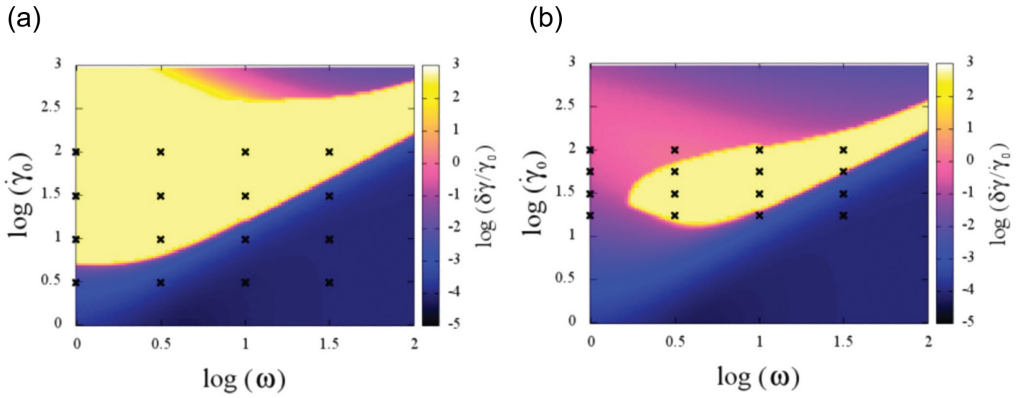

Figure 1.6: Linear stability analysis to predict the normalized degree of shear-banidng under LAOStrain flows for the non-stretching form of the Rolie-Poly model, reproduced from Ref. [54]. The non-stretching Rolie-Poly model is a simpler version of the Rolie-Poly model that assumes instantaneous chain retraction in the limit of $\tau_R \to 0$. The normalized degree of shear-banding is mapped in a parameter space of the normalized imposed strain rate amplitude ($\dot{\gamma}_0$) and frequency (ω). (a) With a underlying non-monotonic constitutive curve, $\beta = 0.4$. (b) With a underlying monotonic constitutive curve, $\beta = 1.0$, where the steady shear banding is precluded.

frequencies is analogous to sweeping shear rates slowly up and down while the sheared fluid remains at a (quasi-)steady state, Eq. (1.9) is used to predict the linear instability. LAOS at higher frequencies can be compared to repeating fast shear start-up protocols where a strong stress overshoot of the shear stress versus strain curve is the trigger, so Eq. (1.10) is used instead. Therefore, the LAOS protocol allows rheologists to explore time-dependent as well as time-independent shear-banding by varying shear frequencies, which can be a very useful experimental framework to study both types of shear-banding flows.

Linear stability studies using phenomenological models were also performed to study edge fractures in complex fluids by Hemingway and coworkers [55–57]. They modeled a boundary condition depicting a fluid-air interface and analyzed how the perturbations

arising from the interface propagate in the diffusive Johnson-Segalman model and diffusive Giesekus model. They suggested a criterion for an initially flat interface to develop edge fracture [55]:

$$\frac{1}{2}\Delta\sigma\frac{d|N_2|}{d\dot{\gamma}}\Big/\frac{d\sigma}{d\dot{\gamma}} > \frac{2\pi\Gamma}{L_y}, \tag{1.11}$$

where $\Delta\sigma$ is the jump in shear stress across the fluid-air interface, N_2 is the second normal stress difference, σ is the fluid shear stress (T_{xy}), Γ is the surface tension of the interface, and L_y is the gap. This criterion has an implication for a better design of flow geometries to prevent edge fracture, which is a crucial limiting factor in rheology of fast flows of complex fluids. For example, immersing the flow cell in a bathing fluid will be helpful as the jump in the shear stress ($\Delta\sigma$) can be reduced. More importantly, they further extended the discussion to predict that even a mild edge disturbance that would be hardly noticed experimentally can penetrate deep inside a flow cell to display apparent shear-banding velocity profiles [56, 57]. Since the edge fracture was one of the heatedly debated topics about validity of Wang's early experiments [37–39], it will be also worthwhile to verify whether the experimentally observed shear-banding in polymer solutions is free from the effect of edge instabilities.

The models mentioned above are one-fluid models in the sense that they assume a spatially homogeneous concentration field. Whereas they can provide universal criteria for steady (Eq. (1.9)) and transient (Eq. (1.10)) shear-banding, they preclude experimentally observed concentration fluctuations of polymer solutions subjected to a flow which are often hinted by increased turbidity. They also discard the steady shear-banding of polymer solutions with a monotonic constitutive equation [58]. Flow-concentration coupling which indicates a large concentration fluctuation and polymer migration against concentration gradient has been proposed as another possible mechanism of shear-banding in entangled polymer solutions, and two-fluid model has been

suggested to account for the effect.

Initial motivation of two-fluid model was to understand experimental reports that high-molecular weight polymers can have a spatially nonuniform concentration profile. For instance, Dill and Zimm [59] found that DNA molecules of different lengths can be effectively separated in co-centric cylinders as their centripetal migration velocities toward the device axis show power-law dependence of molecular weight. Metzner and coworkers [60] found that polymer chains in a dilute and a semi-dilute regimes migrate across streamlines when subjected to a Poiseuille flow. MacDonald and Muller [61] sheared a dilute polystyrene solution in a cone-plate geometry and observed a higher concentration near apex and a lower concentration near edge.

Helfand and Fredrickson [62] formulated a phenomenological theory for the dynamics of concentration fluctuations of polymer chains under a simple shear flow. They found a coupling between stress and concentration fluctuations as a result of concentration-dependence of viscosity and normal stress coefficients. Goveas and Fredrickson [63] introduced this concept into the shear-banding material for the first time. They considered a binary mixture of chemically identical polymers that obey Rouse dynamics, which can be realized by mixing polymers of an identical type with two different molecular weights that are shorter than the entanglement molecular weight. In their study, however, the driving force for the chain migration requires curved streamlines and their model system is different from the entangled polymers. Later, Cromer and coworkers [3, 64, 65] constructed a two-fluid model with a solvent and a polymer as two interpenetrating fluids. Concentration/stress coupling was incorporated into the Rolie-Poly model with a underlying monotonic constitutive curve. They claimed to qualitatively reproduce all the experimental findings of shear-banding which cannot be explained by traditional nonmonotonic constitutive models, including the steady shear banding with a monotonic constitutive curve and ramping history dependence of the finally reached

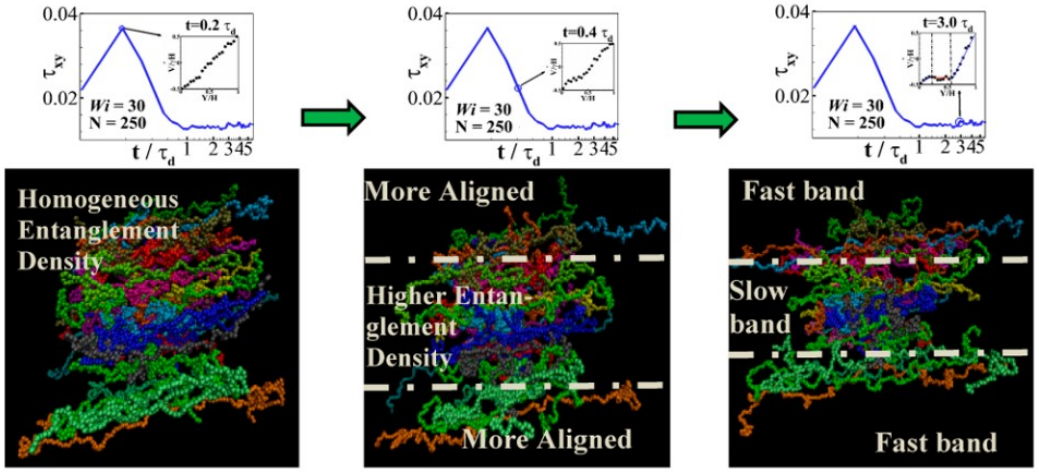

Figure 1.7: An example of molecular dynamics simulations for startup shear of entangled polymer melts, reproduced from Ref. [67]. Evolution of molecular structures at different stages (stress peak, downhill of the overshoot, steady-state) was studied.

steady state [40, 41]. They also predicted a higher polymer concentration in the low-shear-rate band and a lower polymer concentration in the high-shear-rate band. This trend is opposite to an early observation by Callaghan and Gil [26] where the polymer concentration measured by ^{1}H NMR intensity appeared higher in the high-shear-rate band while it agrees with a prediction by another two-fluid approach [58]. Peterson and coworkers [66] further added isotropic elastic contributions to the two-fluid Rolie-Poly model and predicted additional linear instability at Wi higher than the stress plateau regime. They also suggested that much longer time is needed to reach a steady state in a Taylor-Couette cell as the gap is widened, but changes in a velocity profile and a concentration profile should be noticeable at an early stage.

Molecular dynamics (MD) simulation can provide information about single molecular level changes in chain conformation associated with development of the shear-banding flows (Fig. 1.7). Cao and Likhtman [68] reported the first observation of shear-banding in MD simulations of entangled polymer melts. In their computation, a simple bead-spring chain consisting of purely repulsive Lennard-Johnes beads connected by finitely extensible nonlinear elastic (FENE) springs with a slight bending potential, combined with a dissipative particle dynamics (DPD) thermostat, was tested as a model polymer system. The authors observed the shear-banding for a relatively low entanglement number ($Z = 10$) and attributed it to the chain stiffness, which has an implication for experiments using semi-flexible or rigid polymers that have a fewer Kuhn segments in the entanglement length. Mohagheghi and Khomami [67, 69–71] conducted MD simulations to study molecular processes leading to shear-banding in polymer melts. They rationalized that the flow-induced disentanglement and insufficient orientational relaxation due to fast imposed deformation cause heterogeneous entanglement densities and local variations in fluid properties along the shear-gradient direction, leading to strain inhomogeneity and finally formation of the shear-banded structure. While MD simulation can provide plausible explanations about microscopic origins of the shear-banding in entangled polymer melts, a high computational cost has limited its application only to the idealized flow geometry. The effect of solvent has been omitted so far, and it will need to be accounted for to understand situations in polymer solutions.

As briefly reviewed so far from historical perspectives, there have been debates about the shear-banding in polymer solutions and melts despite being the very first complex fluid system predicted to develop shear-banding flows. Many mechanisms and models have been proposed to rationalize experimentally observed shear-banding flows in polymer solutions, which require experimental validations. In this dissertation, we carefully examine and rule out possible sources of experimental artifacts such as edge

fractures, mis-alignment of shear plates or curvature in the stream line. By using a large-aspect-ratio, curvature-free, gap adjustable confocal shear cell, we try to verify the existence of shear-banding in polymer solutions without ambiguity and provide insights into the microscopic structural origins that trigger the flow behavior.

1.2 Overview of contributions

The objective of the present research is to resolve the long-standing controversy about the presence of shear banding in entangled polymers, and provide insights into its microscopic origins. The major contributions of this dissertation are summarized as follows.

- Chapter 2 explores experimental parameters affecting the measured shear profiles. In specific, a highly entangled ($Z \approx 300$) DNA solution will be prepared and characterized. LAOS will be applied with a fixed strain ($\gamma_0 = 1.5$) to the sample solution with varying H and shearing frequency f. The degree of wall slip and shear-banding will be quantified and mapped onto the parameter space. As the shear-banding profile develops, the embedded tracer particles will be tracked to extract information of spatially distinct microscopic structures in the two bands. We find transient super-diffusive dynamics of tracers in the high-rate-band which can be characterized by Lévy-walk-type motion. We also measure dynamic heterogeneity in the two bands.

- Chapter 3 investigates the effect of edge disturbances on the internal shear-banding flow profiles, and verify if the measured profile in Chapter 2 was a true property or an apparent behavior affected by the edge instabilities. The velocity profiles near the edges deviate from the shear profile measured inside but they approach to the bulk profile as we observe deeper inside the sample solution. We define a penetration length (δ) as the distance over which the deviation decays to a

measurement noise level. In the flow-direction of the shear-banding solution, we find abnormally long $\delta = 20\ H$, an order of magnitude larger than a typical penetration length H. The bulk shear-banding profile is recovered beyond δ where the edge effect diminishes, and it indicates its true bulk nature.

- Chapter 4 studies DNA-bridged colloidal particle dumbbell dynamics in the two shear-bands. Compared to Chapter 2, the dumbbell has a rotational degree of freedom, and the DNA linkers are deformable and entangled with background polymers. We measure orientational distribution and translational/rotational dynamics. The dumbbells in the high-shear-rate band display stronger alignment along the flow direction and enhanced translation/rotation. Moreover, a coupling between translational and rotational dynamics and the correlation between inter-particle separation and translation. Our result suggests that low viscosity zones allowing translation, rotation, and chain stretching are formed in the high-shear-rate band.

Chapter 2

Shear-banding and superdiffusivity in polymer solutions

Using high-resolution confocal rheometry, we study the shear profiles of well-entangled DNA solutions under large amplitude oscillatory shear (LAOS) in a rectilinear planar shear cell. With increasing Weissenberg number (Wi), we observe successive transitions from normal Newtonian linear shear profiles to wall-slip dominant shear profiles and finally to shear-banding profiles at high Wi. To investigate the microscopic origin of the observed shear banding, we study the dynamics of micron-sized tracers embedded in DNA solutions. Surprisingly, tracer particles in the shear frame exhibit transient super-diffusivity and strong dynamic heterogeneity. The probability distribution functions of particle displacements follow a power-law scaling at large displacements, indicating a Lévy-walk-type motion, reminiscent of tracer dynamics in entangled wormlike micelle solutions and sheared colloidal glasses. We further characterize the length and time

scales associated with the abnormal dynamics of tracer particles. We hypothesize that the unusual particle dynamics arise from localized shear-induced chain disentanglement.

2.1 Introduction

Shear banding, namely the coexistence of multiple shear rates in a sheared sample, has been observed in numerous complex fluids such as worm-like micelle solutions [72, 73], concentrated colloidal suspensions [74, 75], low-density attractive colloidal gels [76], dense assemblies of soft microgels [77] and granular materials [78]. Due to its fundamental importance in understanding the response of materials under large and fast shear deformations, shear banding has been a persistent focus of rheological studies [47,48,79,80]. Although entangled linear polymers were predicted to display shear banding over 30 years ago based on the then newly developed Doi-Edwards theory [2], the existence of shear banding in entangled linear polymers remains under debate. Experimental evidence supporting the existence of shear banding in entangled linear polymers was first reported by Wang and coworkers under both steady and time-dependent shear conditions [24, 27, 30, 32, 33, 41, 81, 82]. However, subsequent studies suggested that the observed banding flows may arise from the edge fracture in cone-plate rheometers and/or experimental artifacts [36–38, 40, 83, 84]. Although the controversy has not been fully settled [42, 85–87], these experimental findings have aroused intensive numerical and theoretical investigations that attempt to rationalize the existence of shear banding [3, 52, 64, 67–70, 88]. Mechanisms including shear-induced concentration fluctuations [3, 64, 88], localized chain disentanglements [67, 69, 70] and transient instabilities triggered by stress overshoot in shear startup [52, 68, 70] have been proposed for the possible existence of shear banding in entangled polymeric fluids.

In spite of the theoretical progress, important experimental questions remain open,

largely contributing to the on-going controversy. First, can one observe shear banding in polymeric fluids after ruling out possible experimental defects? If so, what are the microscopic dynamics of polymer shear-banding flows? Here, we address these two fundamental questions by using a high-resolution rheo-optical apparatus designed to avoid experimental artifacts [85, 86]. Our experiments directly verify the existence of shear banding in highly entangled polymer solutions under planar large amplitude oscillatory shear (LAOS). Moreover, we find that the dynamics of polymer solutions in the two co-existing bands differ substantially. In the high shear-rate band, embedded tracer particles exhibit a Lévy-walk type of motion and a transient super-diffusive behavior with a high degree of dynamic heterogeneity. Long temporal correlations but short-range spatial correlations are observed for the abnormal dynamics of tracer particles. Such unusual tracer dynamics provide important insights into the origin of the shear-banding flows in polymeric fluids and suggest localized shear-induced chain disentanglement.

2.2 Materials and methods

2.2.1 Sample preparation and characterization

Our experiments use calf thymus DNA (double-stranded, 75 kbp, 4.9×10^7 g/mol, Affymetrix) as our model polymer. Solutions of calf thymus DNA were prepared in an aqueous 2× TBE buffer (180 mM Tris base, 180 mM Boric acid, 5.6 mM EDTA). The buffer strongly screens electrostatic interactions, so that DNA molecules behave similarly to neutral semi-flexible polymers [89]. The moderate pH (≈ 8) maintained by the buffer also prevents the denaturation of DNA. We added fluorescently-tagged, carboxy-terminated polystyrene (PS) micro-beads (radius $a = 0.55$ μm, Thermo Fisher Scientific) in the DNA solution as tracer particles. The volume fraction of PS spheres is kept so low ($< 0.03\%$) that the interaction between tracers can be safely ignored.

The final concentration of DNA was confirmed using a UV/Vis spectrometer (NanoDrop, Thermo Scientific). In the shear-banding experiments, the concentration of DNA was fixed at 8.3 ± 0.4 mg/mL. Based on a previous study using λ-DNA [90], the overlap concentration of λ-DNA in a high ionic strength buffer is $c^* = 0.064$ mg/mL. As $c^* \approx 3M/(4\pi R_g^3 N_A) \sim M^{1-3\nu}$, where M is the molecular weight, R_g is the radius of gyration, N_A is the Avogadro number and $\nu = 3/5$, we estimated $c^* = 0.051$ mg/mL for our samples of calf thymus DNA. Thus, the DNA concentration used in our experiments is two orders magnitude larger than c^*, ensuring a high degree of chain entanglement.

We estimated the tube parameters from the linear viscoelasticity of the solution. Frequency sweep experiments under small amplitude oscillatory shear (SAOS) were conducted using a commercial cone-plate rheometer (AR-G2, TA Instruments) (Fig. 2.1). We used time-temperature superposition to obtain the final result. We chose G' at the frequency where the loss tangent $\tan\delta$ is minimal as the plateau modulus, $G_N^0 \approx 100$ Pa. The average number of entanglements per chain (Z) was calculated by Ferry's temporary network formula [91],

$$Z = \frac{5}{4}\frac{M}{M_e} = \frac{5}{4}G_N^0(cRT)^{-1} \approx 300, \tag{2.1}$$

where $c = 8.3$ mg/mL. Thus, the mesh size of the polymer network is about 90 nm based on Z. Reptation time was given by the reciprocal overlap frequency when $G' = G''$, $\tau_d \approx 900$ s. Finally, the Rouse relaxation time is $\tau_R = \tau_d/(3Z) \approx 1$ s [92]. Thanks to the long contour length of DNA molecules, we can achieve a high entanglement at a relatively low DNA concentration so that the elastic modulus of the solution is sufficiently small for us to load and shear the sample [30, 81, 82]. However, due to the slow relaxation at such a high DNA concentration, we could not reach the terminal relaxation regime even at the lowest frequency of our rheometer.

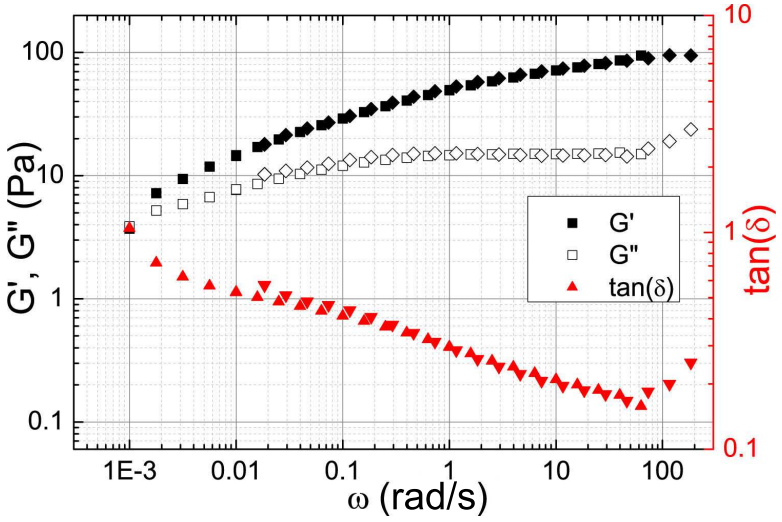

Figure 2.1: Linear viscoelasticity of a highly-entangled DNA solution. The storage modulus (G'), the loss modulus (G'') and the loss tangent ($\tan\delta$) were measured in a frequency sweep under SAOS. Solid squares and diamonds are for G'. Empty squares and diamonds are for G''. Solid triangles (up-pointing and down-pointing) are for $\tan\delta$. The results were used to determine the relevant tube parameters τ_d, τ_R, G_N^0 and Z. Squares and up-pointing triangles were obtained at the room temperature 23 °C, whereas diamonds and down-pointing triangles were taken at 13 °C and shifted to the room temperature using the principle of time-temperature superposition.

Since the non-uniformity of DNA concentration in a solution may trigger shear banding flows [64, 88], we test the uniformity of our high-concentration DNA solutions in three different ways. First, we take a small volume ($\sim$ 2 μL) of DNA solution from a concentrated sample at five different, well-separated positions in a sample vial. UV/Vis measurements are then made at least five times for the solution taken at each position. The variation of the measured concentrations is within 5% of the average concentration, indicating that both the device measurement error and the spatial concentration variation are reasonably small in our experiments. Second, we also measure the velocity profiles at low Weissenberg number (Wi) (f = 0.1 Hz). Presumably, if a sample is locally heterogeneous, we would observe non-uniform shear deformations of the sample at low Wi. Furthermore, the diffusion of DNA molecules due to the concentration gradient would result in the change of shear profiles over time. We find that the velocity profiles of our samples are always stable and linear, again indicating a good uniformity of the solutions. Lastly, sample homogeneity can also be qualitatively checked from the distribution of PS tracer particles. As mentioned above, we seed a small amount of fluorescent PS tracers in DNA solutions for flow visualization. After slowly stirring the solution for mixing, any aggregated particle clusters in the original solution are well dispersed. The uniformity of the particle distribution is directly confirmed from microscope images, which again suggests the uniformity of DNA concentrations after stirring.

2.2.2 Experimental setup

Figure 2.2 shows the schematic of our experimental setup. A small amount of the highly-entangled DNA solution (20 μL) is loaded in a custom shear cell. The shear cell has a rectilinear plane-plane geometry with a square top plate of length L = 5 mm made of an etched silicon wafer and a much larger bottom plate made of a normal

microscope coverslip. While the top plate is kept stationary, the bottom plate is driven by a piezoelectric actuator, which exerts a sinusoidal oscillatory shear in the sample confined between the two plates following $\gamma_0(t) = (A_0/H)\sin(2\pi ft)$ (Supplementary Video 1). Here, A_0 is the applied shear amplitude, f is the applied shear frequency, and H is the gap size between the top and bottom plates. In our experiments, we keep $H \leq 100$ μm such that the aspect ratio of the shear cell is large with $L/H \geq 50$. The detailed description of the setup can be found in Refs. [93, 94]. The corresponding Weissenberg number based on the Rouse relaxation time is Wi $= (A_0/H)$De, where De $= 2\pi\tau_R f$ is the Deborah number of large amplitude oscillatory shear (LAOS). The shear cell is coupled to a fast inverted spinning-disk confocal microscope for high-resolution flow field visualization [93, 94].

Before each of our measurements, we allow the sample to equilibrate in the shear cell without shear for at least 30 minutes, about twice as long as τ_d. An oscillatory shear is then applied at the desired shear frequency and strain amplitude for another 30 minutes. The preshear allows the sample reach a steady state before measurements. Videos are then taken at different heights above the moving plate and analyzed with Particle Image Velocimetry (PIV) (Supplementary Video 1). The confocal microscope scans two-dimensional images at 200 frames per second. These images have an area of 100×100 μm^2 when a 60× lens was used, and 300×300 μm^2 when a 20× lens was used, which typically contain a few hundred tracer particles in the field of view. An image sequence containing two to four shear cycles is taken at each height y before the focal plane is adjusted a different y either manually or automatically. The time for adjusting the focal plane is irrelevant, since the shear velocity at each height is analyzed separately and our sample has reached the steady state before measurements. At each height, the peak velocity of the oscillatory shear is determined by applying Fast Fourier Transformation (FFT) to the velocity as a function of time. We typically measure

velocities at 10 different heights to construct one shear profile. Three shear profiles are measured for the sample at a given shear condition. The final shear profile is an average of these three independent experimental runs. Error bars reflect the variation of the three measurements.

Our setup shares the same advantage as the confocal-rheoscopic device introduced in Ref. [31], where high-resolution imaging of velocity profiles within narrow gaps was achieved. However, Ref. [31] applies steady shear to entangled polybutadiene solutions in a rotational rheometer. Here, we used a planar Couette cell, which eliminates stress inhomogeneity and streamline curvature that may potentially trigger shear banding [47]. Indeed, the rectilinear shear cell with a large aspect ratio L/H provides an ideal geometry excluding or significantly reducing potential experimental artifacts [36,40] such as the curvature of material lines, secondary flows and thermal and edge effects [85,86].

Lastly, we discuss the influence of the shear boundary. (1) For the vertical shear boundary, in all the experiments reported in this article, the bottom shear plate is made of a normal microscope coverslip. The top shear plate is constructed from a silicon wafer. The wafer is roughened by reactive-ion etching, where we use 40 sccm CF_4 and 4 sccm O_2 at pressure 100 mtorr and power 100 W. The etching time is slightly less than one minute. From atomic force microscopy (AFM), the roughness of the wafer surface is 34.5 ± 1.7 nm, calculated based on the root-mean-squared heights. Symmetric shear boundaries with both the top and bottom plates made of glass coverslips have also been tested, which yield qualitatively similar behavior (results not shown). (2) For the lateral boundary condition, the perimeter of the cell is left open. Samples overflow outside the shear cell laterally and are held fixed by the capillary force at the contact line with the bottom plate. Since the confined gap of the shear cell is much smaller than the lateral dimension, we do not expect the lateral boundary condition strongly affects the flow profile of samples at the center of the cell [85,86], where we conduct all

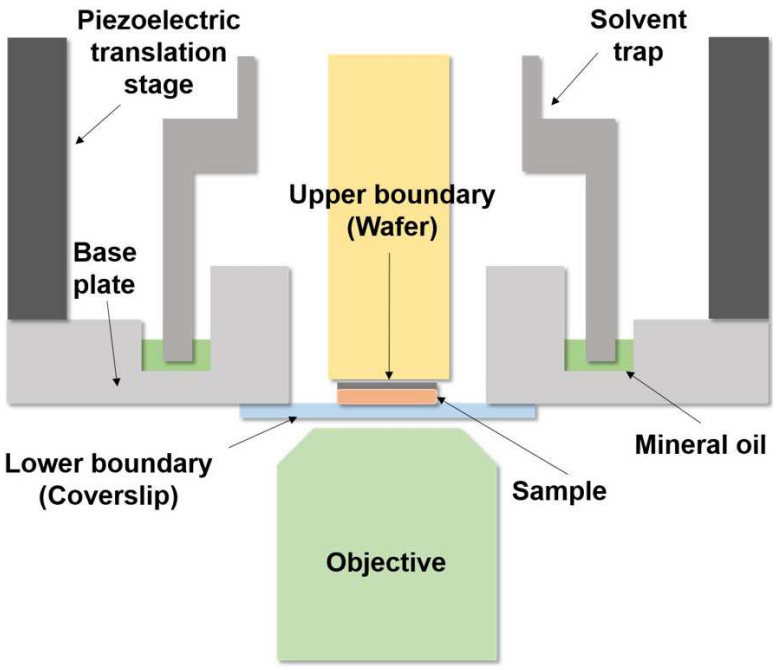

Figure 2.2: Schematic of the experimental setup. The area of the wafer is 5×5 mm^2. The thickness of the sample is 100 μm. While the wafer is fixed, the coverslip is moved by the piezoelectric stage, which induces a linear shear in the confined sample. The solvent trap creates a sealed chamber, preventing the evaporation of the solvent. An inverted confocal microscope (represented here by the objective) is used for imaging the shear flow within the sample.

our measurements. Rheological measurements have indeed shown that the influence of the lateral boundary on the shear profile only extends into the sample on the order of the gap thickness [95], which is far away from the center of the cell. A similar geometry has been adopted before in studying the shear profile of polymer samples without shear banding [85, 86]. It is worth noting that although the measurements on velocity profiles at the center of the cell are not affected by the lateral boundary, rheological measurement of the stresses may be affected depending on the boundary condition. This is because stress measurements average all the samples in the cell including those near the lateral boundary. To further test the influence of the edge, we measure the shear profiles at different gap thicknesses in the small gap limit for semi-dilute DNA solutions. The profiles are all linear as expected without any perceptible influence from the lateral boundary.

2.3 Results

2.3.1 Shear banding of entangled DNA solutions

To probe the response of highly entangled DNA solutions under large amplitude oscillatory shear (LAOS), we vary the gap thickness of our shear cell, H, and the shear frequency, f, while keeping the strain amplitude fixed at $\gamma_0 = 1.5$.

Figure 2.3 illustrates typical behaviors of the DNA solution under different shear conditions. For comparison, we also show the usual linear velocity profile of a semi-dilute DNA solution at the overlap concentration. For the entangled DNA solution at the high concentration, the sample shows a strong, asymmetric wall slip near the moving bottom plate at low f (low Wi). A stronger slip occurs at the moving bottom plate of a smooth glass coverslip. In contrast, the slip at the stationary top plate made of a roughened silicon wafer is much weaker. The applied strain is relaxed dominantly

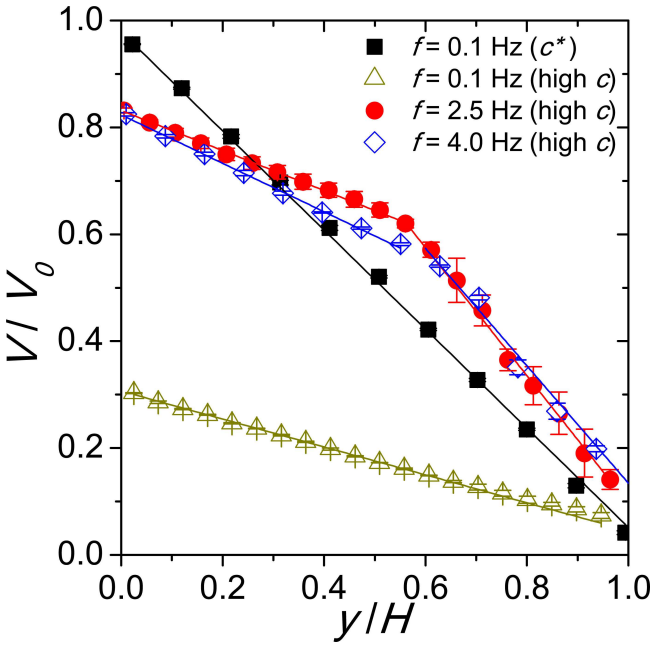

Figure 2.3: Normalized velocity profiles of DNA solutions under shear. Black squares are for a semi-dilute DNA solution at the overlap concentration $c^* = 0.05$ mg/mL. Others are for the high concentration, entangled DNA solution. Solid lines indicate piecewise linear fits. A Cartesian coordinate system is defined, where x, y and z are the flow, shear gradient and vorticity directions, respectively. Velocity amplitudes, $V(y)$, are normalized by the velocity amplitude of the moving plate, $V_0 = 2\pi f A_0$ with $A_0 = 150$ μm.

through the local yielding of a thin layer of DNA molecules near the moving plate. As a result, the local shear strain in the bulk of the material γ is much smaller than γ_0. The wall-slip dominant linear velocity profile eventually turns into clear shear-banding profiles at higher f (higher Wi), which show small but comparable wall slips at both plates. This trend is qualitatively similar to the results from the Wang group [24]. In addition, we also observe the similar trend when using monodisperse λ-DNA (data not shown). As such, our experiments with a high-resolution confocal rheoscope directly demonstrate the existence of shear banding in entangled DNA solutions in rectilinear shear under LAOS.

To quantify the shape of the velocity profiles, we fit the profiles piecewisely with linear lines (Fig. 2.3). A banding parameter can then be defined as the difference between two shear rates relative to the applied shear rate, $|\dot{\gamma}_h - \dot{\gamma}_l|/\dot{\gamma}_0$, where $\dot{\gamma}_{h,l}$ are the shear rates of the high and low shear-rate bands, respectively. $\dot{\gamma}_0 = V_0/H = 2\pi f\gamma_0$ is the applied shear rate, where V_0 is the velocity amplitude of the moving plate. Furthermore, to characterize the degree of wall slip, we measure the slip lengths of a velocity profile at both the stationary and moving plates by extrapolating the profile to the non-slip velocities at 0 and V_0. The normalized average slip length is then calculated using $(b_h + b_l)/2H$, where $b_{h,l}$ are the slip lengths at the stationary and moving plates, respectively.

Based on the banding parameter and the slip length, we map a detailed phase diagram for the shear response of entangled DNA solutions under LAOS (Fig. 2.4). Fig. 2.4 shows that shear banding flows are more favorable when the degree of wall slip is small. With increasing $\dot{\gamma}_0$ and H, linear profiles with strong wall slips gradually give away to shear-banding flows. Shear banding and wall slip are complementary to each other. Following the previous study by Wang and co-workers [24], we also plot the banding parameter in terms of Wi and the slip parameter in Fig. 2.4c. The result again

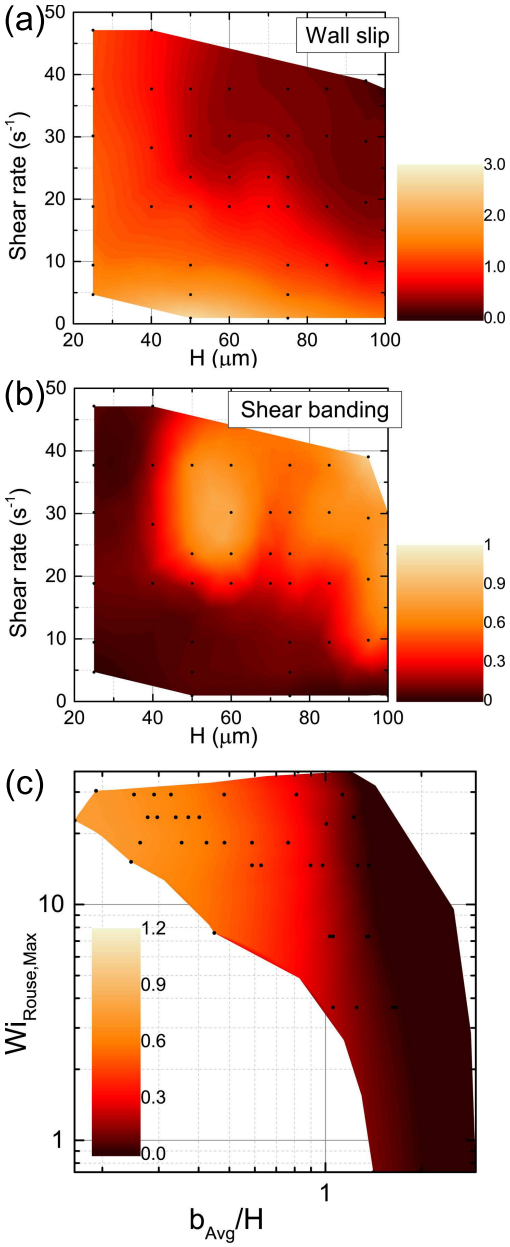

Figure 2.4: The amplitude of shear strain is fixed at $\gamma_0 = 1.5$. (a) Contour map of the wall-slip parameter, $(b_h + b_l)/2H$, at different shear rates $\dot{\gamma}_0$ and gap thicknesses H. Solid disks correspond to our experimental points. (b) Contour map of the shear-banding parameters, $|\dot{\gamma}_h - \dot{\gamma}_l|/\dot{\gamma}_0$, from the same experiments. (c) Contour map of the shear-banding parameter in terms of Wi and the slip parameter, $b_{avg}/H = (b_h + b_l)/2H$.

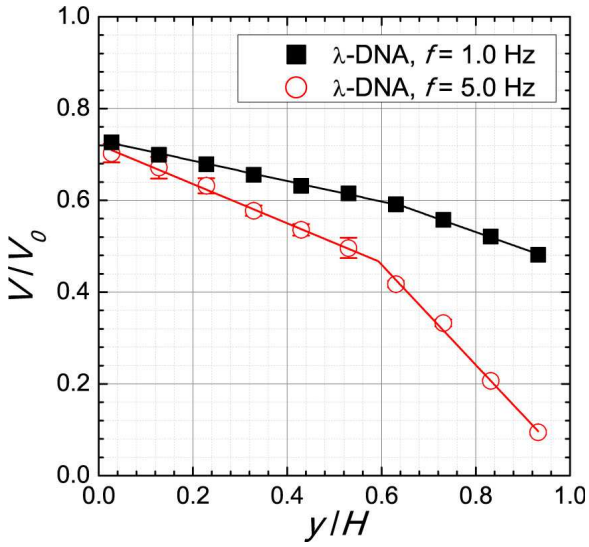

Figure 2.5: Shear banding in a λ-DNA solution. The concentration of DNA is 5.4 ± 0.4 mg/mL, about two orders magnitude higher than the overlap concentration. The strain amplitude is $\gamma_0 = 2.0$ and the gap thickness is $H = 75$ μm. At low shear frequency $f = 1.0$ Hz, the velocity profile shows strong wall slip (black squares). At high shear frequency $f = 5.0$ Hz, a clear shear banding flow emerges (red circles). Solid lines are piecewise linear fits.

demonstrates that shear banding sets in when wall-slip is suppressed and Wi is large.

We also tested the effect of polydispersity on the formation of shear banding using monodisperse λ-DNA. Due to the high cost of λ-DNA, we cannot afford to systematically map the phase diagram (Fig. 2.4). Nevertheless, we did confirm that under large shear strain and frequency, a highly entangled λ-DNA solution shows strong shear banding flows. Furthermore, jumpers with superdiffusive motions were also observed in the high shear-rate band. A typical shear-banding flow in a highly entangled λ-DNA solution is shown in Fig. 2.5.

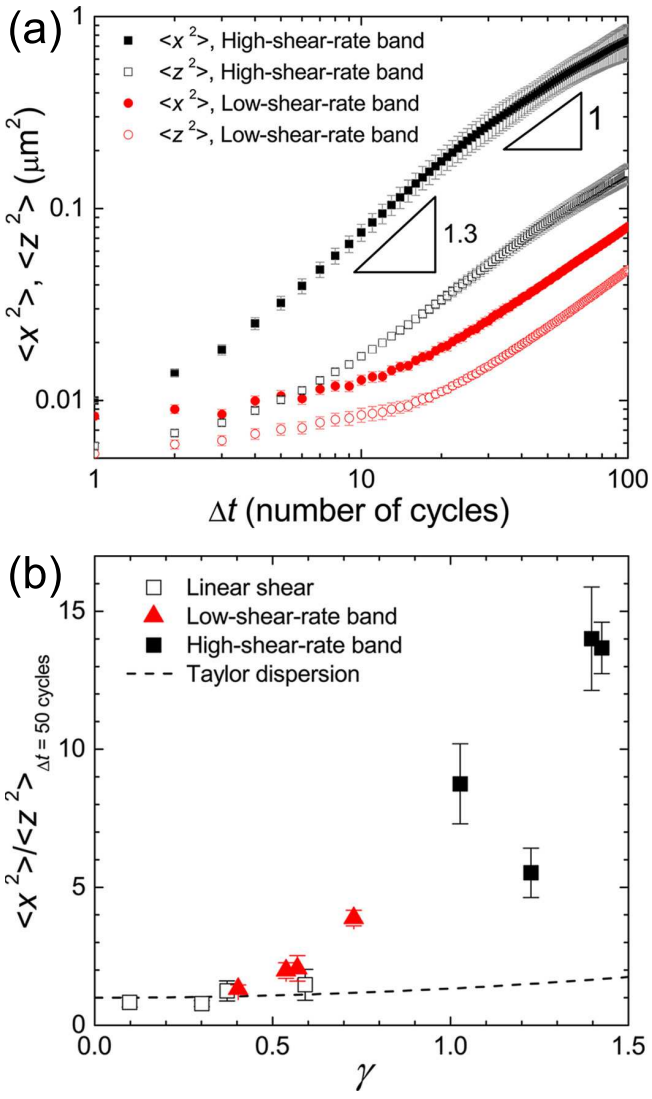

Figure 2.6: Dynamics of particles in the shear frame. (a) Mean-squared displacements (MSDs) of particles along the flow (x) and vorticity (z) directions in the two co-existing shear bands. The slopes indicate the superdiffusive motion of particles at intermediate times and the diffusive motion at long times. (b) The ratio of MSDs, $\langle x^2 \rangle / \langle z^2 \rangle$, at $\Delta t = 50$ cycles versus local shear strains, γ. The dashed line indicates the prediction of Taylor dispersion. Different γ are achieved by varying A_0 while keeping $f = 4$ Hz.

2.3.2 Super-diffusivity of tracer particles

To explore the microscopic dynamics of the shear banding flow, we shall focus on the behavior of the solution at high Wi with fixed $f = 4$ Hz (De ≈ 25) and $A_0 = 120$ μm (Wi ≈ 30). In the lab frame, the average sinusoidal motion of tracer particles dominates (Supplementary Video 1), allowing us to accurately extract the velocity profiles (Fig. 2.3). In order to reveal the fluctuation of particle dynamics around the mean shear flow, we acquire images of the tracer particles in the shear frame at a frequency equal to f, so that a sequence of strobed images of the tracer particles are taken at the same phase of successive shear cycles (Supplementary Videos 2 and 3). For imaging convenience, we choose the phase at $\pi/2$ where $\gamma_0(t)$ is largest. Fig. 2.6a shows the mean-squared displacements (MSDs) of particles in the shear frame in the two co-existing shear bands, respectively. Particles diffuse faster in the high shear-rate band close to the stationary plate, indicating a lower effective shear viscosity in that band, consistent with the overall velocity profile (Fig. 2.3). In both the low- and high shear-rate bands, a strong anisotropy in particle dynamics is observed. Particles exhibit faster dynamics along the direction of the shear flow. Quantitatively, we plot the ratio of MSDs along the flow (x) and vorticity (z) directions, $\langle x^2\rangle/\langle z^2\rangle$, at $\Delta t = 50$ cycles under different shear conditions, where particles show clear long-time diffusions (Fig. 2.6b). $\langle x^2\rangle/\langle z^2\rangle$ increases with the amplitude of local shear strains γ. At low Wi, when the velocity profile is linear, the ratio follows the prediction of the classic Taylor dispersion with $\langle x^2\rangle/\langle z^2\rangle = 1 + \gamma^2/3$ [96]. However, the prediction fails in the shear banding flow, especially in the high shear-rate band, where particle dynamics in x are more strongly enhanced.

More interestingly, particles in the high shear-rate band show a transient superdiffusive motion when $\Delta t = 3$ to 20 cycles (Fig. 2.6a), where $\langle x^2\rangle \sim \Delta t^\alpha$ with $\alpha = 1.41 \pm 0.13$

obtained from an average of 25 independent experimental runs. Similar transient superdiffusivity has also been observed in stationary worm-like micelle solutions [97] and in sheared dense colloidal suspensions [75,98]. Indeed, one can easily identify the particles with anomalous fast motions in Supplementary Video 3, taken in the high shear-rate band. A fraction of the particles jump over a large distance along x within a short time interval, Δt, whereas other particles hardly diffuse within the same Δt. In sharp contrast, no such jumpers can be observed in the co-exiting low shear-rate band close to the moving plate (Supplementary Video 2). We also observe a small fraction of jumpers next to the walls when there is a strong wall slip.

We further quantify the anomalous particle dynamics by plotting the probability distribution functions (PDFs) of the displacements of particles along the flow direction, Δx, over $\Delta t = 20$ cycles (Fig. 2.7a). While PDF of particles in the low shear-rate band can be well described by a Gaussian distribution, the jumpers in the high shear-rate band give rise to long power-law tails in the PDF at large Δx, indicating a Lévy walk of the jumpers [97,99]. Such an observation inspires us to fit the PDFs using

$$\mathrm{PDF}(\Delta x) = \frac{(1-w)}{\sqrt{2\pi\sigma^2}} e^{-\frac{\Delta x^2}{2\sigma^2}} + \frac{w(1+\mu)\sin\left(\frac{\pi}{1+\mu}\right)}{2\pi\left(1+|\Delta x|^{1+\mu}\right)}, \tag{2.2}$$

where the first term gives the Gaussian core at small Δx with a standard deviation σ and the second term gives the distribution of the Lévy walk with $\mathrm{PDF}(\Delta x) \sim \Delta x^{-(1+\mu)}$ at large Δx. The power-law exponent of the distribution $1 \leq \mu < 2$ is linked to the anomalous diffusion exponent $\mathrm{MSD} \sim t^{3-\mu}$ [99]. We find $\mu = 1.45 \pm 0.17$ in the PDF, agreeing with the MSD measurements. The weighting factor, $w(y) \in [0,1]$, gives the relative contribution of the two distributions and, therefore, can be used to quantify the fraction of jumpers. We plot $w(y)$ in both the linear and nonlinear shear flows (Fig. 2.7b). Jumpers are not observed in the linear shear flow except near the wall with

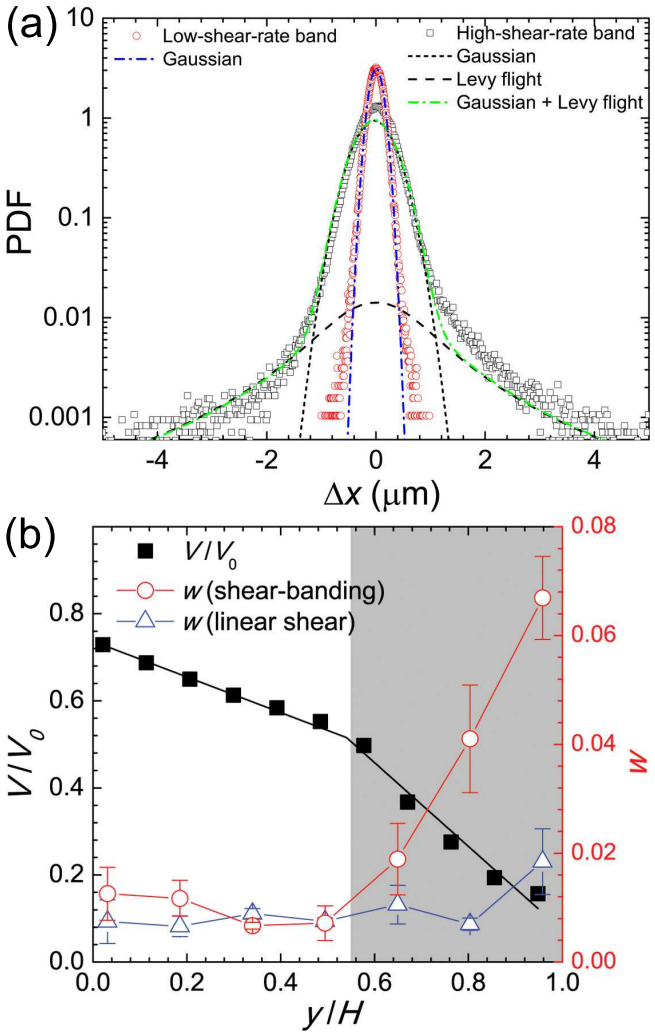

Figure 2.7: Lévy walk of tracer particles. (a) Probability distribution functions (PDFs) of particle displacements over 20 shearing cycles in the high and low shear-rate bands. PDF in the low shear-rate band is fitted by a Gaussian distribution. PDF in the high shear-rate band is fitted by Eq. (2.2). (b) The fraction of jumpers performing the Lévy walk, w, at different heights. The corresponding velocity profile is shown for comparison. The shaded area indicates the high shear-rate band. The fraction of jumpers in the sample with a linear velocity profile at $A_0 = 37.5$ μm (Wi ≈ 9.4) is also shown.

wall-slip. Although the fraction of jumpers is also low in the low shear-rate band of the shear-banding flow, it increases sharply in the high shear-rate band, consistent with our direct observation.

The co-existence of fast jumpers and slow diffusive particles reveals a strong dynamic heterogeneity in the sheared solution. We quantify this dynamic heterogeneity by measuring a four-point susceptibility $\chi_4(t) = N\left[\langle q_s(t)^2\rangle - \langle q_s(t)\rangle^2\right]$, where $q_s(t)$ is the self-overlap function of particles [100]: $q_s(t) = (1/N)\sum_{i=1}^{N} w\left(|x_i(t) - x_i(0)|\right)$ with $w = 1(0)$ if $|x_i(t) - x_i(0)| < (>)a$. Here, $x_i(t)$ is the position of the tracer particle i at time t and N is the total number of tracer particles. $\chi_4(t)$ measures the standard deviation of particle dynamics quantified by $q_s(t)$; a larger χ_4 corresponds to a stronger dynamic heterogeneity. $\chi_4(t)$ at different heights in the shear-banding flow are shown in Fig. 2.8a. Strong dynamic heterogeneities emerge in the high shear-rate band at the intermediate time scales, coincident with the superdiffusive regime in the MSDs (Fig. 2.8a). The well-defined peak of $\chi_4(t)$ is reminiscent of particle dynamics in crowded environments near the glass transition [100]. Quantitatively, we compare the peak value of χ_4, $\chi_{4,p}$, in different shear bands (Fig. 2.8b). It is clear that strong dynamic heterogeneities only develop in the high shear-rate band of the shear-banding flow, consistent with the presence of the jumpers in Fig. 2.7b. Note that the heterogeneous dynamics at micron scales strongly limit the possibility of a secondary flow triggered by the edge failure as the origin of the anomalous particle dynamics and, for that matter, the shear banding in our LAOS experiments [36, 40]. Unless microscopic vortices of tens of microns—the average spacing between jumpers and diffusers—were formed in the secondary flow, the flow would lead to uniform particle drift at this small scale.

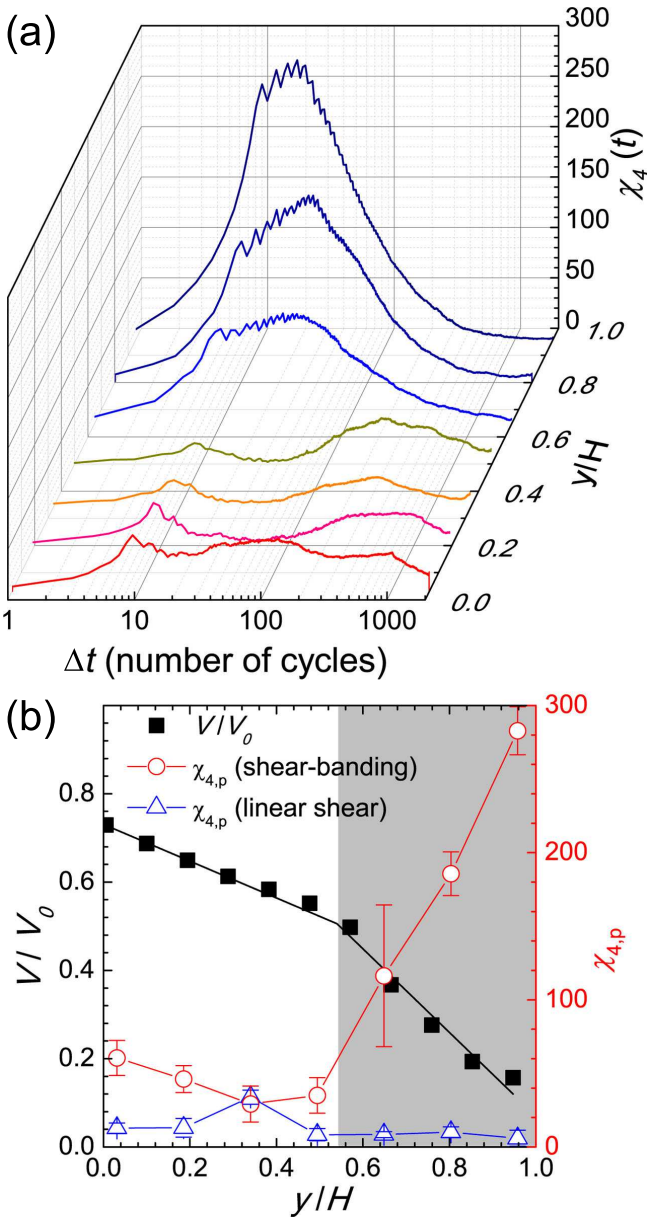

Figure 2.8: Dynamic heterogeneity of tracer particles. (a) Four-point susceptibility, $\chi_4(t)$, at different heights in the shear-banding flow. (b) The peak value of $\chi_4(t)$, $\chi_{4,p}$, at different heights. The corresponding shear-banding velocity profile is shown for comparison. The shaded area indicates the high shear-rate band. $\chi_{4,p}$ for the sample with a linear shear profile at $A_0 = 50$ μm (Wi ≈ 12.5) is also shown.

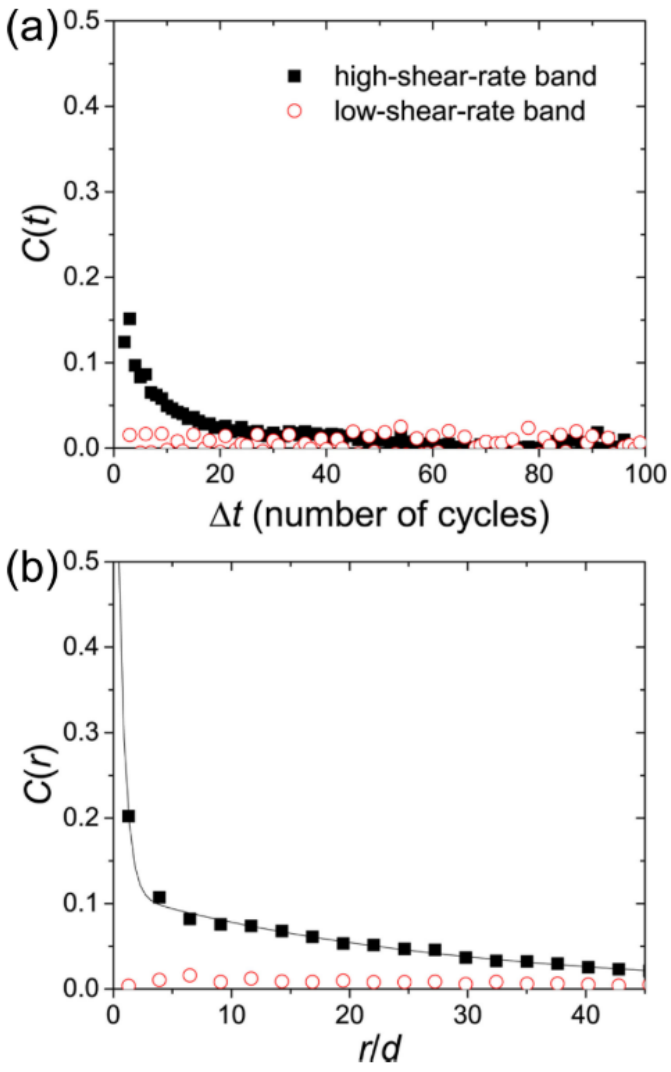

Figure 2.9: (a) The autocorrelation of particle velocities, $C(t)$, in the in the low- and high shear-rate bands. (b) The spatial correlation of particle velocities, $C(r)$, in the low and high shear-rate bands. The radial distance r is normalized by the diameter of tracer particles $d = 1.1\mu$m. The solid line indicates a double-exponential fit.

2.3.3 Correlation of the jumper dynamics

The dynamics of jumpers in the high shear-rate band exhibit interesting spatiotemporal features. Some jumpers sustain slow drifts over multiple cycles after performing a large leap and finally turning back into normal diffusion (Supplementary Video 3). Moreover, neighboring jumpers may show strong correlated motions. To extract the associated time and length scales of jumper dynamics, we measure the temporal and spatial correlations of jumper dynamics. The results reveal crucial information on the underlying dynamics of the sheared entangled polymer network.

We obtain the trajectories of jumpers using Particle Tracking Velocimetry (PTV), where we define a particle as a jumper when its maximal displacement over one cycle within the entire trajectory is larger than one particle diameter. The autocorrelation of jumper dynamics, $C(t)$, can be written as,

$$C(t) = \frac{\langle \boldsymbol{v_i}(t_0) \cdot \boldsymbol{v_i}(t_0 + t) \rangle_{i,t_0}}{\langle \boldsymbol{v_i}(t_0) \cdot \boldsymbol{v_i}(t_0) \rangle_{i,t_0}}, \tag{2.3}$$

where $\boldsymbol{v_i}(t_0)$ is the velocity of particle i at time t_0 given by $[\boldsymbol{r_i}(t_0 + 1) - \boldsymbol{r_i}(t_0)]$ and t is the time difference in terms of the number of cycles. The average is taken over all particles $i = 1, N$ and all t_0. For comparison, we also calculate $C(t)$ for particles in the low shear-rate band. Whereas particles in the low shear-rate band show no temporal correlation as expected for normal diffusion (Fig. 2.9a), jumpers in the high shear-rate band show a weak but long correlation with a time constant $\tau = 11.2 \pm 1.7$ cycles.

We also quantify the spatial correlation of jumper dynamics. We find the spatial correlation is isotropic in the flow-vorticity plane. Thus, we define the spatial correlation, $C(r)$, based on the radial variable r alone as

$$C(r) = \frac{\langle \boldsymbol{v}(\boldsymbol{r_i}, t_0) \cdot \boldsymbol{v}(\boldsymbol{r_j}, t_0) \rangle_{i,j,t_0}}{\langle \boldsymbol{v}(\boldsymbol{r_i}, t_0) \cdot \boldsymbol{v}(\boldsymbol{r_i}, t_0) \rangle_{i,t_0}}, \tag{2.4}$$

where i and j are indices denoting tracer particles and $r = |\boldsymbol{r_i} - \boldsymbol{r_j}|$. The average is taken over all the particle pairs and the initial time t_0. Similar to the autocorrelation, diffusers in the low shear-rate band show almost zero spatial correlation as expected (Fig. 2.9b). The spatial correlation of jumpers in the high shear-rate bands shows a more interesting behavior. With increasing r, a strong short-range correlation is followed by a much weaker but long-range correlation. Accordingly, we fit $C(r)$ using a double-exponential decay $C(r) = A\exp(-r/l_s) + (1-A)\exp(-r/l_l)$. The strong short-range correlation gives a length scale $l_s = 0.81 \pm 0.23$ μm, which is about 0.75 particle diameters or 10 mesh sizes, whereas the weak long-range correlation shows a length scale $l_l = 30.2 \pm 2.6$ μm, comparable to the width of the high shear-rate band. The existence of two different spatial correlation length scales can be observed in Supplementary Video 3.

2.4 Discussions

The superdiffusivity and dynamic heterogeneity of tracer particles provide important insights into the microscopic polymer dynamics under shear. We hypothesize that the abrupt motion of jumpers arises from localized shear-induced chain disentanglement and the breakage of local entangled polymer network. The motion of tracer particles is strongly constrained by the local entangled mesh of DNA chains. If the shear deformation is affine and the dense mesh of chains that regulates the tracer motion is intact, the positions of tracers with respect to the local entangled network should remain the same (assuming the diffusion of tracers is negligible). This explains our observations in the low shear-rate band, where particles barely move. We argue that the observed abnormal dynamics of jumpers in the high shear-rate band is possible only if the mesh network around the region containing jumpers experiences entanglement failure and deforms in a non-affine manner. The event releases the shear stress built up around jumpers induced

by the non-affine deformation of the network around the particles, which pushes the particles out of the entangled "cage", i.e., the local constraints imposed by the entangled polymer network on the particles. Although the associated length scale $l_s = 0.82$ μm is 10 times larger than the mesh size, it is small enough to safely exclude the influence of global effects such as the secondary flow on the correlation of particle motions [36, 40]. Nevertheless, it is not clear if the long-range correlation at the scale of l_l is induced by the secondary flow. If this long-range correlation indeed arises from the secondary flow, why does the secondary flow concentrate only in the high shear-rate band? Hence, our hypothesized "localized disentanglement" should be understood on the scale of l_s. Within this hypothesis, the polymer solution should have a lower degree of entanglement in the high shear-rate band and, therefore, exhibit a lower viscosity, a picture consistent with a recent numerical finding [67]. Moreover, the presence of jumpers and the small χ_4 peak near the shear plates with strong wall slip (Figs. 2.7b and 2.8b) indicate shear-induced chain disentanglement near the boundary, consistent with previous theories on wall slip, where apparent slip occurs due to the disentanglement of polymer chains near the wall [101]. This observation suggests a common origin of shear banding and wall slip [24, 47].

Independent of the validity of the hypothesis, our results on unusual tracer dynamics provide a solid experimental benchmark for testing microscopic theories of the rheology of concentrated polymeric fluids. Our results also pose further questions and directions. First, it is important to theoretically understand the time and length scales of jumper dynamics and, particularly, the two different length scales of the spatial correlation of jumper dynamics. Second, it is not clear why the fraction of jumpers and the dynamic heterogeneity increase continuously with height, rather than plateauing, in the high shear-rate band (Figs. 2.7b and 2.8b). Last, it is also interesting to verify if shear banding exists in steady shear flows [33] and measure the corresponding shear-induced

particle dynamics. For LAOS at small De approaching the limit of steady shear, our sample shows a strong wall slip (Fig. 2.4), preventing us from testing the possible steady-state shear banding. Future experiments with rough shear plates and higher solvent viscosity may help to reduce the degree of wall slip and allow us to probe this interesting regime.

2.5 Summary

We studied the response of concentrated DNA solutions under LAOS using a custom high-resolution rectilinear confocal shear cell. The setup allows us to avoid potential experimental artifacts and experimentally verify the existence of shear-banding in highly entangled polymer solutions under LAOS. Moreover, we found that the embedded tracer particles in the shear-banding polymeric fluids display markedly different dynamics in the two co-existing shear bands. While particles in the low shear-rate bend show normal diffusive motions, particles in the high shear-rate band exhibit transient super-diffusivity, obeying the distribution of Lévy walks. A high degree of dynamic heterogeneity were also observed exclusively in the high shear-rate band. We quantitatively analyzed the associated length and time scales of abnormal particle dynamics. We hypothesized that these dynamic features are associated with shear-induced chain disentanglement and breakage of local entanglement network in the high shear-rate band, although it is not clear if such a microscopic picture can quantitatively predict the length and time scales of tracer particles. This poses a theoretical challenge for the future work.

Chapter 3

Effect of edge disturbance on shear banding in polymer solutions

Edge instabilities are believed to be one of the possible causes of shear banding in entangled polymeric fluids. Here, we investigate the effect of edge disturbance on the shear-induced dynamics of well-entangled DNA solutions. Using a custom high-aspect-ratio planar-Couette cell, we systematically measure the velocity profiles of sheared DNA samples at different distances away from the edge of the shear cell. Under a weak oscillatory shear with the corresponding Wi smaller than 1, where DNA solutions exhibit linear velocity profiles with strong wall slip, the penetration depth of the edge disturbance is on the order of the gap thickness of the shear cell, consistent with the behavior of Newtonian fluids. However, under a strong oscillatory shear with Wi >1 that produces shear-banding flows, the penetration depth is an order of magnitude larger than the gap thickness and becomes spatially anisotropic. Moreover, we find

that the shear-banding flows persist deep inside the sheared sample, where the effect of edge disturbance diminishes. Hence, our experiments demonstrate an abnormally long penetration depth of edge disturbance and illustrate the bulk nature of shear-banding flows of entangled polymeric fluids under time-dependent oscillatory shear.

3.1 Introduction

Under strong shear, an entangled polymeric fluid can develop heterogeneous flow profiles with multiple bands of different shear rates [24, 102]. Such shear-banding behavior has attracted great research interests in recent years. Although the experimental evidence for shear-banding in entangled polymeric fluids has accumulated in different polymer systems under various shear protocols, including steady and start-up shear and time-dependent oscillatory shear [32, 33, 42, 44, 45, 82], the origin of these shear-banding flows is still under heated debate [36, 38, 84–86]. It is still controversial as to whether the observed shear banding flows arise from an underlying non-monotonic constitutive relation between shear stress and shear rate [2, 4, 22], confirmation of which would modify our current understanding of the dynamics of entangled polymer chains. The value of the key parameters in the models of entangled polymer fluids such as the convective constraint release (CCR) parameter in the GLaMM model need to be revisited [22]. To accommodate shear banding within the framework of the existing polymer theory, several alternative scenarios have been proposed, including strong flow-concentration coupling [64, 88], localized chain disentanglements [67, 69] and long-lived transient instabilities triggered by stress overshoot [52, 68]. In particular, edge instabilities in the form of surface disturbances and edge fractures have been suggested as a likely cause of shear banding [36, 38, 39, 56, 103].

To mitigate the influence of edge instabilities, shear-banding experiments with sample edges wrapped in plastic films [82], in large-aspect-ratio shear cells with small gaps [31, 44, 104, 105] and using a special cone-partitioned-plate rheometer [27] have been conducted. However, it is still debatable whether these procedures truly eliminate the edge instabilities [38]. Indeed, a recent numerical study showed that even a mild surface disturbance of shear-thinning polymeric fluids, which may go experimentally unnoticed, leads to strong secondary flows and apparent shear banding [56]. The secondary flows induced by the edge instability can penetrate deep into sheared samples up to 10–20 gap thicknesses H. These surprising results challenge not only the view of shear banding of polymeric fluids as a bulk phenomenon, but also the validity of conventional rheological characterization of strong shear-thinning polymeric fluids where the aspect ratio of shear cells W/H is usually comparable to or smaller than the normalized penetration depth L/H. Inspired by the numerical study of Hemingway and Fielding, we experimentally investigate the effect of edge instabilities on the shear banding profile of entangled polymeric fluids.

Here, instead of minimizing edge instabilities, we use a custom-designed high-aspect-ratio planar shear cell to systematically probe the influence of edge disturbance on the shear-induced dynamics of entangled polymeric fluids. Specifically, we directly measure the shape variation of the velocity profile of entangled polymeric fluids as a function of the distance away from the edge. We find that the penetration depth of edge disturbance is on the order of H when the shear profile is linear, even with strong wall slip, similar to the behavior of Newtonian fluids. However, when shear-banding profiles develop, we observe a strong deviation from the bulk flow profile far away from the edge with a penetration depth an order of magnitude larger than H. The result is qualitatively similar to the prediction of Ref. [56], even though different boundary condition and shear protocol were adopted in simulations. A long penetration depth seems to be

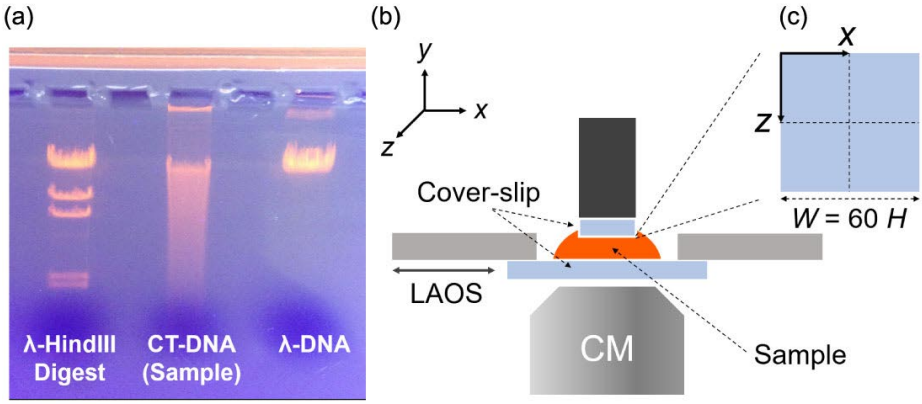

Figure 3.1: Experimental setup. (a) Gel electrophoresis of calf thymus DNA solution (center). The results from λ-DNA fragments (left, digested by HindIII restriction enzyme) and monodisperse λ-DNA (right, 48.5 kbp) are also added for comparison. All the DNA samples were prepared in the same TBE 2X buffer. (b) Schematic showing our custom planar-Couette cell (not to scale). CM: confocal microscope. A sheared sample is confined between two microscope coverslips with a fluid reservoir outside the cell. The gap thickness between the two coverslips is $H = 100$ μm. (c) Top view of the top shear plate. The horizontal and vertical dashed lines indicate the two directions, along which we probe the edge effect.

a generic feature for strong shear thinning polymer fluids, independent of boundary conditions and shear protocols. We furthermore find that the penetration depth is spatially inhomogeneous with a longer penetration along the flow direction. Under the condition of our experiments, the shear-banding flows persist deep inside entangled polymeric fluids when the edge effect vanishes, which thus eliminates edge disturbance as the origin of shear banding in our experiments. As such, our experiments reveal profound effects of boundary and edge on the velocity profiles of sheared complex fluids.

3.2 Materials and methods

3.2.1 Sample preparation and characterization

We used calf thymus DNA (double-stranded, average molecular weight 75 kbp, 4.9×10^7 g/mol, Affymetrix) as our model polymer, which exhibited strong shear-banding flows under large amplitude oscillatory shear (LAOS) in Ch. 2 [45, 82]. Calf thymus DNA is less monodisperse compared with λ-DNA as shown in gel electrophoresis (Fig. 3.1a). The exact polydispersity depends on the specific method used for extracting DNA from calf thymus tissues and is not known from the vendor. Concentrated aqueous DNA solutions were prepared in 2× TBE buffer (180 mM Tris base, 180 mM Boric acid, 5.6 mM EDTA). The buffer sufficiently screens the electrostatic interactions between DNA chains [106]. As a result, the DNA molecules behave similarly as neutral semi-flexible chains. We fixed the concentration of DNA at 8.3 mg/ml in this study, which is 160 times the overlap concentration.

A standard rheological characterization of the DNA solution under small amplitude oscillatory shear was performed using a commercial cone-plate rheometer (AR-G2, TA Instruments). The plateau modulus of the solution is $G_N^0 \approx 100$ Pa at 23 °C. The average molecular weight of DNA molecules is calculated from the average chain length, $M = 7.5 \times 10^4$ bp $\times$ 650 Da/bp $= 4.9 \times 10^7$ g/mol. Thus, the average number of entanglement points per chain, Z, can be estimated as $Z = (5/4)MG_N^0/(cRT) \approx 300$. Furthermore, the reciprocal of the overlap frequency at $G' = G''$ gives the reptation time $\tau_d = 900$ s. The Rouse relaxation time $\tau_R = \tau_d/3Z = 1$ s. The mesh size of the entangled network is about 90 nm. R_g of our calf thymus DNA is 0.72 μm, which is estimated based on R_g of λ-DNA (48.5 kbp, 32 MDa) [90]. To track shear flows, we added a small amount of fluorescently-tagged polystyrene particles (< 0.03 wt%) with radius 0.55 μm in the solution for particle imaging velocimetry (PIV). The tracer particle is more than

12 times larger than the entanglement strand. The average distance between particles is 8.3 μm, which is about $11R_g$.

3.2.2 Experimental setup

Our setup is a custom planar-Couette cell, consisting of two parallel plates made of microscope coverslips (Fig. 3.1). The coverslip glass is made of borosilicate from Thermo Fisher Scientific. The original dimension of the coverslips is 18×18 mm^2 and the thickness is labeled as #1 (0.13 – 0.17 mm). The coverslips were then cut to the right shape and size suitable as the top and bottom plates of the shear cell. The top plate is square with edge size $W = 6$ mm, whereas the bottom plate is circular with a much larger diameter of 12.8 mm. We washed the surface of the top and bottom plates with ethanol and water before each experiment to remove residual solutions and dust. Three differential screws located at the vertices of an equilateral triangle were used to adjust the level of the top plate relative to that of the bottom plate. The degree of parallelism was checked by measuring the distances between the top and bottom plates at the four corners of the square top plate using confocal microscopy. By finely tuning each screw with different amounts, one can achieve a good control of the level of the top plate with an accuracy of 1 μm over 6 mm. The overall height of the gap can be lowered or increased by twisting the three screws together. More details about the design and the function of the setup can be further found in Ref. [94].

During experiments, the top plate was held stationary, while the bottom plate was driven sinusoidally by a piezo actuator. We fixed the gap thickness between the top and the bottom plates at $H = 100$ μm, equivalent to $\sim 140R_g$, so that a high aspect ratio of $W/H = 60$ is maintained in our study. A DNA solution of volume $v = 15$ μL was loaded into the shear cell before each experiment. Since v is larger than the confined volume between the two shear plates, the solution outflows the edge of the top plate and forms

a pinned contact line on the bottom plate. Hence, our experiments have a "drown" edge with a fluid reservoir outside the shear cell (Fig. 3.1b), a geometry frequently used in rheological measurements [74, 94, 107–109]. The shear cell was placed on a fast inverted confocal microscope for visualization of 3D flow profiles.

We define a coordinate system so that the flow, flow gradient and vorticity directions are along x, y and z, respectively (Fig. 3.1). The plane at $y = 0$ indicates the position of the moving bottom plate, whereas the stationary top plate is at $y = H$. Since the bottom plate is driven sinusoidally with oscillatory velocity $V_0 \sin(2\pi f t)$, the flow at any location (x, y, z) within the shear cell simply follows $v(x, y, z, t) = V(x, y, z) \sin(2\pi f t + \delta)$. Here, f is the shear frequency and V_0 is the applied velocity amplitude of the sinusoidal oscillatory shear, which is related to the amplitude of the displacement, A_0, via $V_0 = 2\pi f A_0$. In our study, we fixed $A_0 = 150$ μm and the corresponding shear strain $A_0/H = 1.5$, which gives $V_0 = 3.77$ mm/s at $f = 4$ Hz and 0.094 mm/s at $f = 0.1Hz$. The phase shift δ is zero in our experiments.

At fixed x and z, $V(y)$ defines the velocity profile of sheared samples. We measure $V(y)$ at different locations along the bisector of the edge of the top plate either in the flow direction at $z = W/2$ (Fig. 3.2b inset) or in the vorticity direction at $x = W/2$ (Fig. 3.5b inset). We typically start the measurements from the edge and move gradually inward to the center of the sheared sample, although reversing the direction of experiments yields quantitatively the same results. For each $V(y)$ measurement, we take a video of four shearing cycles at a fixed y and then scan different y positions to obtain the entire velocity profile at given x and z. These measurements are repeated three times, which are averaged to give the average velocity profile for the given sample. It takes $\sim$ 1 minute to obtain one average velocity profile at high f. Finally, three different samples are tested to yield the final results reported below. To remove the possible effect of sample loading, for each new sample, we preshear the sample at high shear

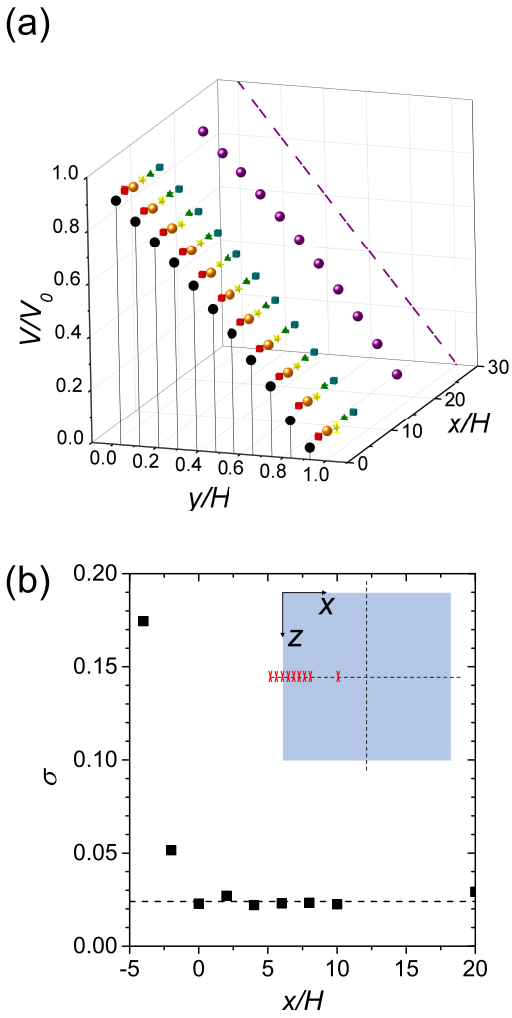

Figure 3.2: Shear profiles of a glycerol/water mixture. Applied shear velocity amplitude $V_0 = 3.77$ mm/s. Shear frequency $f = 4.0$ Hz. De $= 2\pi\tau_{\mathrm{R}}\mathrm{f} = 25$ (a) Shear profiles, $V_x(x, y)$, at different locations x. x and y are normalized by H, whereas V_x is normalized by V_0. From the front to back, $x/H = 0$, 2, 4, 6, 8, 10 and 20. The dashed line indicates the linear profile of a Newtonian fluid satisfying no-slip boundary conditions. (b) Standard deviation of the shape of shear profiles, σ, versus x/H. Intrinsic errors are indicated by the dashed line. Inset shows the top view of the top shear plate. Red crosses indicate the locations where the velocity profiles are measured.

rates for 15 min and let it rest for another 30 min before the start of the velocity profile measurements.

Two dimensionless numbers can be constructed to quantify the dynamics of the DNA solution under oscillatory shear. The Weissenberg number (Wi) of a shear is defined as $\mathrm{Wi} \equiv \tau_{\mathrm{R}} \mathrm{V}_0/\mathrm{H}$. The Deborah number (De) is defined as $\mathrm{De} \equiv 2\pi \mathrm{f} \tau_{\mathrm{R}}$, where τ_R is the Rouse relaxation time of DNA chains. For Wi and De defined based on the reptation time τ_d, one can simply multiply the above definition of Wi and De by $3Z = 900$.

3.3 Results and discussion

3.3.1 Validation of the experimental setup with a Newtonian solution

To validate our experimental protocol, we first measure the edge effect on a glycerol/water mixture (21/79 wt%), which is a Newtonian fluid with viscosity 1.7 mPa·s. Velocity profiles of the mixture at different x along the flow direction with $z = W/2$ are shown in Fig. 3.2a. As expected, $V(y)$ in the bulk of the sheared sample is linear. To quantify any deviation of the shape of the velocity profiles from the linear profile, we calculate the standard deviation of the shape variation of the velocity profiles as

$$\sigma(x,z) = \left[\frac{1}{H} \int_0^H \left(\frac{V(x,y,z) - \hat{V}(y)}{V_0} \right)^2 dy \right]^{1/2} \tag{3.1}$$

$$\hat{V}(y) = \lim_{W/H \to \infty} V\left(x \equiv \frac{W}{2}, y, z \equiv \frac{W}{2} \right),$$

where $\hat{V}(y)$ is the velocity profile in the bulk without the influence of edge disturbance, which will be approximated in our study by a linear or piecewise linear fit to the velocity profile at $x = W/2$ and $z = W/2$ far away from the edge. For Newtonian fluids, $\hat{V}(y)$ is well known with $\hat{V}(y) = V_0(1 - y/H)$. We find that $\sigma(x, W/2)$ decreases sharply with

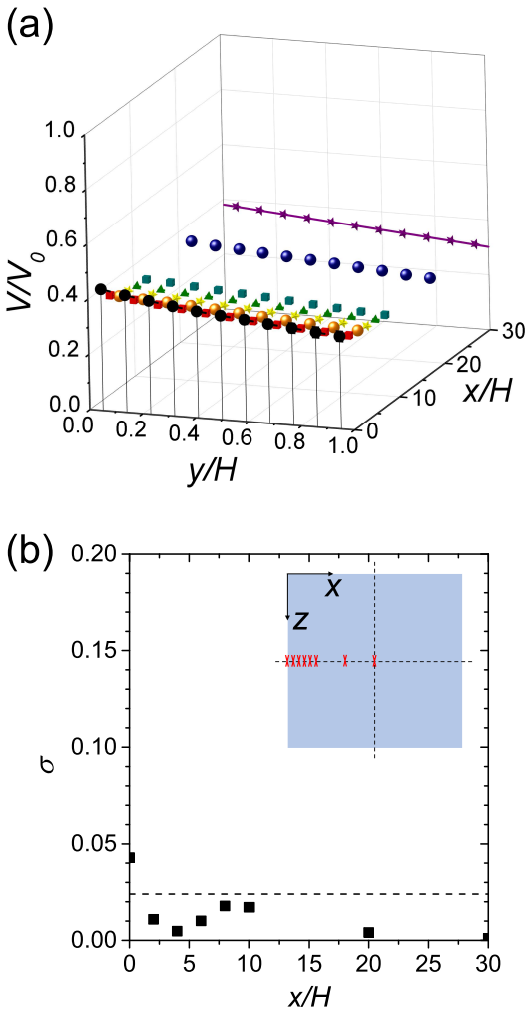

Figure 3.3: Shear profiles of entangled DNA solutions at low Wi. Applied shear velocity amplitude and frequency are $V_0 = 0.094$ mm/s and $f = 0.1$ Hz, respectively. Wi $= 0.9$ and De $= 0.6$. (a) Shear profiles, $V_x(x, y)$, at different locations x. From the front to back, $x/H = 0$, 2, 4, 6, 8, 10, 20 and 30. At all positions, the shear profiles are linear with significant wall slips. Linear fitting is applied to the profile at $x/H = 30$. (b) Standard deviation of the shape of shear profiles, σ, versus x/H. Intrinsic errors are indicated by the dashed line. Inset shows the top view of the top shear plate. Red crosses indicate the locations where the velocity profiles are measured.

x and reaches a constant $c = 0.024$ almost immediately when we move into the shear cell with $x \geq 0$ (Fig. 3.2b). Note that in our experiments, we also measure $V(x, y, z)$ outside the shear cell at negative x. The constant c reflects intrinsic velocity fluctuations and errors of our PIV analysis, independent of edge disturbance. Accordingly, the penetration length, L, can be experimentally defined as the distance beyond which σ consistently lies below the noise threshold. In other words, $\sigma(x = L) = c$. For the glycerol/water mixture, $L < H$, consistent with the known result on the edge effect of Newtonian fluids with a fluid reservoir [107, 108].

3.3.2 Effect of edge disturbance on the shear profiles of the entangled DNA solutions

Next, we measure the shape of the velocity profiles of the entangled DNA solutions. The velocity profiles of concentrated DNA solutions under LAOS have been well studied [24]. Wang and co-workers suggests that the flow behaviors of entangled polymeric fluids can be predicted based on $2b_{max}/H$ and Wi, where b_{max} is the maximal slip length [24]. For a 1 % water-based DNA solution of an average chain length comparable to our system, Boukany et al. shows $2b_{max}/H = 136$, where $H = 1$ mm in their study [29]. Thus, we estimate $2b_{max}/H = 1360$ in our study with $H = 0.1$ mm. The transition Weissenberg number between wall slip and shear banding is given by $\mathrm{Wi}^{\mathrm{Rp}}_{\mathrm{ws-sb}} = 1 + 2\mathrm{b}_{\mathrm{max}}/\mathrm{H} \approx 1360$, where $\mathrm{Wi}^{\mathrm{Rp}}$ is estimated based on the reptation dynamics [24]. The transition Weissenberg number based on Rouse dynamics can be simply calculated as $\mathrm{Wi}_{\mathrm{ws-sb}} = \mathrm{Wi}^{\mathrm{Rp}}_{\mathrm{ws-sb}}/3\mathrm{Z} = 1.5$. Below $\mathrm{Wi}_{\mathrm{ws-sb}}$, one expects to observe wall-slip dominated shear profiles, whereas above $\mathrm{Wi}_{\mathrm{ws-sb}}$, shear banding occurs.

In our experiments, at low $\mathrm{Wi} = 0.9 < \mathrm{Wi}_{\mathrm{ws-sb}}$, we indeed observe the linear profile with strong wall slips in the bulk of the shear cell (Fig. 3.3a). Near the edge, a deviation from the bulk linear velocity profile can be found. Quantitatively, the standard deviation

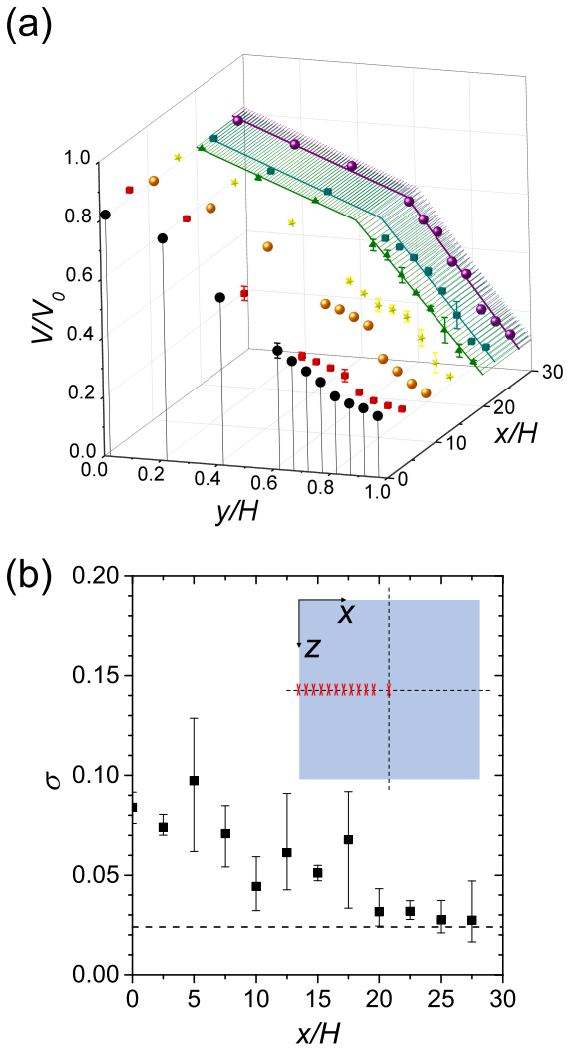

Figure 3.4: Shear profiles of entangled DNA solutions at high Wi. Applied shear velocity amplitude and frequency are $V_0 = 3.77$ mm/s and $f = 4.0$ Hz, respectively. Wi $= 38$ and De $= 25$. (a) From the front to back, $x/H = 0$, 10, 15, 20, 22.5 and 27.5. Piecewise linear fittings are applied to the shear-banding profiles deep inside the sheared sample. (b) Standard deviation of the shape of shear profiles, σ, versus x. Intrinsic errors are indicated by the dashed line. Inset shows the top view of the top shear plate. Red crosses indicate the locations where the velocity profiles are measured.

of the shape variation along the flow direction, $\sigma(x, W/2)$, decreases near the edge and plateaus when $x \gtrsim H$ (Fig. 3.3b). Notice that when calculating σ, we fit the velocity profile of the sheared entangled DNA solution at the center of the shear cell $x = W/2$ and $z = W/2$ using $\hat{V}(y) = V_0(H + l_t - y)/(H + l_t + l_b)$, where the slip lengths at the top and bottom plates, l_t and l_b, are two fitting parameters. Hence, our experiments show that although the entangled DNA solution shows strong viscoelasticity and shear thinning, the penetration depth L is still on the order of H when the velocity profile is linear (albeit with strong wall slips), quantitatively similar to the edge effect on Newtonian fluids.

At high $\mathrm{Wi} = 38 > \mathrm{Wi}_{\mathrm{ws-sb}}$, we also verify the existence of shear-banding flows deep in the sheared entangled DNA solution. The velocity profiles change substantially with x near the edge due to edge disturbance (Fig. 3.4a). In contrast to the case of low Wi, the decrease of $\sigma(x, W/2)$ along the flow direction is much slower with increasing x. The shape of the velocity profiles gradually stabilizes over a surprisingly long distance of $\sim 20H$ (Fig. 3.4b). Here, to calculate σ, we obtain $\hat{V}(y)$ by fitting the shear profile at $x = W/2$ and $z = W/2$ using piecewise linear lines. Thus, our entangled DNA solution displays a penetration depth one order magnitude larger than H, qualitatively agreeing with the numerical finding [56]. However, the long penetration was observed along the vorticity direction, instead of along the flow direction, in simulations. Moreover, different from simulations, the shear-banding profile persists in the bulk of the sheared sample in our experiments. Such differences may arise from different boundary conditions and shear protocols used in simulations and experiments. Indeed, instead of reducing the degree of shear banding, the velocity profile becomes more heterogeneous deeper inside the sample in our experiments (Fig. 3.4a). This observation eliminates the edge disturbance as the possible origin of shear-banding flows in our LAOS experiments.

We also investigate the influence of edge disturbance along the vorticity direction.

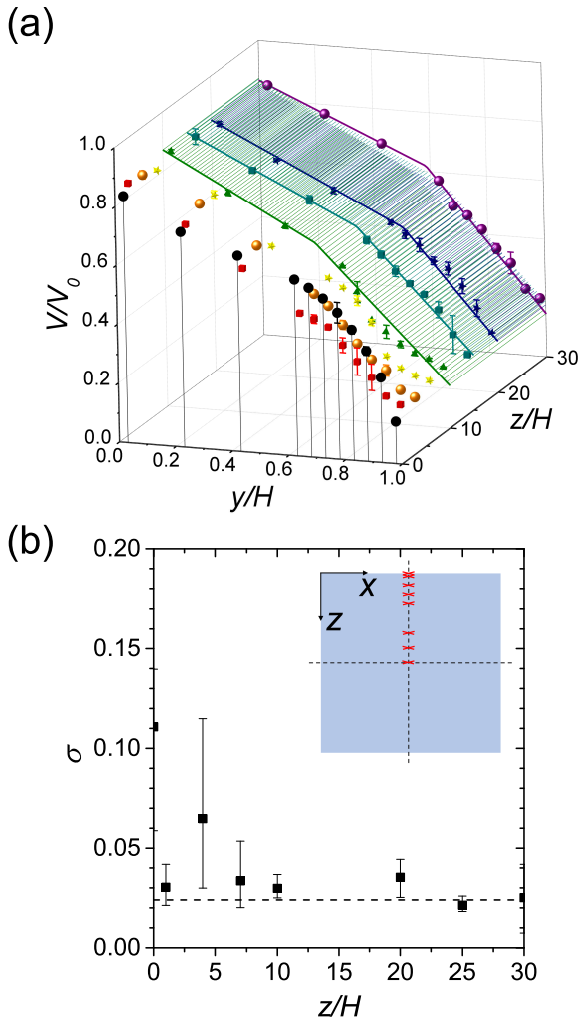

Figure 3.5: Shear profiles of entangled DNA solutions along the vorticity direction at high Wi. Applied shear velocity amplitude and frequency are same as those in Fig. 3.4, $V_0 = 3.77$ mm/s and $f = 4.0$ Hz. Wi = 38 and De = 25. (a) From the front to back, $z/H = 0,\ 1,\ 4,\ 7,\ 10,\ 15,\ 20,\ 30$. Piecewise linear fittings are applied to the shear-banding profiles deep inside the sheared sample. (b) $\sigma(z)$ obtained by comparing each profile to the piecewise linear fitting of the shear-banding profile at $z/H = 30$. Inset shows the top view of the top shear plate. Red crosses indicate the locations where the velocity profiles are measured.

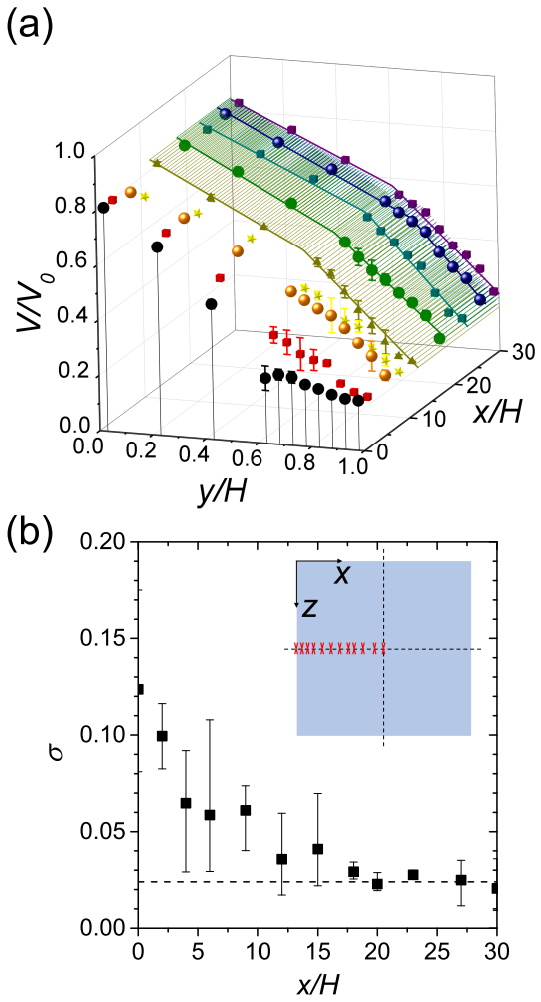

Figure 3.6: Shear profiles of entangled DNA solutions with larger fluid reservoir at high Wi = 38 and De = 25. Applied shear velocity amplitude and frequency are the same as those in Fig. 3.4. Wi = 38. Sample volume $v = 40$ μL. (a) From the front to back, $x/H = 0$, 2, 6, 9, 12, 18, 23, 27, and 30. Piecewise linear fittings are applied to the shear-banding profiles deep inside the sheared sample. (b) Standard deviation of the shape of shear profiles, σ, versus x. Intrinsic errors are indicated by the dashed line. Inset shows the top view of the top shear plate. Red crosses indicate the locations where the velocity profiles are measured.

Specifically, we measure the velocity profiles at different locations z along the bisector of the edge of the top plate normal to the vorticity direction at $x = W/2$ (Fig. 3.5b inset). Figure 3.5a shows the velocity profiles at different z for the entangled polymer solution at high Wi, where strong shear-banding flows are observed deep inside the bulk. Shear banding is again less obvious near the edge of the shear cell, similar to that along the flow direction. However, although the penetration depth along the flow direction is $\sim 20H$ (Fig. 3.4b), the penetration depth along the vorticity direction appears to be much smaller on the order of H (Fig. 3.7). The finding contradicts the numerical result of Hemingway and Fielding, where a long penetration depth is found along the vorticity direction [56]. Since the simulation assumes a translational invariance along the flow direction that eliminates the existence of the x edges, it is not clear if spatially inhomogeneous penetration depths can be detected in the numerical model adopted in [56]. Our result has some interesting implications for conventional rheology measurements. Since the normal direction of the air-fluid interface of sheared samples in a cone-plate rheometer is also along the vorticity direction, edge disturbance may not strongly influence the bulk velocity profiles. However, it should be emphasized that the curvature of the interface in rotational rheometers can also trigger edge instabilities [38, 108], a factor that cannot play a role in our planar shear cell.

3.3.3 Effect of the size of fluid reservoirs

Lastly, we also study the effect of the size of fluid reservoirs on the change of the velocity profiles. A large volume of the DNA solution of $v = 40$ μL is used in this experiment, which gives rise to a significantly larger fluid reservoir compared to those experiments with $v = 15$ μL solutions. Figure 3.6 shows the velocity profiles along the flow direction at high Wi. The shear condition is the same as that used in Fig. 3.4. The results are qualitatively similar as those shown in Fig. 3.4 too; σ decreases near the edge and

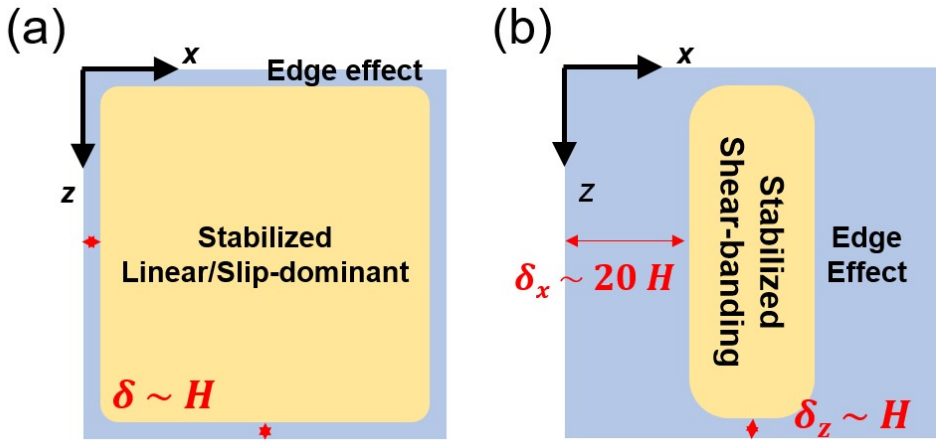

Figure 3.7: A schematic summary of shear profile measurement at various locations. (a) When a sheared sample solution displays a linear bulk velocity profile with or without wall-slip, both δ_x and δ_z are on the order of H. (b) In the entangled polymer solutions at Wi $>>$ 1, stabilized shear-banding velocity profiles are recovered much farther away from the edge in x direction with an abnormally long $\delta_x \approx 20H$ while it is still not strongly affected in z direction with $\delta_z \approx H$.

plateaus around $x = 15H$, which again suggests an abnormal long penetration depth of $L \approx 15H$. Quantitatively, it seems that a larger fluid reservoir leads to a slightly smaller penetration depth, consistent with the expectation for Newtonian fluids [107, 108].

Although inspired by the work of Hemingway and Fielding, our experiments are different from the simulations in two key aspects, which affect the direct comparison between experimental and numerical results. First, we apply large amplitude oscillatory shear (LAOS) instead of steady shear in our experiments. Shear-banding in time-dependent flows may have different origins from steady shear-banding [80]. Hence, although our experiments exclude edge instabilities as the origin of shear-banding in LAOS flows, one should be cautious when extending the same conclusion to steady shear-banding flows [33]. Second, the lateral boundary of our shear cell is different from that of the simulations, where the sheared samples are completely confined between two parallel shear plates. This difference likely explains why we do not observe strong shear banding flows near the edge induced by the edge disturbance. Bulk shear-banding flows emerge only when the effect of edge disturbance diminishes. The shear-banding profiles of entangled DNA solutions are well-established at $x \approx 20H$ away from the edge of the cell.

3.4 Summary

In conclusion, we systematically investigated the effect of edge disturbance on the velocity profiles of highly entangled DNA solutions. In particular, we measured the penetration depth of edge disturbance. Under weak shear with linear shear profiles, the solutions exhibit a short penetration depth comparable to the gap thickness of the shear cell, consistent with our understanding based on Newtonian fluids. However, under strong shear with shear-banding flows, the penetration depth is one order of magnitude larger than

the gap thickness along the flow direction, confirming the existence of an abnormally long penetration of edge disturbance [56]. In addition, we found that the penetration depth is anisotropic. The influence of edge disturbance is significantly deeper along the flow direction than along the vorticity direction. Moreover, a larger fluid reservoir results in a slightly shorter penetration depth, a feature that may be exploited in standard rheological tests of entangled polymeric fluids. Finally, we verified that LAOS exerted in our experiments gives rise to true bulk shear-banding flows without the influence of edge disturbance. Our work illustrates the profound effects of edge disturbance on the sheared dynamics of entangled polymer fluids.

Chapter 4

Dynamics of DNA-bridged dumbbells in shear-banding of entangled polymer solutions

Although experimental evidence for shear-banding flows in highly entangled polymer solutions has accumulated over the last 20 years, the microscopic conformational changes of individual polymer chains that trigger shear banding remains elusive and the proposed theories lack convincing experimental tests. Here, using a custom-built high-resolution rheo-confocal shear cell, we experimentally study the dynamics of DNA-bridged particle dumbbells in the shear-banding flow of entangled double-stranded DNA (dsDNA) solutions under large amplitude oscillatory shear (LAOS). In our experiments, we first synthesize dumbbells consisting of two spherical colloidal particles linked by λ-DNA and developed a code to track their 2D-projected configurations. Second, we confirm that the velocity profiles of the entangled dsDNA solutions are inhomo-geneous at high Wi and develop into strong shear-banding flows with two distinct shear-bands. We then

measure the orientational distribution of the DNA-bridged dimers and investigate their translational/rotational dynamics in highly entangled DNA solutions with two distinct shear bands. We find alignment along the flow direction, enhanced translation/rotation and a strong coupling between translation and chain extension exclusively in the high shear-rate band, which suggests shear-induced breakage of the local entanglement network in that region. Quantitative analyses of the spatially distinct dynamics of such dsDNA-bridged dumbbells in the two co-existing bands provide important insights into the microscopic origin of the shear-banding flows in entangled polymer solutions.

4.1 Introduction

Shear-banding, a heterogeneous shear profile with spontaneously separated domains of different shear rates, is a common feature observed in a variety of complex fluids undergoing strong shear flows [110]. Its emergence in entangled polymer solutions and melts was theoretically predicted long ago by the Doi-Edwards original tube model [2] and first experimentally reported about 20 years ago [25, 26]. Shear-banding has been studied extensively from both experimental and theoretical perspectives, and experimental evidence in support of existence of shear-banding in polymer solutions has accumulated over the past two decades in different polymer systems under different shear protocols including time-independent steady shear, and time-dependent start-up and oscillatory shear [32, 33, 42, 44, 45, 82].

In spite of these extensive efforts to rationalize the phenomenon, the microscopic origin of shear-banding in polymer solutions remains under debate and is far from fully understood [111]. Several scenarios have been proposed to account for this interesting non-linear flow feature within the current polymer theory frameworks consistently, for instance, strong coupling between flow and polymer concentration [3, 64–66],

localized disentanglement of networks [67, 112], instabilities triggered by stress overshoot [52, 53, 68], and long-penetrating edge disturbances [56, 57], all of which require more experimental validations to be considered a definitive explanation of the phenomenon.

Worm-like-micelles are probably the best-studied polymeric system exhibiting shear-banding. They can form long cylindrical filaments of aggregates entangled with each other to form transient entanglement networks, analogous to entangled polymer networks. It has been experimentally observed that the entangled filaments display strong alignment along a flow direction in the high-shear-rate band by flow birefringence, NMR, and SANS methods [113–116]. Such findings suggest that the conformational and/or configurational change of polymer chains can be a significant factor triggering the shear-banding flows.

Single molecule level visualization of polymers has been conducted extensively to provide direct evidence of chain dynamics. Such studies often adopt double-stranded DNA (dsDNA) thanks to its micron-scale size, semi-flexible nature, and ease of labeling with efficient bis-intercalating dyes such as YOYO-1 [117,118]. However, such attempts using dsDNA to investigate shear-banding are limited to dilute/semi-dilute regimes or relatively slower flow geometries because of imaging difficulties in fast flows of highly concentrated solutions, which unfortunately corresponds to the condition where the shear-banding can be realized. Asan alternative to dsDNA, direct observations of F-actin filaments undergoing non-linear flows [44, 104], which are also known to shear-band, have been performed. These filaments are different from typical flexible polymers, however, in that their persistence length is comparable to or even longer than the contour length.

We propose an alternative way to probe chain level dynamics in the shear-banding flow. We synthesize a dumbbell of fluorescent colloidal particles connected by linear

DNA linkers, expecting such bright particles will bypass imaging difficulties in the fast flow of highly concentrated DNA solutions, with the bridging linear chain linkers providing us with insights about chain extension as well as chain end distribution in the co-existing shear-bands. We use a custom planar-Couette confocal shear-cell to observe dynamics of such DNA-bridged dumbbells on a flow-vorticity plane. By investigating the orientation and dynamics of DNA-bridged dumbbells, we find that the orientational distribution and the degree of enhancement in translation/rotation are spatially distinct in different shear-bands. Coupling between translational and rotational dynamics, and between the chain extension and translational dynamics also show quantitatively differences in two shear-bands. More pronounced alignment along the flow direction, faster translation/rotation dynamics, and stronger coupling between translation/rotation and between chain-extension and translation are observed in the high-shear-rate band. Such spatially distinct DNA-bridged dumbbell dynamics provide valuable insights into the microscopic origin of shear-banding in polymeric solutions.

4.2 Materials and methods

4.2.1 Synthesis of DNA-bridged particle dumbbells

Synthesis of DNA linkers

Figure 4.1 describes our method of synthesizing DNA-bridged particle dumbbells. DNA linkers are prepared by ligating single-stranded sticky chain ends of a long linear DNA with complementary single strands that contain reactive groups (biotin or digoxygenin) at 3'-end. In our study, λ-DNA is used as a long linear DNA (New England Biolabs, 48.5 kbp). It is obtained by cleavaging a circular dsDNA of Escherichia virus Lambda with a restriction enzyme, leaving both chain ends single-stranded. These reactive sticky

ends are hybridized with excess amounts of 5'-GGGCGGCGACCT-3'-Biotin and 5'-AGGTCGCCGCCC-3'-Digoxygenin (DIG) oligomers (Integrated DNA Technologies). The hybridized DNA linker has nicks in its phosphate backbones, which are repaired by a standard ligation step. After ligation, the remaining unreacted short oligomers are removed by gel electrophoresis, and the ligated product is recovered from agarose gel by gel digestion, followed by purification using drop dialysis. The DNA concentration is determined by UV-Vis spectrometer (NanoDrop) and diluted with 1X TBE buffer (89 mM tris base, 89 mM boric acid, 2 mM EDTA) to achieve a final concentration of 10 μg/mL or 0.33 nM. The resulting DNA linker has biotin at one end and DIG at the other end.

Surface modification of colloidal particles

Two batches of carboxylated polystyrene colloidal particles are functionalized with either streptavidin or anti-digoxygenin (anti-DIG) respectively and further passivated by methoxypoly(ethylene) glycol amine (mPEG-NH_2, Mw = 5000, Alfa Aesar) by means of EDC/NHS coupling. The particle coating protocol is slightly modified from a previous literature [119]. Fluorescent, carboxylated magnetic polystyrene particles (d = 2.9 μm) are acquired from Bangs Laboratories. In each batch, 10 mg of particles are suspended in 400 μL of 50 mM MES buffer. 100 mM solutions of 1-ethyl-3-(3-dimethylaminopropyl) carbodiimide hydrochloride (EDC) and N-hydroxysulfosuccinimide sodium salt (Sulfo-NHS) in 50 mM MES buffer are prepared immediately before use, 50 μL of which is added to the particle solution sequentially while stirred on a vortex mixer. The suspension is left for 25 minutes for activation of the carboxylic groups. Then, the activated particles are washed and resuspended in 500 μL 1X PBS buffer (phosphate-buffered saline, 137 mM NaCl, 2.7 mM KCl, 10 mM Na_2HPO_4, 1.8 mM KH_2PO_4, with a pH of

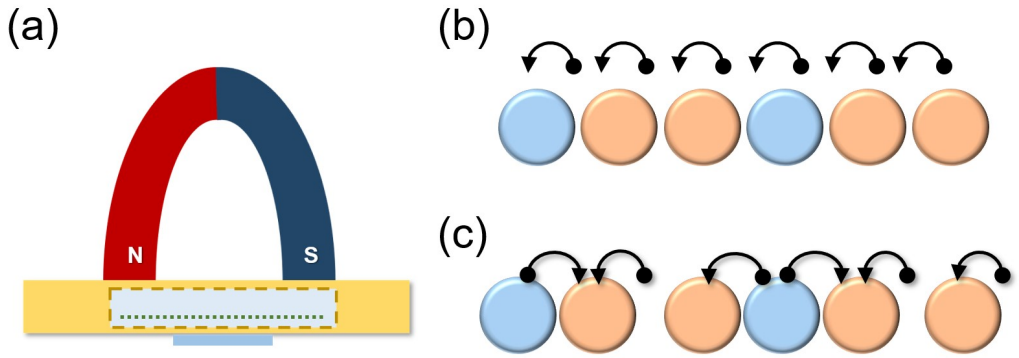

Figure 4.1: (a) A schematic of dimer synthesis reaction using the 3D-printed reactor and a magnet. A reactant solution of 200 μL (0.05 wt% anti-DIG coated particles, 0.05 wt% streptavidin-coated particles, 5 μg/mL protein tagged λ-DNA in TBE 1X buffer) is injected inside the well (20 mm X 5 mm X 6 mm) of the channel and a horseshoe magnet is placed on the channel to align particles. The center of the well has a small hole blocked by a glass cover-slip for microscopy. (b) Two types of particles are aligned into a string with a random sequence by a magnetic field. A λ-DNA linker (black) has heterogeneous chain ends. Conjugation between an anti-body (streptavidin or anti-DIG) on a particle and protein (biotin or DIG) tagged to each chain end is selective. (c) Neighboring particles are bridged by the λ-DNA linkers only when different types of particles are alternating in a line. After removing a magnet, a single particle, a dimer, and a trimer are synthesized in the example.

7.4), followed by addition of 100 μg of protein (streptavidin or anti-digoxygenin) dissolved in 200 μL 1X PBS buffer. After a reaction time of 4 hours, mPEG-NH_2 dissolved in 200 μL of water is added, and the reaction is allowed for longer than 40 hours. After reaction, 1% glycine is added for quenching, and the conjugated particle is washed and suspended in TBE 1X buffer.

Synthesis of dumbbells

Linking process depends on collisions between particles and is slow and inefficient. As a result, we have implemented a reactor that brings the particles into close contact to allow the DNA linkers to have more chances to bridge them. Our linking procedure is based on the procedure a previous literature [120]. Ref. [120] prepared a chamber made of two glass cover-slips spaced by a double-sided tape and sealed with epoxy glue. As we need to recover synthesized dumbbells after the reaction to using in our shear flow cell, however, we use the 3D-printed reactor shown in Fig. 4.1. The reactor is made of polyacrylonitrile and has a rectangular well inside with a dimension of 20 mm X 5 mm X 6 mm. There is a small glass window at the center of the well for microscopy. We make a 50:50 mixture of streptavidin-coated and anti-DIG coated particles and inject it into the well. The ligated DNA solution is then added into the well gently. The final volume of solution inside the well is 200 μL with a composition of 0.05 wt% streptavidin-coated particles, 0.05 wt% anti-DIG coated particles, and 5 μg/mL ligated DNA. The device is put inside a closed petri dish chamber with a solvent trap to reduce sample evaporation, and a horseshoe magnet is placed on top of the lid to align the particles into long strings with a magnetic field ($\approx$ 80 G). The magnet is removed and the sample solution is recovered after overnight reaction by gently aspirating with a wide-mouthed micro-pipette. During the reaction, the two types of particles are brought into long stable strings with random sequences due to the applied magnetic field (Fig. 4.1(b)).

Biotin/streptavidin and DIG/anti-DIG bindings are selective. As each DNA linker has heterogeneous ends, it cannot form a closed loop by connecting both ends to the same bead. Instead, once one end is bound, the other end should remain unbound freely or find and bind to another particle of the other kind. As the size of a particle is much larger than the radius of gyration of λ-DNA (0.58 μm [90]), it is unlikely for a linker to form a bridge between distant particles. Therefore, the linker forms a bridge only when the sequential neighbors in a line are alternating in particle types (Fig. 4.1(c)). If the same type of particles appear consecutively, they cannot be bridged by the linker and the propagation of a particle string will be terminated. Thus, the probability of n-mer formation follows $P(n) = (1/2)^n$, and also the probability of a particle to be a part of n-mer is $P(n) = n(1/2)^{(n+1)}$. Even though we cannot completely prevent longer multi-mers from being formed, its contribution can be kept low since its probability of appearance decays rapidly with its length. The majority of the particles remain either single or form a dimer. Once the DNA-bridged dumbbells are synthesized, they are suspended in 1X TBE buffer.

We conduct control experiments to verify our dumbbell synthesis as shown in Fig. 4.2. To confirm selective body/anti-body interactions and protection of particles from non-specific adsorptions, we add the YOYO-1 fluorescent label to the ligated λ-DNA and let it react with two different batches of particles. One batch of particles is treated with mPEG-NH_2 only (Fig. 4.2(a)), while the particles in the other batch have conjugated reactive sites (anti-DIG) on their surfaces in addition to mPEG-NH_2 passivation (Fig. 4.2(b)). First, mPEG-NH_2 makes the particles well dispersed and free of aggregation in both cases, which indicates that the particles in the synthesized dumbbells are truly bridged by the DNA linker. When there is no anti-DIG conjugated to the particle surface (Fig. 4.2(a)), the fluorescently-labeled λ-DNA molecules exhibit free diffusion without being adsorbed to the particles. On contrary, once anti-DIG is conjugated to

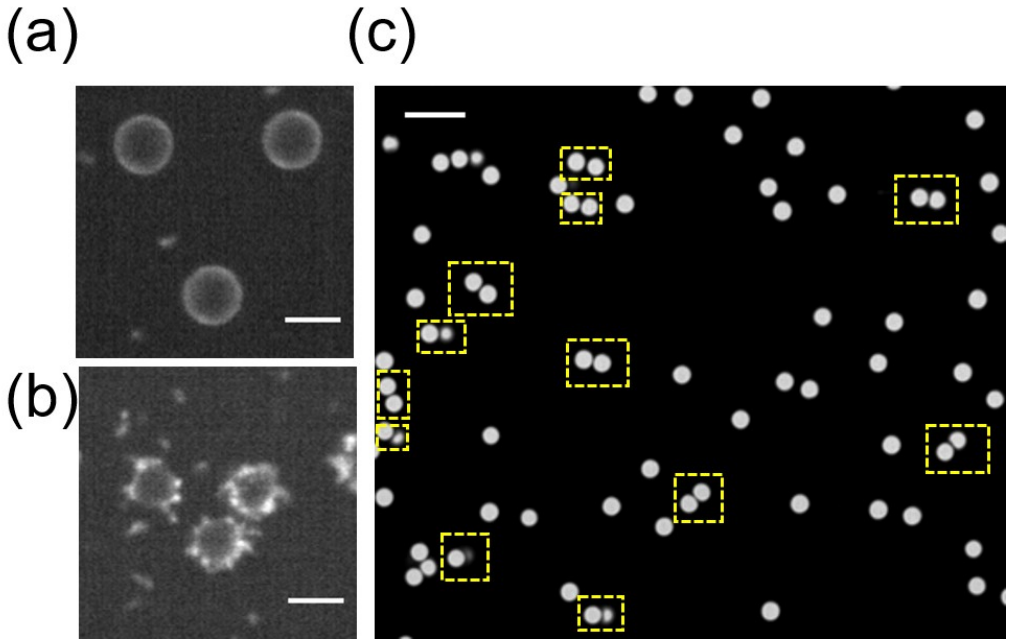

Figure 4.2: (a) A mixture of fluorescently labeled λ-DNA linker and mPEG-NH_2 coated polystyrene beads, after an overnight reaction. The particles are well dispersed and the DNA linkers are not bound to the particles. (b) Polystyrene beads coated with mPEG-NH_2 and anti-DIG, mixed with the same DNA linker. Image is taken after an overnight reaction. The DIG-tagged chain end is bound to the reactive site (anti-DIG) of the beads while the other, biotin-tagged chain end remains unbound and freely diffuses. (c) An image of the synthesized DNA-bridged dumbbells (yellow rectangle) after removing the aligning magnetic field. Half of the particles are anti-DIG coated and the other half have streptavidin on their surfaces. Scale bar = 5 μm in all images.

the particle surface (Fig. 4.2(b)), we observe that the DIG-tagged chain end of the fluorescent λ-DNA is bound to the particle surface while the other biotin-tagged end remains unbound. This control experiment proves that our synthesis scheme can successfully minimize non-specific bindings of DNA-particle as well as particle aggregations, allowing us to safely regard all the dumbbells are DNA-bridged. Fig. 4.2(c) shows an example image of products after the aligning magnetic field is removed. As expected, most of the particles are singlets or form dimers. The dumbbells seem to be tightly bound in the absence of external flows, which we attribute to the self-depletion of long DNA linkers. As our λ-DNA is long enough to have an appreciable size compared to a particle, the bridging DNAs tend to be entropically excluded from the inter-particle gap and induce an attractive potential energy well between the particles, which bring the particles into a closer contact with each other [120–123]. When the dumbbells are subject to shear-banding flows, we find some of the particles in a pair show separation longer than a particle diameter.

4.2.2 Sample preparation and characterization

Calf-thymus DNA (Sigma Aldrich, 10 - 15 kbp) is dissolved in the suspension as a background polymer at a fixed concentration of 11 mg/mL, which corresponds to 87 times its overlap concentration. The sample solution is left at least for a week with occasional gentle stirring to ensure its equilibration. A standard linear viscoelasticity test under small amplitude oscillatory shear is performed with the sample solution (AR-G2, TA Instruments) at 23 °C to extract parameters characterizing its rheological properties (Fig. 4.3). The disentanglement time, τ_d, is found to be 5.5 s from the reciprocal frequency where $G' = G''$. The average number of entanglement per chain, Z, is estimated as around 20 from its plateau modulus (G_N^0) which we determine from G' when it has the minimum phase angle (δ). The Rouse time, τ_R, is 0.09 s from

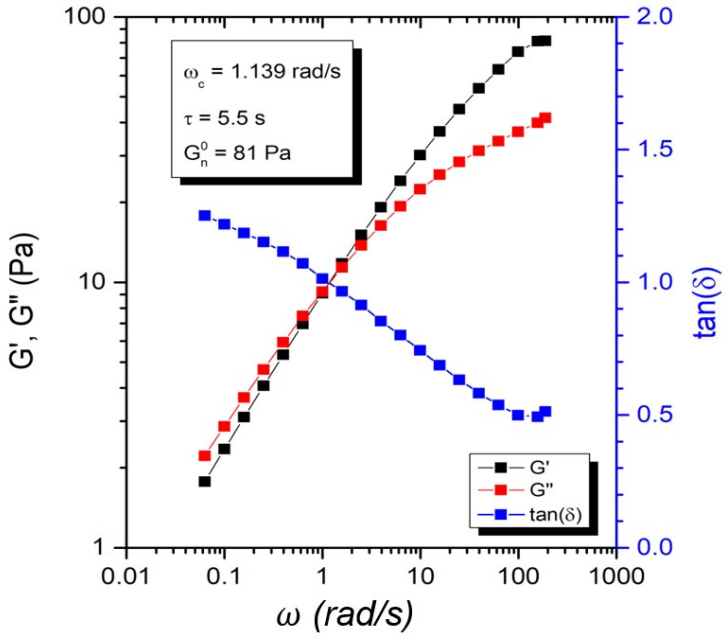

Figure 4.3: Linear viscoelasticity of a highly-entangled DNA solution. A calf-thymus DNA ($mathrmMw = 10 - 15$ kbp) is a background polymer with a concentration of 11 mg/mL. Its storage (G') and loss (G'') modulus are measured and plotted along with $\tan(\delta)$, where δ is a phase angle. The plateau modulus, G_N^0 is obtained from the G' value at minimum $\tan(\delta)$, when the ratio between viscous/elastic modulus is smallest. The measurement is performed at 23 °C.

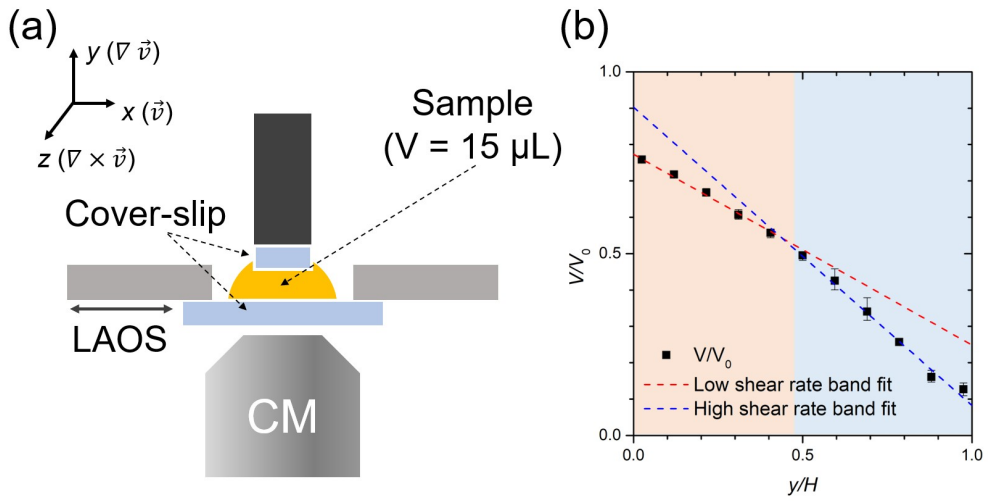

Figure 4.4: (a) A schematic of the custom-built planar-Couette shear cell (not to scale). (b) The measured shear profile at $\mathrm{Wi_{app}} = 55$ and $\mathrm{De} = 140$ based on reptation dynamics. The profile is fitted piece-wisely with two linear lines. The region of smaller shear gradient is low-shear-rate band and it is colored in red. The high-shear-rate band with a bigger slope is colored in blue.

$\tau_R = \tau_d/3Z$. The mesh size of the transient entanglement network is approximately 200 nm, twice its Kuhn length. R_g of the background calf thymus DNA is 0.25 μm based on R_g of λ-DNA [90].

4.2.3 Experimental setup

The sample solution is injected into our custom-built planar-Couette confocal shear cell (Fig. 4.4(a)). It has two square-cut glass coverslips (5 mm x 5 mm) aligned in parallel as shearing plates. While the top plate is fixed, the bottom boundary is driven sinusoidally by a piezo-electric actuator to exert LAOS flows with strain $\gamma(t) = \gamma_0 \sin(2\pi ft) = (A_0/H)\sin(2\pi ft)$, where A_0 is the amplitude of applied shear, H is a separation between the plates, and f is the shearing frequency. The detailed

information about our confocal shear-cell can be found in Refs. [93, 94, 109]. In our experiments, A_0 = 150 μm, H = 60 μm (= $240R_g$), and f = 4.0 Hz, which gives $\mathrm{Wi}_{\mathrm{app}} = \tau_d V_0/H = 2\pi f \tau_d \gamma_0 = 55$ and $\mathrm{De} = 2\pi f \tau_d = 140$ defined based on the reptation dynamics, τ_d. For Wi_{app} and De based on the Rouse dynamics, one can divide the dimensionless numbers by $3Z$. The shear-cell is placed on the inverted confocal miscroscope for visualization of the fluid flow via the transparent bottom glass window. As we previously reported an abnormally long penetration of edge disturbance in the shear-banding polymer flows [124]. Hence, we ensure that the region where we perform the measurements is at least 20 times H away from all the edges. At the fixed x and z position, we vary y to construct a velocity profile by Particle Image Velocimetry (PIV). Typically, image sequences are taken at 11 different heights and the whole y range is scanned three times for error estimation. It takes about 1 min. for all 33 videos required for a single shear profile. In addition to velocity profile measurements by PIV, we also analyze dynamics of the immersed dumbbells by Particle Tracking Velocimetry (PTV). First, we take strobed image sequences by synchronizing the imaging frequency to the shearing frequency (frame rate = 4.0 Hz). The resulting images are snapshots of the particle positions at a fixed phase in the LAOS cycle. Once trajectories of all the particles are generated, we run a dimer tracking code to determine and analyze the DNA-bridged particle dumbbells. The code selects dumbbells based on the assumption that there would be neither generation of new pairs nor breakage of the existing pairs into individual particles.

4.3 Results

A typical shear profile is shown in Fig. 4.4(b). Its velocities and heights are normalized by the applied velocity (V_0) and the gap (H), respectively. The data points can be well

fitted by piece-wise double linear functions. In our experiments, the low-shear-rate band appears near the moving bottom boundary and the high-shear-rate band is formed near the top stationary boundary. Strobed image sequences are taken at y/H = 0.05, 0.15, 0.25, 0.35, 0.55, 0.65, 0.75, 0.85. The first 4 heights are inside the low-shear-rate band, whereas the last 4 heights are inside the high-shear-rate band. Each snapshot in a video is taken once in a shear cycle when the applied shear strain is at its maximum and the corresponding shear rate reaches its minimum to reduce distortion of the images due to a finite exposure time.

Trajectories of all the particles are generated and they are indexed with identification numbers. A remaining drift quantified by $< \Delta x >_i$ and $< \Delta z >_i$ is subtracted, where i denotes every particle appearing in the successive frames. The dimer selection rule is then applied by using a custom Matlab dimer tracking code. The code keeps records of all the particles about whether they are in a dimer or singlets with their index numbers. In each frame, the code first scans all the neighbors around each particle within a cut-off searching radius. If the particle has more than two neighbors in a close distance, it is removed as a dimer candidate unless it has a record of pairing in the previous frames to avoid miscounting aggregates as dimers. Second, once potential particle pairs are chosen, the algorithm looks up their previous record to check if any particle in the pair formed a dimer with a particle other than the current partner. If so, those pairs are considered false and removed. Third, if the two particles in the potential pair appeared as singlets simultaneously in one of the previous frames, they are excluded since we do not allow for new formation of a dimer. Lastly, we only select the dimers which are tracked for more than 50 frames consecutively. And if the inter-particle distance exceeds a cut-off limit beyond which is considered unphysical, the whole record of such a pair is also discarded. After applying these strict dumbbell-selection rules, we acquire more than 800 trajectories of the dumbbells in each shear-band, and we analyze the

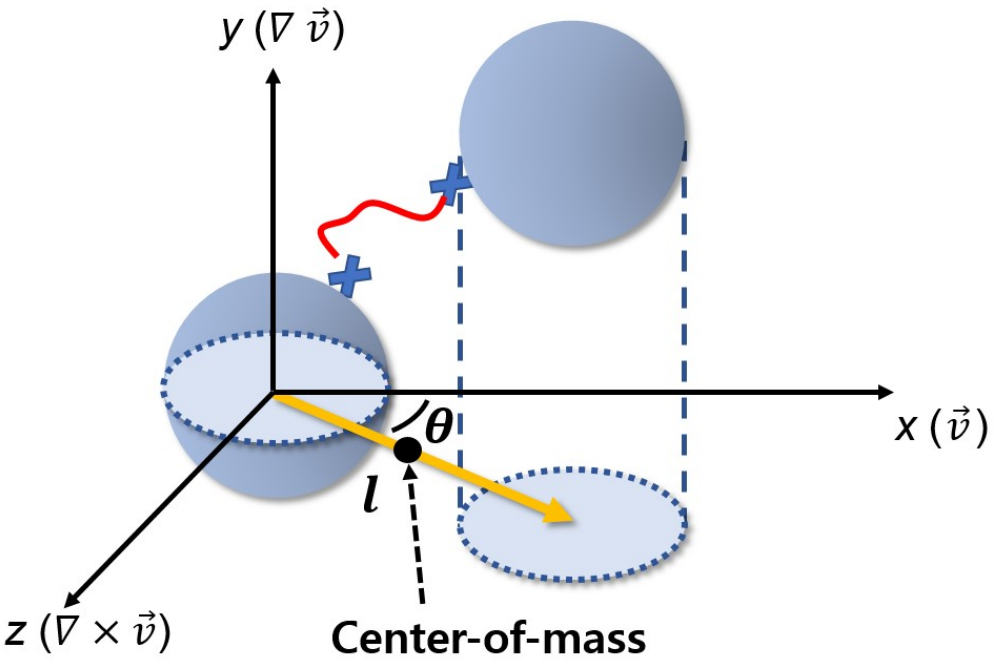

Figure 4.5: A schematic of a dimer linked by a linker (red) projected onto the imaging plane. We generate a vector (yellow) that connects the 2D-projected 6centers-of-mass of the two particles forming a DNA-bridged dumbbell. The dumbbell center of mass is determined from a mid-point to analyze its translational motion. Its rotation on xz plane is studied by tracking the azimuthal angle, θ, from the shear flow direction. The projected inter-particle distance, l, is also tracked.

translation of their centers-of-mass, orientations, and inter-particle distances. Since our confocal image is a 2D projection onto xz-plane, the center-of-mass, the inter-particle distance are the 2D-projection of the 3D configuration. The center-of-mass of a dumbbell is determined from a mid-point of the xz-projection of the vector connecting centers of the two particles, and the particle-particle distance is the length of the vector. Its orientation angle, θ, is an azimuthal angle with respect to the flow (x-) direction (Fig. 4.5). For ease of visualization and comparison of distinct features in the two co-existing shear-bands, the data acquired from the low-shear-rate band will be red-colored, while the data obtained from high shear-rate band will be presented in blue in the following sections.

4.3.1 Orientation of dumbbells in shear-banding solutions

We first present relative orientation of two particles forming a pair in the two shear-bands (Fig. 4.6). Taking one of the particles as the origin, the projected position of the other bead in the pair is displayed in the 2D heatmap. In the low shear-rate band (Fig. 4.6(a)), one can find bimodal peaks, one along x- (flow) direction and the other along z- (vorticity) direction. The bimodal peaks can be also captured in the azimuthal probability distribution function (PDF) of the dumbbell orientation in the low shear-rate band (Fig. 4.6(b)). Alignment of an anisotropic slender body along vorticity(z-) direction in a sheared viscoelastic fluid, so called log-rolling, was first theoretically studied by Leal [125] The log-roll alginment was attributed to the normal stress differences that drive the slender bodies to drift toward vorticity direction through near-Jeffery orbits. At even higher shear rates, or equivalently at higher elasticities, reorientation of the log-rolling slender body toward the flow direction was predicted and also has been observed experimentally, with bimodal distributions similar to Fig. 4.6(b) at intermediate regimes [126]. Normal stress differences drive dumbbells toward the z-direction while

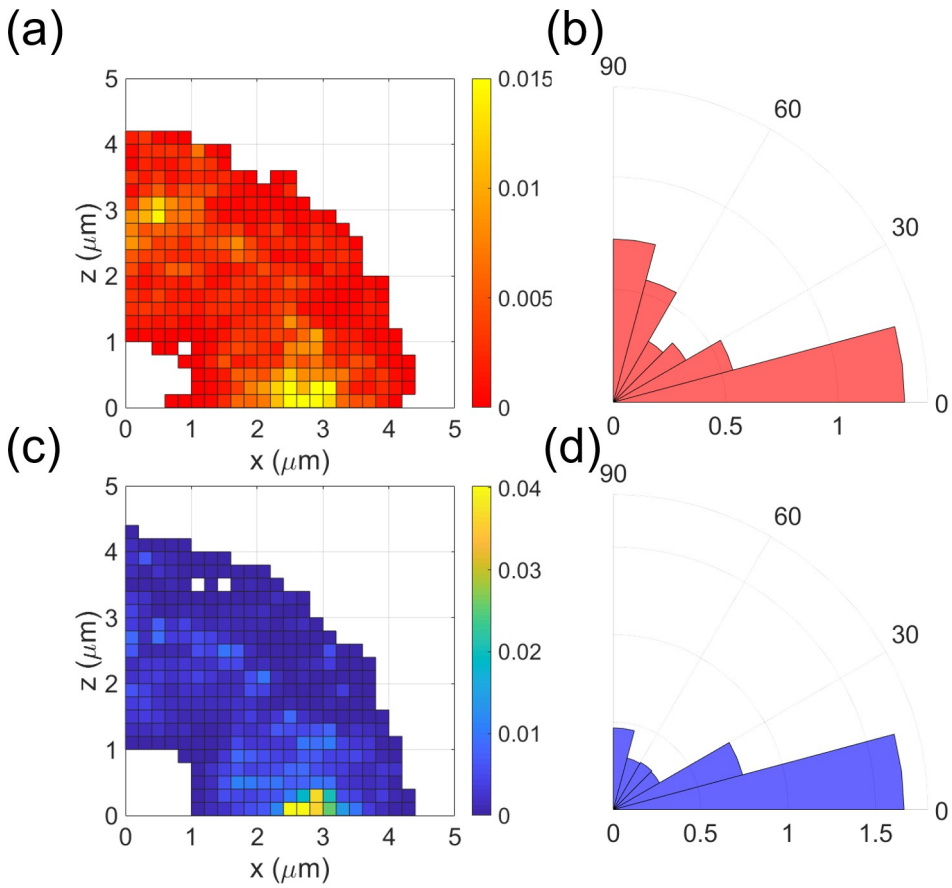

Figure 4.6: (a) Density map of projected orientation of dumbbells in the low-shear-rate band. The bimodal peaks along x-direction and along z-direction are highlighted with a dashed circle. (b) Normalized azimuthal PDF of θ calculated from (a) exhibits bimodal peaks. (c) Density map of projected orientation of dumbbells in the high-shear-rate band. The single peak along the x-direction is highlighted with a dashed circle. (d) Normalized azimuthal PDF of θ calculated from (c). The peak along the z-direction is almost negligible and only a single peak along the x-direction is pronounced.

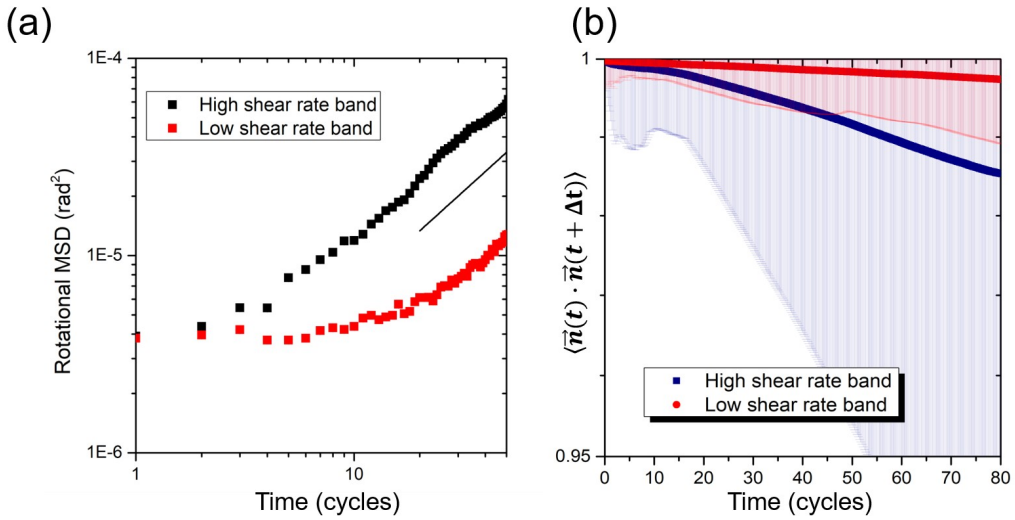

Figure 4.7: (a) Rotational mean-squared-displacement of dimers in the two shear-bands. Diffusive scaling is indicated with a black line for comparison. (b) Auto-correlation of an azimuthal angle (θ) of dimers as a function of time. Dimers in the high-shear-rate band decays faster, and the resulting effective rotational diffusivity quantified by an exponential fit of the diffusive regime is 7.7 times higher than that in the low-shear-rate band.

elasticity preferably aligns them along x-direction. In the high-shear-rate band, the higher shear-rate/stronger elasticity forces the dumbbells to become more flow-aligned while suppressing their log-rolling alignment (Fig. 4.6(c) and (d)). Therefore, different orientational distribution indicates the competition between elastic stress and normal stress difference in the two co-existing bands.

4.3.2 Dynamics of dumbbells in shear-banding solutions

To investigate spatial differences existing in the two bands, the dynamics of the DNA-bridged dumbbells are compared. Their rotational dynamics are analyzed and shown in Fig. 4.7. Note that the analyzed rotation is in terms of azimuthal angle θ relative

to the x-direction and lacks information about the polar angle. The rotational MSDs display transition from sub-diffusive to diffusive rotational dynamics in both low- and high-shear-rate bands expected for a shear-thinning fluid (Fig. 4.7(a)). Fig. 4.7(b) shows the time evolution of the autocorrelation of a dumbbell orientation. The dumbbells in the high shear-rate band show a slower decay in orientational correlation. The autocorrelation function is related to an effective rotational diffusivity (D^r_{eff}) via

$$< \vec{n}(t) \cdot \vec{n}(t + \Delta t) >= \exp(-2D^r_{\text{eff}}\Delta t), \tag{4.1}$$

where $\vec{n}(t)$ is a unit directional vector at t. D^r_{eff} is quantified by an exponential fitting of the autocorrelation function in the diffusive regime and D^r_{eff} in the high shear-rate band is greater than D^r_{eff} measured in the low shear-rate band by a factor of 7.7. Another interesting feature of Fig. 4.7(b) is that the variation in the high shear-rate band is much bigger, suggesting that some dumbbells actually experience more rapid orientation than others, leading to a higher degree of heterogeneity. In our previous study analyzing the dynamics of spherical particles immersed in shear-banding solutions [127], we observed more enhanced translational displacement in the high shear-rate band.

To further explore the translation/rotation of the dumbbell dynamics, we select the time interval of 10 cycles and plot the PDF of angular/translational displacements during the period (Fig. 4.8(a)). Both the PDFs drawn in the high and low shear-rate bands are normalized for a direct comparison. In both translational and angular displacements, the dumbbells in the high shear-rate band show more slowly decaying long non-Gaussian tails (Fig. 4.8(b) and (c)). It means that the dumbbells in the high shear-rate band can experience extraordinarily rapid translation and rotation much more frequently than those in the low shear-rate band. This result is again consistent with our previous study, where the immersed particles in the high shear-rate band displayed

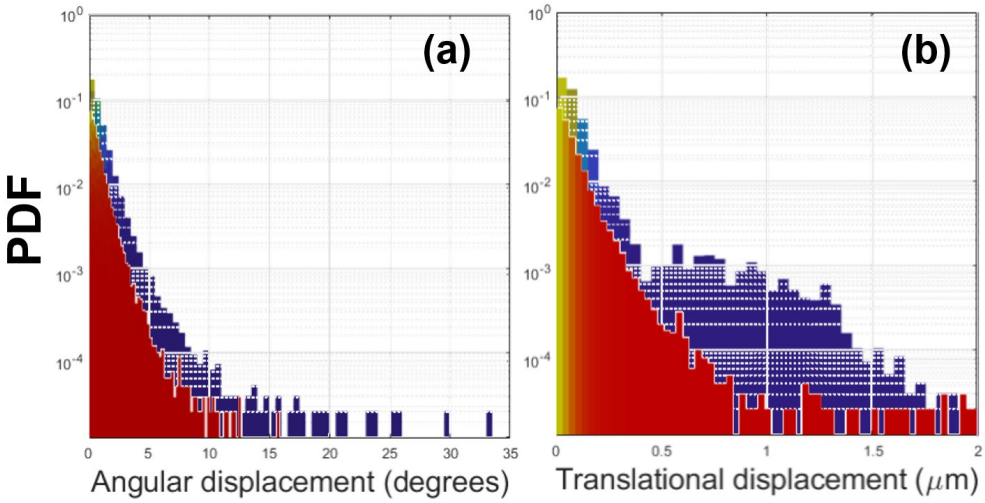

Figure 4.8: PDF of angular and translational dynamics of the dumbbells for a time interval of 10 cycles, in the two shear bands. (a) Angular displacement over 10 cycles in high (blue) and low (red) shear-rate band. (b) Translational displacement over 10 cycles in high (blue) and low (red) shear-rate band.

a Lévy-walk-type of transient super-diffusive translational motion [127].

4.3.3 Correlation of dumbbell dynamics in shear-banding solutions

Another interesting feature arises when both translational and rotational PDFs are viewed simultaneously(Fig. 4.9). In the low shear-rate band, translation and rotation appear to be independent or uncorrelated from each other. Fast translating dumbbells do not necessarily rotate rapidly in the low shear-rate band. The dumbbells experiencing both rapid translation and rotation over the given time interval are encountered more frequently in the high shear-rate band. This observation leads us to quantify the cross-correlation between translation and rotation to reveal their relation, using:

$$C_{|\Delta r|,|\Delta\theta|}(t) = \frac{< (|\Delta r| - < |\Delta r| >)(|\Delta\theta| - < |\Delta\theta| >) >}{\sigma_{|\Delta r|}\sigma_{|\Delta\theta|}}, \tag{4.2}$$

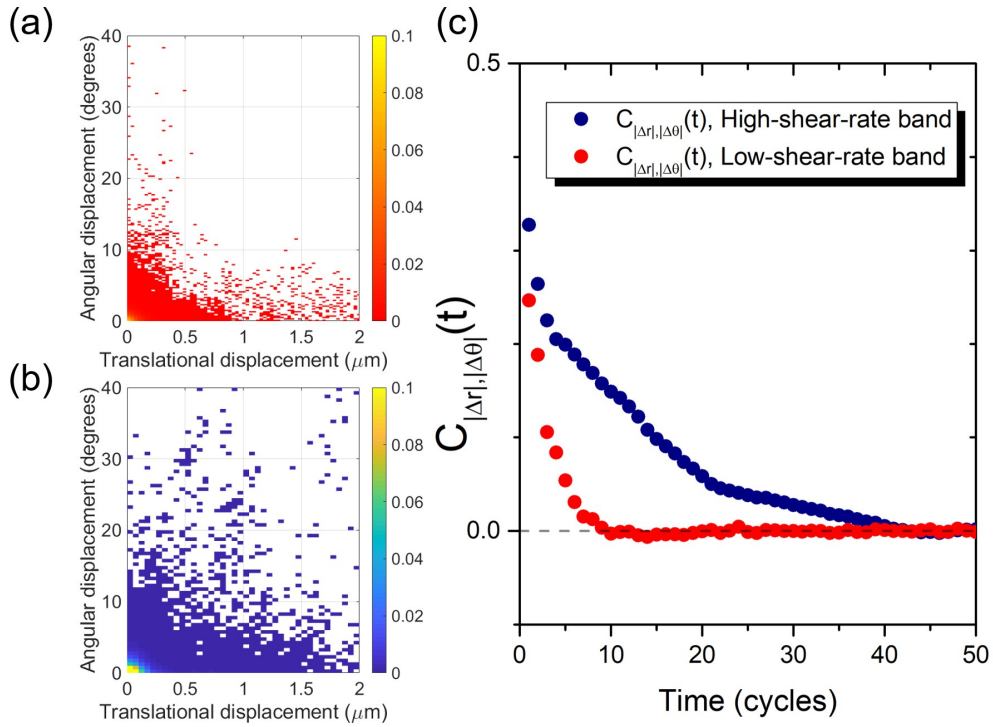

Figure 4.9: (a) PDF density map in the low shear-rate band. Fast translation and rapid rotation are not correlated. (b) The same PDF density map in the high shear-rate band. Fast translation and rapid rotation appear to be more correlated as one can observe more points in the upper-right region of the density map. (c) Correlation between translational ($|\Delta r(t)|$) and rotational ($|\Delta\theta(t)|$) displacements as a function of time interval. Coupling is stronger and decays slower in the high shear-rate band.

where $|\Delta r|$ and $|\Delta\theta|$ are the magnitude of translational and rotational displacements over the given time interval t, and $\sigma_{|\Delta r|}$ and $\sigma_{|\Delta\theta|}$ are standard deviations. Fig. 4.9(c) shows the correlation between translation and rotation in the low and high shear-rate bands. $C_{|\Delta r|,|\Delta\theta|}(t)$ is strongly correlated over longer a time period in the high shear-rate band, while correlates weaker and decays faster in the low shear-rate band.

4.3.4 Inter-particle separation of dumbbells in shear-banding solutions

As the paired particles are bridged by linear DNA linkers, the inter-particle distance projected onto the xz-plane (l) allows us to extract the information on the extent of chain extension. We focus on the cross-correlation between the inter-particle separation of a dumbbell (l, Fig. 4.5) and its translational displacement over t ($|\Delta r(t)|$). $C_{|\Delta r|,l}(t)$ quantifies how the dumbbells in the region of strong stretching translate over time:

$$C_{|\Delta r|,l}(t) = \frac{< (|\Delta r| - < |\Delta r| >)(l - < l >)}{\sigma_{|\Delta r|}\sigma_l}, \tag{4.3}$$

where $\sigma_{|\Delta r|}$ and σ_l are standard deviations. The result is plotted in Fig. 4.10.

Interestingly, the inter-particle separation and translational displacement of a dumbbell are negatively correlated (Fig. 4.10(a)). It is counter-intuitive in that stronger extension and alignment of polymer chains which result in longer l of the dumbbells are expected to reduce the effective viscosity.

This unexpected relation can be understood by considering directional dependence of effective diffusivity. For simplicity, we consider the Brownian motion of a dumbbell subjected to a simple shear flow ($V_x = \dot{\gamma} y$) with time-independent shear rate $\dot{\gamma}$, the initial position of which is $(x(0), y(0)) = (0, 0)$. Its motion obeys the Langevin equation:

$$R_x(t) = \zeta_x[\dot{x}(t) - \dot{\gamma} y(t)] \tag{4.4}$$

$$R_y(t) = \zeta_y \dot{y}(t), \tag{4.5}$$

where ζ_α is a drag coefficient in α-direction. R_α is a Gaussian-distributed random force in the α-direction that balances Stokes drag due to the Brownian motion of an object

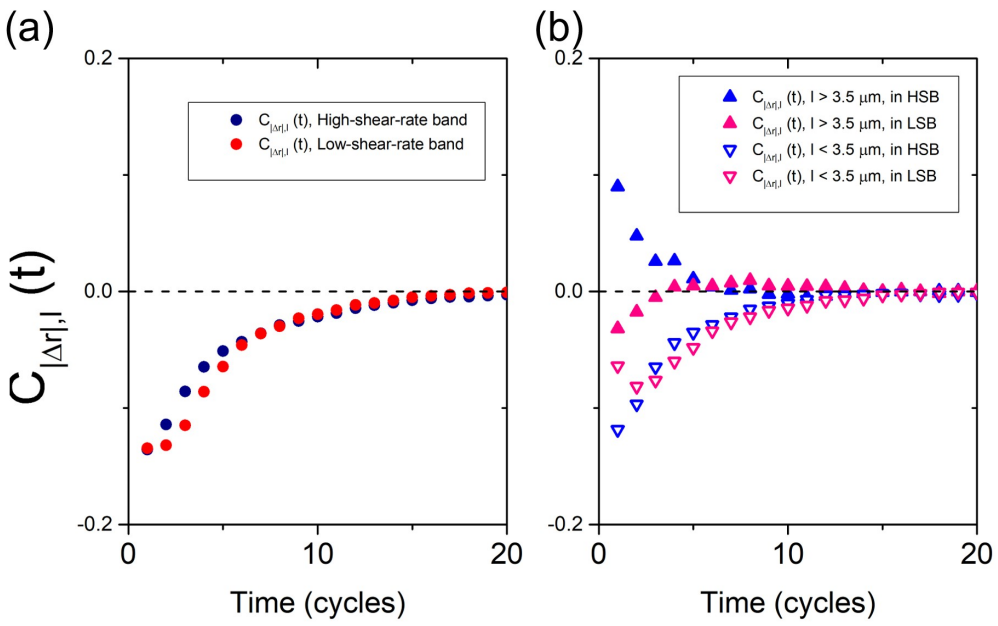

Figure 4.10: (a) Correlation between the inter-particle separation (l) of dumbbells and their in-plane translational displacement ($|\Delta r(t)|$) in the high (blue) and the low (red) shear-rate band. (b) Dumbbells are categorized according to whether $l > 3.5$ μm or not and whether the measurement is made in the high or low shear-rate band. The data with $l > 3.5$ μm are described with filled symbols whereas $l < 3.5$ μm data are drawn with hollow symbols. Upper triangular symbol means they are measured in the high shear-rate band while lower triangle symbols are used for the dumbbells in the low shear-rate band. Correlation function between l and $|\Delta r(t)|$ is calculated again in the four groups of the dumbbells. Only the dumbbells which are stretched ($l > 3.5$ μm) and in the high shear-rate band exhibit a positive correlation between the linker extension and translation.

and satisfies the following equations:

$$< R_\alpha(t) >= 0 \tag{4.6}$$

$$< R_\alpha(t) R_\beta(t') >= 2\zeta k_B T \delta_{\alpha\beta} \delta(t - t'), \tag{4.7}$$

where $\delta_{\alpha\beta}$ is the Kronecker delta and $\delta(t - t')$ is the Dirac delta function.

$$< R_\alpha(t) R_\alpha(t') >= 2\zeta_\alpha k_B T \delta(t - t'), \tag{4.8}$$

and ζ_α is related to the effective diffusivity in the α-direction through the Einstein relation, $\zeta_\alpha = k_B T / D_\alpha$.

$$\Delta x(t) = \int_0^t \dot{x}(\tau) d\tau = \frac{1}{\zeta_x} \int_0^t R_x(\tau) d\tau + \int_0^t \dot{\gamma} y(\tau) d\tau \tag{4.9}$$

$$\Delta y(t) = \int_0^t \dot{y}(\tau) d\tau = \frac{1}{\zeta_y} \int_0^t R_y(\tau) d\tau \tag{4.10}$$

For the MSD in the y-direction,

$$< \Delta y(t)^2 >= \frac{1}{\zeta_y^2} \int_0^t \int_0^t < R_y(\tau_1) R_y(\tau_2) > d\tau_1 d\tau_2 = \frac{2 k_B T}{\zeta_y} t = 2 D_y t, \tag{4.11}$$

which is expected as there is no convective flow in the y-direction. On the contrary, the x-directional MSD has an additional term due to coupling between diffusion and convection:

$$< \Delta x(t)^2 >= 2 D_x t + \dot{\gamma}^2 \int_0^t \int_0^t < y(\tau_1) y(\tau_2) > d\tau_1 d\tau_2 \tag{4.12}$$

The first term is molecular diffusion and the second term arises as the dumbbell that diffuses in the y-direction is convected by the x-directional shear flow, which leads to

enhanced fluctuations in the x-directional translation. The second term can be further simplified:

$$\begin{aligned}
\dot{\gamma}^2 \int_0^t d\tau_1 \int_0^t d\tau_2 < y(\tau_1)y(\tau_2) > &= \frac{\dot{\gamma}^2}{\zeta_y^2} \int_0^t d\tau_1 \int_0^t d\tau_2 \int_0^{\tau_1} d\tau_3 \int_0^{\tau_2} d\tau_4 < R_y(\tau_3)R_y(\tau_4) > \\
&= \frac{2k_BT\dot{\gamma}^2}{\zeta_y} \int_0^t d\tau_1 \int_0^t d\tau_2 \int_0^{\tau_1} d\tau_3 \int_0^{\tau_2} d\tau_4 \delta(\tau_3 - \tau_4) \\
&= 2D_y\dot{\gamma}^2 \int_0^t d\tau_1 \int_0^t d\tau_2 \int_0^{\tau_1} d\tau_3 \int_0^{\tau_2} d\tau_4 \delta(\tau_3 - \tau_4) \\
&= 2D_y\dot{\gamma}^2 \int_0^t d\tau_3 \int_0^t d\tau_4 (t - \tau_3)(t - \tau_4)\delta(\tau_3 - \tau_4) \\
&= \frac{2}{3} D_y(\dot{\gamma}t)^2 t = \frac{2}{3} D_y \gamma^2 t
\end{aligned} \tag{4.13}$$

Therefore,

$$< \Delta x(t)^2 >= 2D_x t + \frac{2}{3} D_y \gamma^2 t \tag{4.14}$$

Eq. (4.14) is same as the previous results [96, 128, 129] except that the isotropic diffusivity, D, is replaced by direction-dependent diffusion coefficients. On the one hand, since our peak-to-peak shear strain $\gamma = 2A_0/H = 5$ is much smaller than the strain required for a full cycle of Jefferey orbits, the orientation of the dimer is not instantly uncorrelated during shear cycles. On the other hand, our peak-to-peak strain of $\gamma = 5$ is large enough to make the second term in Eq. (4.14)) dominant because of its γ^2 dependence, so the in-plane translation is much more strongly affected by D_y than by D_x. A dumbbell aligned along the xz-plane that has a longer xz-projected inter-particle separation experience stronger drag along the y-direction due to its larger cross-sectional area, thereby has lower D_y [130]. As a result, the dumbbell shows slower in-plane translation compared to the dumbbells aligned along the gradient direction. It can contribute to the negative correlation between the particle-particle distance projected

on the xz-plane (l) and in-plane translation ($|\Delta r(t)|$), so it could have masked the true coupling between the DNA linker extension and translation. We find a qualitatively similar trend even from non-extensible dumbbells that are connected by very short DNA linkers in the same shear-banding polymer solution and in a sheared density-matched Newtonian glycerol/water mixture (85/15 vol%) (Fig. 4.11). The control experiments with the non-extensible dumbbells show the negative correlation between $|\Delta r|$ and l in all the cases (Fig. 4.11(a)), which further supports our argument. Additionally, since the 3D inter-particle separation is fixed at a particle diameter, the short non-extensible dumbbells allow us to investigate the orientation of the dumbbells with respect to the shear-vorticity (xz-) plane as shown in Fig. 4.11(b). The non-extensible dumbbells are more aligned along the xz-plane in the high shear-rate band than in the low shear-rate band, as expected.

In order to reduce the masking effect, we separate the dumbbells according to whether l is longer or shorter than a cut-off length of $d_{cut} = 3.5$ μm and whether they are in the high or low shear-rate band and recalculate their cross-correlation functions in four different cases. Since d_{cut} is longer than a particle diameter (2.9 μm), it guarantees the DNA linkers connecting the beads in the selected dumbbell with $l > d_{cut}$ are being stretched and they are preferentially aligned along the xz-plane so that the dimers have similar D_y to reduce the masking effect explained above. As shown in Fig. 4.10(b), only the dumbbells with $l > d_{cut}$ in the high shear-rate-band display a positive cross-correlation between l and $|\Delta r(t)|$ out of the four cases. It suggests the polymer chain extension and lower effective viscosity are correlated in the high shear-rate band. On contrary, the coupling between the chain stretching and lower effective viscosity is not found, or at least not strong enough to overcome the masking effect, in the low shear-rate band even from the stretched dumbbells.

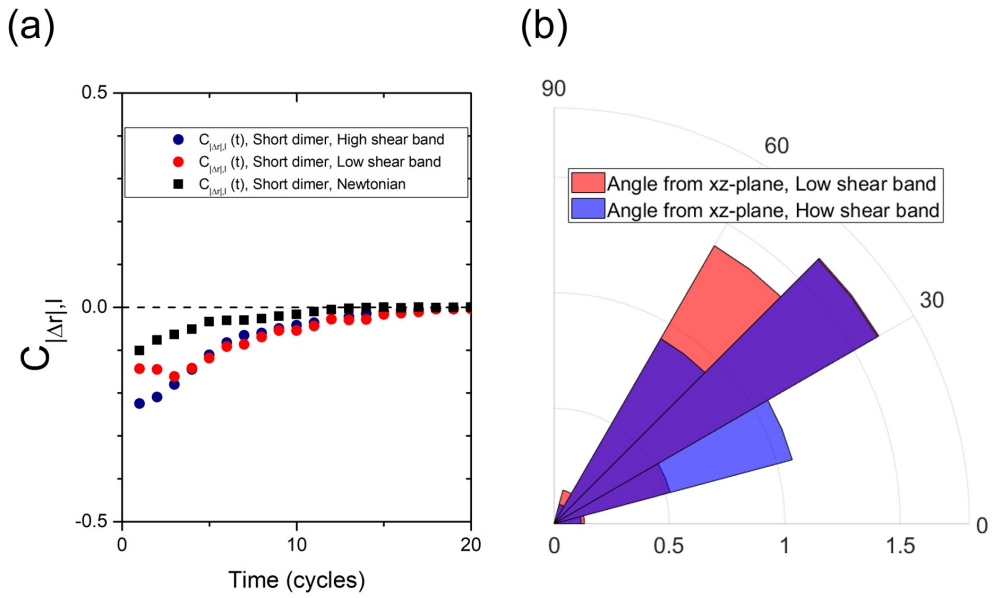

Figure 4.11: (a) Correlation between the inter-particle separation (l) of short, non-extensible dumbbells and their in-plane translational displacement ($|\Delta r(t)|$) in the high (blue) and the low (red) shear-rate band of polymer solutions and in a density-matched Newtonian solvent (black). Every case displays a negative correlation between l and $|\Delta r(t)|$. (b) Normalized PDFs of the short, non-extensible dumbbell with respect to xz-plane in the two shear bands. As the 3D inter-particle separation is fixed at a particle diameter, the ratio between l and d gives $\cos\phi$, where ϕ is the angle from the xz-plane. The dumbbells are more aligned along the xz-plane in the high shear-rate band (blue) than in the low shear-rate band (red).

4.4 Discussion

We found the different projected orientational distributions of the dumbbells in the two bands. We also observed the enhanced translational and rotational dynamics in the high shear-rate band which reflect its lower effective viscosity. Our correlation study reveals that such enhanced translational and rotational dynamics are coupled in the high shear-rate band. Another trend to note is that coupling remains weak with most of the dumbbells in the high shear-rate band whereas a portion of them experience strongly coupled fast translation and rapid rotation. Moreover, the extension of the DNA linkers that connect the particles in a dumbbell is correlated with the translational dynamics of the dumbbell in the high shear-rate band. These unique dynamic features and correlations are either much weaker or not found in the low shear-rate band.

Our results may suggest structural differences between the two shear bands. It is worth revisiting the proposed mechanisms of shear-banding such as edge disturbances [56,57], localized shear-induced disentanglement [70,131], and flow-concentration coupling [3, 64, 66]. The aspect ratio of our device is large enough ($A/H = 100$) to disregard edge disturbances as a cause of the observed shear-banding [124]. The enhanced dynamics in the high shear-rate band indicates the lower effective viscosity, which is consistent with both explanations based on the localized disentanglement and the lower concentration in the high shear-rate band predicted by two fluid Rolie-Poly models [3,58,64,66] because both effects reduce the effective viscosity in the high-shear rate band. On the other hand, a larger variation is found in the dumbbell dynamics in the high shear-rate band and only a fraction of them exhibit such strong couplings, which is also consistent with our previous study [127] where we found a strong dynamic heterogeneity in the translational dynamics of the spherical tracers embedded in the

high shear-rate band. This findings lead us to hypothesize that the unique dynamic features of the immersed DNA-bridged dumbbells that we witness in the high shear-rate band could be localized.

4.5 Summary

In conclusion, we synthesized the dumbbells made of colloidal particles connected by λ-DNA linkers and studied their dynamics in shear-banding polymer solutions. Our concentrated DNA solution develops a shear-banding velocity profile under strong shear with $\mathrm{Wi}_{\mathrm{app}} > 1$. In the low shear-rate band, the orientation of dumbbells show bimodal distribution along the x- and the z-directions due to interplay between the normal stress difference and elasticity whereas the dumbbells are aligned along the x-direction by the dominant elastic stress over normal stress differences. Both translational and rotational dynamics are more enhanced in the high shear-rate band, which implies formation of low effective viscosity zone. Moreover, the translational and rotational displacements are correlated more strongly in the high shear-rate band. Positive correlation between the extension of the linking DNA chain and the translational displacement is also found exclusively in the high shear-rate band.

Chapter 5

Concluding remarks

5.1 Summary and conclusions

As reviewed in Chapter 1, the shear-banding in polymer solutions and melts is a long-standing problem. It has been reported in a few polymer systems [25–35,40–46,124,127] such as PBD, PAAm, DNA, xanthan, F-action solutions. Theoretical efforts to incorporate the experimentally observed shear-banding in polymer solutions have developed phenomenological models [3,21,51–58,63–66] which can predict the criteria for the shear-banding. A number of mechanisms leading to the shear-banding have been proposed, all of which need experimental tests to be verified.

While many previous experimental studies depended on velocimetry measurements, much fewer works were dedicated to the polymeric microstructure [111]. In the present study, we tried to use a carefully designed shear flow cell to avoid misleading experimental artifacts and elucidate the microscopic origins related to the shear-banding. In specific, we adopted a large aspect ratio, planar-Couette geometry as curved streamlines [47] and edge fractures [56] are possible causes of flow instabilities. LAOS flow was applied because it is a shear protocol which can test both steady and time-independent

shear-banding [54]. And the device was coupled with a confocal microscopy as it can provide us with information about the microstructures with high spatial resolution.

In Chapter 2, we studied the response of concentrated DNA solutions under LAOS using the confocal shear cell. We could explore the flow transition from linear to wall-slip dominant behavior and finally to shear-banding velocity profiles with increasing $\mathrm{Wi}_{\mathrm{app}}$. By varying the gap thickness (H) and the shear rate, we constructed phase diagrams that quantify the degrees of wall-slip and shear-banding in the parameter space of $\mathrm{Wi}_{\mathrm{app}}$ and b_{avg}/H in a similar manner to Ref. [24]. We confirmed that a significant wall-slip always precedes shear-banding flows and they show opposite trends. At a fixed strain $\gamma_0 = 1.5$, the wall-slip is favored with a thinner gap and a lower $\mathrm{Wi}_{\mathrm{app}}$ whereas the shear-banding flow develops with a thicker gap and a higher $\mathrm{Wi}_{\mathrm{app}}$. Moreover, we found that embedded tracer particles in shear-banding polymeric fluids display qualitatively different dynamics in the two co-existing shear bands. While particles in the low shear-rate bend show normal in-plane diffusion, particles in the high shear-rate band exhibited transient super-diffusivity expressed by a sudden abnormal "jump", the probability distribution of which obeys the distribution of Lévy walks. A high degree of dynamic heterogeneity was also observed exclusively in the high shear-rate band. These results are reminiscent of tracer dynamics in sheared colloidal glasses [132] where the stress built-up due to deformation faster than the relaxation rate pushes particles ballistically when the local caging structure is destructed.

We further quantitatively analyzed the associated length and time scales of abnormal particle dynamics. In contrast to the low shear-rate band, where correlations are negligible, the tracer dynamics in the high shear-rate band are strongly correlated both temporally and spatially. We hypothesized that these dynamic features are associated with shear-induced chain disentanglement and breakage of local entanglement network in the high shear-rate band. In such a scenario, the characteristic time scale of 11.2 ± 1.7

cycles could be a measure of the life-time of the locally broken networks. The spatial correlation study gave two characteristic length scales. The short-range correlation gives a length scale of $l_s = 0.81 \pm 0.23$ μm or 10 mesh sizes and the scale of the longer range correlation ($l_l = 30.2 \pm 2.6$ μm) was comparable to the width of the high shear-rate band.

In Chapter 3, we directly evaluated the effect of edge-induced disturbances on the bulk velocity profile. Edge-induced instability is one of the crucial limiting factors in the experimental rheology of complex fluids. Criticism on earlier experimental observations of shear-banding was focused on the possibility of edge fractures [36, 38, 39] and simulations predicted that even a mild edge disturbance, which is hardly noticeable in experiments, can induce apparent shear-banding that persists deep inside a sheared sample and might have misled researchers [56, 57]. Therefore, it is important to verify whether the shear-banding we observed in Chapter 2 is a genuine fluid flow property or due to experimental artifacts. We tested three different flow cases. First, in a Newtonian solution, the edge effect decays within a distance H from the edge and the linear velocity profile is observed. Thus, the solution exhibit a short penetration depth comparable to the H of the shear cell, consistent with our understanding based on Newtonian fluids. In the second case, we applied LAOS flow to the DNA solution such that a linear profile accompanying significant wall-slip appears according to the phase diagram we mapped in Chapter 2. The penetration depth was again on the order of H. Under strong shear with shear-banding flows, however, the penetration depth was one order of magnitude larger than the gap thickness ($\delta = 20\ H$) along the flow direction, confirming the existence of an abnormally long penetration of edge disturbance [56]. Moreover, we found that the penetration depth is anisotropic. The influence of edge disturbance is significantly deeper along the flow direction than along the vorticity direction. A larger fluid reservoir results in a slightly shorter penetration depth ($\delta = 15\ H$), a feature that

may be exploited in standard rheological tests of entangled polymeric fluids. Finally, we verified that LAOS exerted in our experiments gives rise to true bulk shear-banding flows without the influence of edge disturbance.

Our work has multiple implications for the experimental rheology of the shear-banding flow. Experimentalists should note that the device aspect ratio may need to be much higher than anticipated to safely prevent the measured velocity profiles from being affected by the edge instabilities, especially when a planar-Couette flow geometry is used. On the contrary, in many conventional rheometers, the edge disturbance penetrates along the z-direction. Since we observed the penetration depth along the z-direction is still on the order of H, the previous observations of shear-banding exploiting rotational flow geometries can still remain valid, even though additional instability arising from the curved streamlines need to be evaluated separately. Lastly, a larger fluid reservoir indeed reduced the penetration of the edge instabilities. Hemingway and Fielding [55] suggested that immersing the flow cell in a bathing fluid can be effective in eliminating the development of edge fractures as it will reduce the stress jump across fluid-air interface and increase the surface tension. Our result is in line with their argument in that the presence of the drown edge can suppress the edge-induced disturbances. Therefore, the shear-banding experiments, which do not require making a stress measurement that is also affected by the bathing fluid, could be better performed in the immersed flow geometry.

We need a better understanding of chain-level microscopic information associated with the shear-banding. Molecular dynamics simulations provided us with valuable insights about a possible mechanism of the shear-band formation in polymer melts from the flow-induced disentanglement and the insufficient orientational relaxation [71]. However, the experimental verification whether the suggested mechanism is true or not is difficult since single molecular visualization of flexible polymer chains is limited in fast

flows of highly concentrated solutions where the shear-banding flows occur. In Chapter 4, we synthesized the dumbbells made of fluorescent colloidal particles connected by λ-DNA linkers as an alternative to studying individual polymer chains. We then studied their dynamics in shear-banding polymer solutions to acquire insights about the chain end distribution and the chain dynamics.

In the low shear-rate band, the orientation of dumbbells showed a bimodal distribution along the x- and the z-directions due to competition between the normal stress difference and elasticity, whereas the dumbbells are aligned along the x-direction by the dominant elastic stress. Both translational and rotational dynamics are enhanced in the high shear-rate band, which indicates formation of a low effective viscosity zone. Moreover, the translational and rotational dynamics are correlated more strongly in the high shear-rate band. The correlation between the projected inter-particle separation and the translational displacement of a dumbbell was negative, which we attributed to a short-term Taylor dispersion arising from the directional dependence of the dumbbell diffusivitiy. By focusing on the dumbbells linked by the stretched DNA linkers in the high shear-rate band, we recovered a positive correlation between the chain-extension and translation.

As a concluding remark, it will be worthwhile to revisit the proposed mechanisms to see which argument our results are in line with. According to one-fluid phenomenological models, there are time-independent (steady) and time-dependent shear-banding flows governed by different inequalities [52, 54]. Eq. (1.9) predicts the steady shear-banding arising from the constitutive instability and Eq. (1.10) accounts for the time-dependent shear-banding accompanied by a strong stress overshoot. Additionally, an edge-induced disturbance could persist in the form of apparent shear-banding according to Hemingway and Fielding [56]. Since our DNA solutions display a monotonic relationship between the shear stress and the shear rate and we also ruled out the effect of edge instabilities

on bulk shear-profiles in Chapter 3, the shear-banding flow we observed should be the time-dependent one which is related to the strong stress overshoot.

Two-fluid models [3,64,66] predict concentration fluctuations along the shear-gradient (y-) direction, with a lower polymer concentration in the high shear-rate band and a higher polymer concentration in the low shear-rate band. Since polymer solutions become more viscous with increasing polymer concentrations [5], the high shear-rate band will exhibit a lower effective viscosity. Enhanced dynamics of embedded spherical particles (Fig. 2.6) and DNA-bridged dumbbells (Fig. 4.7 and Fig. 4.8) reflect the lower effective viscosity in the high shear-rate band, which seems to be in a qualitative agreement with the argument.

Meanwhile, the dynamics of the immersed tracers in the high shear-rate band were not entirely homogeneous. In Chapter 2, even though we observed that some spherical tracer particles in the high shear-rate band experienced very large displacement steps following a Lévy-walk-type motion, their fraction remained relatively lower compared to normally diffusing particles in the same band (Fig. 2.7). The co-existence of particles following different dynamics was captured by a growth of dynamic heterogeneity (Fig. 2.8), which implies heterogeneous local structures in the high shear-rate band. Similarly, in Chapter 4, only a fraction of the DNA-bridged dumbbells in the high shear-rate band exhibited strong couplings between translation and rotation, while many other dumbbells showed much weaker couplings and behaved similar to those in the low shear-rate band.

These findings lead us to propose that the unique dynamic features of the immersed tracers that we observed in the high shear-rate band could be localized, which hints to heterogeneous local structures. Such local heterogeneity on the xz-plane (within the same high shear-rate band or at the same y position) was not considered in the

two-fluid models where the polymer concentration was invariant along the x- and z-directions. For instance, Cromer and coworkers [3, 64] imposed an initial concentration defect, $\phi = 1 + \delta \cos(\pi k y/H)$, where ϕ is the normalized polymer concentration, δ is the magnitude of the defect, and k is a wave number. Accordingly, the steady state concentration profile was also a function of y only. As our experimental results indicate the presence of heterogeneity on the xz-plane, it will be also interesting to introduce concentration fluctuations along the x- and z-directions into the two-fluid model to see how their growth and attenuation are involved in the formation of the shear-bands.

The correlation between the translation and the inter-particle separation can provide us with a clue for such localized low viscosity zones in the high shear-rate band. In Chapter 4, we found an enhanced translation coupled with an extension of the DNA-linkers in the high shear-rate band (Fig. 4.10). It demonstrates that the formation of the low viscosity zone in the high shear-rate band could be related to the chain stretching. On the contrary, such a coupling was much weaker or negligible in the low shear-rate band. It means that structural changes in the localized zone, which arise from the chain stretching and reduce a local viscosity, occur exclusively in the high shear-rate band. Some molecular dynamics simulations [67, 69–71] and Wang [133] suggested that disentanglement of the polymer chain network in the high shear-rate band should be associated with the shear-banding formation. Based on this argument, we postulate that the flow-induced local disentanglement of the chain network which appears in the high shear-rate band can be a strong candidate for the microscopic picture linked to the observed shear-banding in entangled polymer solutions.

5.2 Future work

We studied the dynamics of the DNA-bridged dumbbell (Chapter 4) to acquire information about microscopic pictures. Its behavior, however, is expected to be different from native DNA chains as its chain ends are bound to colloidal particles. Single chain visualization will provide us with more direct, definite evidence to study the microscopic origins leading to the shear-banding formation. Single chain visualization by labeling a small fraction of chains (test chains) in the sea of dark background chains has been applied to many polymer physics studies, mostly using DNA as a model system with YOYO-1 as a fluorescent label [90, 117, 118, 134, 135].

Nonetheless, there are a number of imaging difficulties in applying this method directly. Since YOYO-1 is not covalently bonded to DNA, it can diffuse away from the labeled test chain to the surrounding chains and the fluorescence will be smeared out accordingly. Moreover, the shear-banding flows can be realized by applying fast shear flows to highly concentrated polymer solutions. In our study, DNA concentration was at least two orders of magnitude higher than its overlap concentration, which, to the author's knowledge, has not been reached by previous single DNA visualization studies. Furthermore, it is difficult to find an aqueous solvent that can match the refractive index of the DNA. Due to the high DNA concentration and the refractive index mismatch, it is challenging to image an individual chain clearly. In addition, fast flows require a short exposure time to avoid distortions of chain configurations in snapshots, which again reduces a signal-to-noise ratio and limits resolution. Lastly, the gap we adopted was up to 100 μm. We have to see through a few tens of microns of a highly concentrated solution to observe the chains near the top shear boundary where the high shear-rate band is developed. Thus, it will be important to find a suitable model system with a better index-match, a stable fluorescent label, and a large enough molecular size for

microscopy.

Another direction will be studying the dynamics over the entire shear cycle. In our study, we took strobed image sequences by synchronizing an image taking frequency to a shearing frequency. It means that we accessed to only a single fixed phase in the oscillatory shear cycle, where strain is at its maximum and shear rate is at its minimum. It was to minimize distortion of images under fast shear flows. If we develop a shear-cell with an alternative design, which has two shearing plates oscillating in the opposite directions, we can find a stationary xz-plane from an external viewpoint at a certain y-position, thereby observing the dynamics of the test chains or the tracers over the entire shear phase without worrying about the distortion of images. The new design will also help us resolve a short exposure time problem induced by the fast flow.

An interesting question we need to answer in the future study is whether the steady shear-banding and the time-dependent shear-banding share a common microscopic origin or not. LAOS is a useful experimental tool to study both types of shear-banding flows [54]. The steady shear-banding can be explored by choosing a polymer solution displaying a wide stress plateau and applying a large strain (A/H) with a low frequency (f) for a given shear rate. As the maximum shear amplitude in our shear-cell is bounded by the operation limit of a piezoelectric actuator, such conditions can be achieved by making a gap (H) smaller. However, we could study only the time-dependent shear-banding here since the smaller gap and the lower frequency always favored a wall-slip (Fig. 2.4). Therefore, it will be important to reduce the wall-slip to study the steady shear-banding with the same LAOS flow cell. Introducing roughness to the shearing plates and using a more viscous solvent will be helpful.

References

[1] M. H. Nafar Sefiddashti, B. J. Edwards, and B. Khomami. Individual chain dynamics of a polyethylene melt undergoing steady shear flow. *J. Rheol.*, 59(1):119–153, 2015.

[2] T. McLeish and R. Ball. A molecular approach to the spurt effect in polymer melt flow. *J. Polym. Sci. Pol. Phys.*, 24:1735, 1986.

[3] M. Cromer, G. H. Fredrickson, and L. G. Leal. A study of shear banding in polymer solutions. *Phys. Fluids*, 26:63101, 2014.

[4] M. Doi and S. F. Edwards. *The Theory of Polymer Dynamics*. Clarendon Press, Oxford, 1988.

[5] M. Rubinstein and M. Colby. *Polymer Physics*. Oxford University Press, New York, 2003.

[6] S. F. Edwards. The statistical mechanics of polymerized material. *Proc. Phys. Soc.*, 92:9–16, 1967.

[7] P. G. de Gennes. Reptation of a polymer chain in the presence of fixed obstacles. *J. Chem. Phys.*, 55:572–579, 1971.

[8] M. Doi and S. F. Edwards. Dynamics of concentrated polymer systems. part 1.—brownian motion in the equilibrium state. *J. Chem. Soc. Faraday Trans. 2*, 74:1789–1801, 1978.

[9] M. Doi and S. F. Edwards. Dynamics of concentrated polymer systems. part 2.—molecular motion under flow. *J. Chem. Soc. Faraday Trans. 2*, 74:1802–1817, 1978.

[10] M. Doi and S. F. Edwards. Dynamics of concentrated polymer systems. part 3.—the constitutive equation. *J. Chem. Soc. Faraday Trans. 2*, 74:1818–1832, 1978.

[11] G. Marrucci and N. Grizzuti. Fast flows of concentrated polymers: predictions of the tube model on chain stretching. *Gazz. Chim. Ital.*, 118:179–185, 1988.

[12] M. E. Cates, T. C. B. McLeish, and G. Marrucci. The rheology of entangled polymers at very high shear rates. *EPL (Europhysics Letters)*, 21:451, 1993.

[13] G. V. Vinogradov, A. Malkin, Y. G. Yanovskii, E. K. Borisenkova, B. V. Yarlykov, and G. V. Berezhnaya. Viscoelastic properties and flow of narrow distribution polybutadienes and polyisoprenes. *J. Polym. Sci. Pol. Phys.*, 10(6):1061–1084, 1972.

[14] M. Bercea, C. Peiti, B. Simionescu, and P. Navard. Shear rheology of semidilute poly (methyl methacrylate) solutions. *Macromolecules*, 26(25):7095–7096, 1993.

[15] M. E. Helgeson, P. A. Vasquez, E. W. Kaler, and N. J. Wagner. Rheology and spatially resolved structure of cetyltrimethylammonium bromide wormlike micelles through the shear banding transition. *J. Rheol.*, 53(3):727–756, 2009.

[16] H. Rehage and H. Hoffmann. Viscoelastic surfactant solutions: model systems for rheological research. *Mol. Phys.*, 74(5):933–973, 1991.

[17] S. Lerouge and JF. Berret. Shear-induced transitions and instabilities in surfactant wormlike micelles. *Adv. Polym. Sci.*, 230:1–71, 2009.

[18] T. C. B. McLeish. Tube theory of entangled polymer dynamics. *Advances in physics*, 51(6):1379–1527, 2002.

[19] G. Marrucci. Dynamics of entanglements: A nonlinear model consistent with the cox-merz rule. *J. Non-Newton. Fluid.*, 62(2-3):279–289, 1996.

[20] F. Snijkers, R. Pasquino, P. D. Olmsted, and D. Vlassopoulos. Perspectives on the viscoelasticity and flow behavior of entangled linear and branched polymers. *J. Phys. Condens. Matter*, 27(47):473002, 2015.

[21] J. M. Adams, S. M. Fielding, and P. D. Olmsted. Transient shear banding in entangled polymers: A study using the rolie-poly model. *J. Rheol.*, 55(5):1007–1032, 2011.

[22] R. S. Graham, A. E. Likhtman, T. C. B. McLeish, and S. T. Milner. Microscopic theory of linear, entangled polymer chains under rapid deformation including chain stretch and convective constraint release. *J. Rheol.*, 47:1171–1200, 2003.

[23] A. E. Likhtman and R. S. Graham. Simple constitutive equation for linear polymer melts derived from molecular theory: Rolie-poly equation. *J. Non-Newton. Fluid.*, 114(1):1–12, 2003.

[24] S.-Q. Wang, S. Ravindranath, and P. E. Boukany. Homogeneous shear, wall slip, and shear banding of entangled polymeric liquids in simple-shear rheometry: A roadmap of nonlinear rheology. *Macromolecules*, 44:183, 2011.

[25] M. M. Britton and P. T. Callaghan. Nuclear magnetic resonance visualization of anomalous flow in cone-and-plate rheometry. *J. Rheol.*, 41(6):1365–1386, 1997.

[26] P. T. Callaghan and A. M. Gil. Rheo-nmr of semidilute polyacrylamide in water. *Macromolecules*, 33(11):4116–4124, 2000.

[27] S. Ravindranath, S.-Q. Wang, M. Olechnowicz, and R. P. Quirk. Banding in simple steady shear of entangled polymer solutions. *Macromolecules*, 41:2663, 2008.

[28] P. E. Boukany and S. Q. Wang. A correlation between velocity profile and molecular weight distribution in sheared entangled polymer solutions. *J. Rheol.*, 51(2):217–233, 2007.

[29] P. E. Boukany, Y. T. Hu, and S.-Q. Wang. Observations of wall slip and shear banding in an entangled dna solution. *Macromolecules*, 41(7):2644–2650, 2008.

[30] P. E. Boukany and S.-Q. Wang. Exploring the transition from wall slip to bulk shearing banding in well-entangled dna solutions. *Soft Matter*, 5:780, 2009.

[31] P. E. Boukany, S.-Q. Wang, S. Ravindranath, and L. J. Lee. Shear banding in entangled polymers in the micron scale gap: a confocal-rheoscopic study. *Soft Matter*, 11:8058, 2015.

[32] P. Tapadia, S. Ravindranath, and S.-Q. Wang. Banding in entangled polymer fluids under oscillatory shearing. *Phys. Rev. Lett.*, 96:196001, 2006.

[33] S. Ravindranath and S.-Q. Wang. Large amplitude oscillatory shear behavior of entangled polymer solutions: Particle tracking velocimetric investigation. *J. Rheol.*, 52:341–358, 2008.

[34] S. Ravindranath, S. Q. Wang, M. Olechnowicz, V. S. Chavan, and R. P. Quirk. How polymeric solvents control shear inhomogeneity in large deformations of entangled polymer mixtures. *Rheologica acta*, 50(2):97–105, 2011.

[35] S. Ravindranath and S.-Q. Wang. Steady state measurements in stress plateau region of entangled polymer solutions: Controlled-rate and controlled-stress modes. *J. Rheol.*, 52:957–980, 2008.

[36] Y. Li, M. Hu, G. B. McKenna, C. J. Dimitriou, G. H. McKinley, R. M. Mick, D. C. Venerus, and L. A. Archer. Flow field visualization of entangled polybutadiene solutions under nonlinear viscoelastic flow conditions. *J. Rheol.*, 57:1411, 2013.

[37] S.-Q. Wang, G. Liu, S. Cheng, P. E. Boukany, Y. Wang, and X. Li. Letter to the editor: Sufficiently entangled polymers do show shear strain localization at high enough weissenberg numbers. *J. Rheol.*, 58:1059, 2014.

[38] Y. Li, M. Hu, G. B. McKenna, C. J. Dimitriou, G. H. McKinley, R. M. Mick, D. C. Venerus, and L. A. Archer. Response to: Sufficiently entangled polymers do show shear strain localization at high enough weissenberg numbers. *J. Rheol.*, 58:1071, 2014.

[39] Y. Li and G. B. McKenna. Startup shear of a highly entangled polystyrene solution deep into the nonlinear viscoelastic regime. *Rheol. Acta*, 54:771–777, 2015.

[40] Y. T. Hu. Steady-state shear banding in entangled polymers? *J. Rheol.*, 54:1307, 2010.

[41] S. Cheng and S.-Q. Wang. Is shear banding a metastable property of well-entangled polymer solutions? *J. Rheol.*, 56:1413, 2012.

[42] S. Jaradat, M. Harvey, and T. A. Waigh. Shear-banding in polyacrylamide solutions revealed via optical coherence tomography velocimetry. *Soft Matter*, 8:11677, 2012.

[43] T. B. Goudoulas, S. Pan, and N. Germann. Nonlinearities and shear banding instability of polyacrylamide solutions under large amplitude oscillatory shear. *J. Rheol.*, 61(5):1061–1083, 2017.

[44] K. Sato, I. Kunita, Y. Takikawa, D. Takeuchi, Y. Tanaka, T. Nakagaki, and H. Orihara. Direct observation of orientation distributions of actin filaments in a solution undergoing shear banding. *Soft Matter*, 13:2708–2716, 2017.

[45] T. B. Goudoulas, S. Pan, and N. Germann. Double-stranded and single-stranded well-entangled dna solutions under laos: A comprehensive study. *Polymer*, 140:240–254, 2018.

[46] H. Tang, T. Kochetkova, H. Kriegs, J. K. G. Dhont, and M. P. Lettinga. Shear-banding in entangled xanthan solutions: tunable transition from sharp to broad shear-band interfaces. *Soft matter*, 14(5):826–836, 2018.

[47] T. Divoux, M. A. Fardin, S. Manneville, and S. Lerouge. Shear banding of complex fluids. *Annu. Rev. Fluid Mech.*, 48:81, 2016.

[48] P. D. Olmsted. Perspectives on shear banding in complex fluids. *Rheol. Acta*, 47:283, 2008.

[49] H. Giesekus. A simple constitutive equation for polymer fluids based on the concept of deformation-dependent tensorial mobility. *J. Fluid. Mech*, 11(1-2):69–109, 1982.

[50] M. W. Johnson and D. Segalman. A model for viscoelastic fluid behavior which allows non-affine deformation. *J. Fluid Mech.*, 2(3):255–270, 1977.

[51] J. M. Adams and P. D. Olmsted. Nonmonotonic models are not necessary to obtain shear banding phenomena in entangled polymer solutions. *Phys. Rev. Lett.*, 102(6):067801, 2009.

[52] R. L. Moorcroft and S. M. Fielding. Criteria for shear banding in time-dependent flows of complex fluids. *Phys. Rev. Lett.*, 110:086001, 2013.

[53] R. L. Moorcroft and S. M. Fielding. Shear banding in time-dependent flows of polymers and wormlike micelles. *J. Rheol.*, 58(1):103–147, 2014.

[54] K. A. Carter, J. M. Girkin, and S. M. Fielding. Shear banding in large amplitude oscillatory shear (laostrain and laostress) of polymers and wormlike micelles. *J. Rheol.*, 60(5):883–904, 2016.

[55] E. J. Hemingway, H. Kusumaatmaja, and S. M. Fielding. Edge fracture in complex fluids. *Phys. Rev. Lett.*, 119(2):028006, 2017.

[56] E. J. Hemingway and S. M. Fielding. Edge-induced shear banding in entangled polymeric fluids. *Phys. Rev. Lett.*, 120:138002, 2018.

[57] E. J. Hemingway and S. M. Fielding. Edge fracture instability in sheared complex fluids: Onset criterion and possible mitigation strategy. *J. Rheol.*, 63:735, 2019.

[58] S. Hooshyar and N. Germann. A thermodynamic study of shear banding in polymer solutions. *Phys. Fluids*, 28(6):063104, 2016.

[59] K. A. Dill and B. H. Zimm. A rhelogical separator for very large dna molecules. *Nucleic Acids Res.*, 7(3):735–749, 1979.

[60] A. B. Metzner and Y. Cohenand C. Rangel-Nafaile. Inhomogeneous flows of non-newtonian fluids: Generation of spatial concentration gradients. *J. Fluid Mech.*, 5:449–462, 1979.

[61] M. J. MacDonald and S. J. Muller. Experimental study of shear-induced migration of polymers in dilute solutions. *J. Rheol.*, 40(2):259–283, 1996.

[62] E. Helfand and G. H. Fredrickson. Large fluctuations in polymer solutions under shear. *Phys. Rev. Lett.*, 62(21):2468, 1989.

[63] J. L. Goveas and G. H. Fredrickson. Curvature-driven shear banding in polymer melts. *J. Rheol.*, 43(5):1261–1277, 1999.

[64] M. Cromer, M. C. Villet, G. H. Fredrickson, and L. G. Leal. Shear banding in polymer solutions. *Phys. Fluids*, 25:051703, 2013.

[65] M. Cromer, G. H. Fredrickson, and L. Gary Leal. Concentration fluctuations in polymer solutions under mixed flow. *J. Rheol.*, 61:711, 2017.

[66] J. D. Peterson, M. Cromer, G. H. Fredrickson, and L. Gary Leal. Shear banding predictions for the two-fluid rolie-poly model. *J. Rheol.*, 60:927, 2016.

[67] M. Mohagheghi and B. Khomami. Molecular processes leading to shear banding in well entangled polymeric melts. *ACS Macro Lett.*, 4:684, 2015.

[68] J. Cao and A. E. Likhtman. Shear banding in molecular dynamics of polymer melts. *Phys. Rev. Lett.*, 108:028302, 2012.

[69] M. Mohagheghi and B. Khomami. Elucidating the flow-microstructure coupling in the entangled polymer melts. part i: Single chain dynamics in shear flow. *J. Rheol.*, 60:849, 2015.

[70] M. Mohagheghi and B. Khomami. Elucidating the flow-microstructure coupling in entangled polymer melts. part ii: Molecular mechanism of shear banding. *J. Rheol.*, 60:861, 2015.

[71] M. Mohagheghi and B. Khomami. Molecularly based criteria for shear banding in transient flow of entangled polymeric fluids. *Phys. Rev. E*, 93(6):062606, 2016.

[72] L. M. Walker. Rheology and structure of worm-like micelles. *Curr. Opin. Colloid In.*, 6:451–456, 2001.

[73] P. T. Callaghan. Rheo nmr and shear banding. *Rheol. Acta*, 47:243, 2008.

[74] I. Cohen, B. Davidovitch, A. B. Schofield, M. P. Brenner, and D. A. Weitz. Slip, yield, and bands in colloidal crystals under oscillatory shear. *Phys. Rev. Lett.*, 97:215502, 2006.

[75] N. Koumakis, M. Laurati, S. U. Egelhaaf, J. F. Brady, and G. Petekidis. Yielding of hard-sphere glasses during start-up shear. *Phys. Rev. Lett.*, 108:098303, 2012.

[76] V. Grenard, T. Divoux, N. Taberlet, and S. Manneville. Timescales in creep and yielding of attractive gels. *Soft Matter*, 10:1555–1571, 2014.

[77] T. Divoux, D. Tamarii, C. Barentin, and S. Manneville. Transient shear banding in a simple yield stress fluid. *Phys. Rev. Lett.*, 104:208301, 2010.

[78] X. Cheng, J. B. Lechman, A. Fernandez-Barbero, G. S. Grest, H. M. Jaeger, G. S. Karczmar, M. E. Möbius, and S. R. Nagel. Three-dimensional shear in granular flow. *Phys. Rev. Lett.*, 96:038001, 2006.

[79] P. Schall and M. van Hecke. Shear bands in matter with granularity. *Annu. Rev. Fluid Mech.*, 42:67, 2010.

[80] S. M. Fielding. Triggers and signatures of shear banding in steady and time-dependent flows. *J. Rheol.*, 821, 2016.

[81] P. E. Boukany, Y. T. Hu, and S.-Q. Wang. Observations of wall slip and shear banding in an entangled dna solution. *Macromolecules*, 41:2644, 2008.

[82] P. E. Boukany and S.-Q. Wang. Shear banding or not in entangled dna solutions depending on the level of entanglement. *J. Rheol.*, 53:73–83, 2009.

[83] S. Ravindranath, Y. Wang, P. E. Boukany, and X. Li. Letter to the editor: Cone partitioned plate (cpp) vs circular couette. *J. Rheol.*, 56:675, 2012.

[84] Y. T. Hu. Response to: Cpp vs circular couette. *J. Rheol.*, 56:683, 2012.

[85] K. A. Hayes, M. R. Buckley, I. Cohen, and L. A. Archer. High resolution shear profile measurements in entangled polymers. *Phys. Rev. Lett.*, 101:218301, 2008.

[86] K. A. Hayes, M. R. Buckley, H. Qi, I. Cohen, and L. A. Archer. Constitutive curve and velocity profile in entangled polymers during start-up of steady shear flow. *Macromolecules*, 43:4412, 2010.

[87] L. Noirez, H. Mendil-Jakani, and P. Baroni. New light on old wisdoms on molten polymers: conformation, slippage and shear banding in sheared entangled and unentangled melts. *Rapid Comm.*, 30:1709, 2009.

[88] S. M. Fielding and P. D. Olmsted. Early stage kinetics in a unified model of shear-induced demixing and mechanical shear banding instabilities. *Phys. Rev. Lett.*, 90:224501, 2003.

[89] D. R. Tree, A. Muralidhar, P. S. Doyle, and K. D. Dorfman. Is dna a good model polymer? *Macromolecules*, 46:8369, 2013.

[90] R. E. Teixeira, A. K. Dambal, D. H. Richter, E. S. G. Shaqfeh, and S. Chu. The individualistic dynamics of entangled dna in solution. *Macromolecules*, 40:2461, 2007.

[91] J. D. Ferry. *Viscoelastic Properties of Polymers, 3rd ed.* Wiley, 1980.

[92] R. G. Larsonn, T. Sridhar, L. G. Leal, G. H. McKinley, A. E. Likhtman, and T. C. B. McLeish. Definitions of entanglement spacing and time constants in the tube model. *J. Rheol.*, 47:809, 2003.

[93] X. Cheng, J. H. McCoy, J. N. Israelachvili, and I. Cohen. Imaging the microscopic structure of shear thinning and thickening colloidal suspensions. *Science*, 333:1276, 2011.

[94] N. Y. C. Lin, J. McCoy, X. Cheng, B. Leahy, J. Israelachvili, and I. Cohen. A multi-axis confocal rheoscope for studying shear flow of structured fluids. *Rev. Sci. Instrum.*, 85:033905, 2014.

[95] N. K. Reddy, C. Ruth, and C. Clasen. *Bulletin of The Society of Rheology 84th Annual Meeting*, 2013.

[96] B. D. Leahy, X. Cheng, D. C. Ong, C. Liddell-Watson, and I. Cohen. Enhancing rotational diffusion using oscillatory shear. *Phys. Rev. Lett.*, 110:22830, 2013.

[97] A. Ott, J. P. Bouchaud, D. Langevin, and W. Urbach. Anomalous diffusion in "living polymers": A genuine levy flight? *Phys. Rev. Lett.*, 65:2201, 1990.

[98] J. Zausch, J. Horbach, M. Laurati, S. U. Egelhaaf, J. M. Brader, T. Voigtmann, and M. Fuchs. From equilibrium to steady state: the transient dynamics of colloidal liquids under shear. *J. Phys. Condens. Matter*, 20:404210, 2008.

[99] J. Klafter and I. M. Sokolov. *First Steps in Random Walks*. Oxford Univ. Press, Oxford, UK, 2011.

[100] L. Berthier, G. Biroli, J.-P. Bouchaud, L. Cipelletti, and W. van Saarloos. *Dynamical Heterogeneities in Glasses, Colloids and Granular Media*. Oxford Univ. Press, Oxford, UK, 2011.

[101] S. G. Hatzikiriakos. Slip mechanisms in complex fluid flows. *Soft Matter*, 11:7851, 2015.

[102] S.-Q. Wang. *Nonlinear Polymer Rheology*. Wiley, Hoboken, NJ, 2018.

[103] T. Schweizer and M. Stockli. Departure from linear velocity profile at the surface of polystyrene melts during shear in cone-plate geometry. *J. Rheol*, 52:713–727, 2008.

[104] I. Kirchenbuechler, D. Guu, N. A. Kurniawan, G. H. Koenderink, and M. P. Lettinga. Direct visualization of flow-induced conformational transitions of single actin filaments in entangled solutions. *Nat. Commun.*, 5:5060, 2014.

[105] O. Hemminger and P. E. Boukany. Microscopic origin of wall slip during flow of an entangled dna solution in microfluidics: Flow induced chain stretching versus chain desorption. *Biomicrofluidics*, 11:044118, 2017.

[106] C.-C. Hsieh, A. Balducci, and P. S. Doyle. Ionic effects on the equilibrium dynamics of dna confined in nanoslits. *Nano Lett.*, 8:1683–1688, 2008.

[107] J. S. Vrentas, D. C. Venerus, and C. M. Vrentas. An exact analysis of reservoir effects for rotational viscometers. *Chem. Eng. Sci.*, 46:33–37, 1991.

[108] C. W. Macosko. *Rheology: Principles, Measurements, and Applications*. Wiley-VCH, New York, 1994.

[109] N. Y. C. Lin, S. Goyal, X. Cheng, R. N. Zia, F. A. Escobedo, and I. Cohen. Far-from-equilibrium sheared colloidal liquids: Disentangling relaxation, advection, and shear-induced diffusion. *Phys. Rev. E*, 88:062309, 2013.

[110] S. M. Fielding. Shear banding in soft glassy materials. *Reports Prog. Phys.*, 77:102601, 2014.

[111] N. Germann. Shear banding in semidilute entangled polymer solutions. *Curr. Opin. Colloid Interface Sci.*, 39:1–10, 2019.

[112] S. Q. Wang, S. Ravindranath, Y. Wang, and P. Boukany. New theoretical considerations in polymer rheology: Elastic breakdown of chain entanglement network. *J. Chem. Phys.*, 127:064903, 2007.

[113] P. E. Boukany and S. Q. Wang. Use of particle-tracking velocimetry and flow birefringence to study nonlinear flow behavior of entangled wormlike micellar solution: From wall slip, bulk disentanglement to chain scission. *Macromolecules*, 41:1455, 2008.

[114] M. E. Helgeson, M. D. Reichert, Y. T. Hu, and N. J. Wagner. Relating shear banding, structure, and phase behavior in wormlike micellar solutions. *Soft Matter*, 5:3858, 2009.

[115] M. A. Calabrese, S. A. Rogers, R. P. Murphy, and N. J. Wagner. The rheology and microstructure of branched micelles under shear. *J. Rheol.*, 59:1299, 2015.

[116] M. A. Calabrese, S. A. Rogers, L. Porcar, and N. J. Wagner. Understanding steady and dynamic shear banding in a model wormlike micellar solution. *J. Rheol.*, 60:1001, 2016.

[117] Y. Zhou and C. M. Schroeder. Dynamically heterogeneous relaxation of entangled polymer chains. *Phys. Rev. Lett.*, 120(26):267801, 2018.

[118] C. M. Schroeder. Single polymer dynamics for molecular rheology. *J. Rheol.*, 62(1):371–403, 2018.

[119] C. van der Wel, N. Bossert, Q. J. Mank, M. G. T. Winter, D. Heinrich, and D. J. Kraft. Surfactant-free colloidal particles with specific binding affinity. *Langmuir*, 33(38):9803–9810, 2017.

[120] J. Byrom, P. Han, M. Savory, and S. L. Biswal. Directing assembly of dna-coated colloids with magnetic fields to generate rigid, semiflexible, and flexible chains. *Langmuir*, 30(30):9045–9052, 2014.

[121] S. R. Bhatia and W. B. Russel. End-capped associative polymer chains between nanospheres: Attractions in ideal solutions. *Macromolecules*, 33:5713, 2000.

[122] C. N. Likos. Effective interactions in soft condensed matter physics. *Phys. Rep.*, 348:267, 2001.

[123] T. Schmatko, B. Bozorgui, N. Geerts, D. Frenkel, E. Eiser, and W. C. K. Poon. A finite-cluster phase in λ-dna-coated colloids. *Soft Matter*, 3:703, 2007.

[124] S. Shin, K. D. Dorfman, and X. Cheng. Effect of edge disturbance on shear banding in polymeric solutions. *J. Rheol.*, 62:1339, 2018.

[125] L. G. Leal. Slow motion of slender rod-like particles in 2nd order fluid. *J. Fluid Mech.*, 69:305, 1975.

[126] D. Z. Gunes, R. Scirocco, J. Mewis, and J. Vermant. Flow-induced orientation of non-spherical particles: Effect of aspect ratio and medium rheology. *J. Nonnewton. Fluid Mech.*, 155:39, 2008.

[127] S. Shin, K. D. Dorfman, and X. Cheng. Shear-banding and superdiffusivity in entangled polymer solutions. *Phys. Rev. E*, 96:062503, 2017.

[128] R. T. Foister and T. G. M. Van De Ven. Diffusion of brownian particles in shear flows. *J. Fluid Mech.*, 96:105, 1980.

[129] Y. Takikawa and H. Orihara. Diffusion of brownian particles under oscillatory shear flow. *J. Phys. Soc. Japan*, 81:124001, 2012.

[130] J. Happel and H. Brenner. *Low Reynolds Number Hydrodynamics: With Special Applications to Particulate Media*. Springer, Science & Business Media, 2012.

[131] S. Q. Wang. Nonlinear rheology of entangled polymers at turning point. *Soft Matter*, 11(8):1454–1458, 2015.

[132] G. P. Shrivastav, P. Chaudhuri, and J. Horbach. Heterogeneous dynamics during yielding of glasses: Effect of aging. *J. of Rheol.*, 60(5):835–847, 2016.

[133] S. Q. Wang. From wall slip to bulk shear banding in entangled polymer solutions. *Macromol. Chem. Phys.*, 220(1):1800327, 2019.

[134] T. T. Perkins, D. E. Smith, and S. Chu. Direct observation of tube-like motion of a single polymer chain. *Science*, 264(5160):819–822, 1994.

[135] D. E. Smith, T. T. Perkins, and S. Chu. Self-diffusion of an entangled dna molecule by reptation. *Phys. Rev. Lett.*, 75(22):4146, 1995.